

**Spectroscopic Investigation on Fluorescent Probes
in Biologically Relevant and Engineered
Environments**

**THESIS
SUBMITTED FOR THE DEGREE OF
DOCTOR OF PHILOSOPHY (SCIENCE)
OF
JADAVPUR UNIVERSITY
2014**

**BY

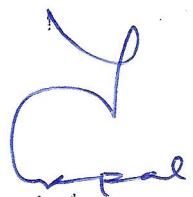
SUBRATA BATABYAL**

**DEPARTMENT OF CHEMICAL, BIOLOGICAL AND
MACROMOLECULAR SCIENCES,
S. N. BOSE NATIONAL CENTRE FOR BASIC SCIENCES,
BLOCK JD, SECTOR III, SALT LAKE,
KOLKATA 700 098, INDIA**

सत्येन्द्र नाथ बसु राष्ट्रीय मौलिक विज्ञान केन्द्र
**SATYENDRA NATH BOSE NATIONAL
CENTRE FOR BASIC SCIENCES**

CERTIFICATE FROM THE SUPERVISOR

This is to certify that the thesis entitled "Spectroscopic Investigation on Fluorescent Probes in Biologically Relevant and Engineered Environments" submitted by Mr. Subrata Batabyal, who got his name registered on June 23, 2010 for the award of **Ph.D. (Science) degree of Jadavpur University**, is absolutely based upon his own work under the supervision of Professor Samir Kumar Pal and that neither this thesis nor any part of it has been submitted for any degree/diploma or any other academic award anywhere before.



10th March 2014

(Signature of Supervisor/date with official seal)

Dr. SAMIR KUMAR PAL
Professor
S. N. Bose National Centre For Basic Sciences
Government of India
Block-JD, Sector-III, Salt Lake
Kolkata-700098

ब्लॉक जे० डी०, सेक्टर-३, साल्ट लेक, कोलकाता ७०००९८, BLOCK-JD, SECTOR III, SALT LAKE, KOKATA - 700 098

दूरभाष/ Phones : 0091-(0)33-2335 5705-8, 2335 3057/61, 2335 0312/1313

ई-मेल/ E-mail : root@bose.res.in

Webpage : <http://www.bose.res.in>

Fax : 0091-(0)33-2335 3477

FUNDED BY THE DEPARTMENT OF SCIENCE & TECHNOLOGY, GOVT. OF INDIA

निष्ठिवद्ध विज्ञान और प्रौद्योगिकी विभाग भारत सरकार द्वारा

*To My Parents
and Brother*

Acknowledgements

Undertaking this PhD has been a truly life-changing experience for me and it would not have been possible to do without the support and guidance that I received from many people.

I would like to express my sincere gratitude to my PhD supervisor, Professor Samir Kumar Pal. Without his inspirational guidance, his enthusiasm, his encouragements, his unconditional help, I could never finish my doctoral work. He has provided guidance at the key moments in my work while also allowing me to work independently. His advice on both research as well as on my career have been priceless. I appreciate all his contributions of time, ideas, and support to make my PhD experience productive and stimulating. The joy and enthusiasm he has for his research was contagious and motivational for me, even during tough times in the Ph.D. pursuit. I am also thankful for the excellent example he has provided as a successful experimental scientist and professor.

I have enjoyed fruitful collaborations of Professor Siddhartha Roy, Professor A. K. Raychaudhuri and Dr. Kaustuv Das. Special recognition is given to Professor Siddhartha Roy, director IICB, for his valuable advices and encouragement. I owe a special thanks to Dr. Abhishek Mazumder, of IICB for his help in the training of molecular biology. Great appreciation is extended to SNNCBS staffs and faculty members for their assistances in my research career. I owe a special thanks to the CSIR, India for my research fellowship, and Department of Science and Technology (DST), India for projects.

Because of the research environment sustained by Professor Pal, I have crossed paths with a number of PhD students (Dr. Pramod Kumar Verma, Dr. Abhinandan Makhal) who have influenced and enriched my earlier stages of research. I want to specially acknowledge Dr. Tanumoy Mondal, with whom I have been directly involved in doing research and for sharing a great time together. The direction of my Ph.D. work has been strongly influenced by the members of the Pal group, notably Nirmal, Soumik, Anupam, Surajit, Ranajay, Soma, Siddhi, Susobhan, Samim, Nabarun, Prasanna da and Soumendra da. I am, especially thankful to Nirmal, Anupam, Surajit and Ranajay who shared glorious moments over a long period of time, supported my work, annoyances, and also for the good moments of fun!

Finally, I would like to express my gratitude to my family who supports me through thick and thin, with loves and affections. I want them to know that I love them cordially. Without their sacrifices, moral supports and blessings the thesis would not have taken its shape.

Dated: 10th March, 2014

Department of Chemical, Biological and Macromolecular Sciences,
S. N. Bose National Centre for Basic Sciences,
Salt Lake, Kolkata 700098, India

Subrata Batabyal.
(Subrata Batabyal)

CONTENTS

	Page
Chapter 1: Introduction	
1.1. Scope of the spectroscopic investigation on fluorescent probes in biologically relevant and engineered environments	1
1.2. Objective	5
1.3. Summary of the work done	7
1.3.1. Time-resolved spectroscopic studies on biological and engineered environments	7
1.3.1.1. Picosecond-resolved solvent reorganization and energy transfer in biological and model cavities.	7
1.3.2. Spectroscopic studies on the interfacial dynamics at a specific protein-DNA interface	8
1.3.2.1. Ultrafast interfacial solvation dynamics in specific protein-DNA recognition	8
1.3.3. Development of an engineered platform for the detection of very fast molecular/biomolecular interaction	8
1.3.3.1. An improved microfluidics approach for monitoring real-time interaction profiles of ultrafast molecular recognition	8
1.3.4. Spectroscopic studies on the ultrafast migration of radiation at the engineered dielectric interface	9
1.3.4.1. Förster resonance energy transfer in a nanoscopic system on dielectric interfaces	9
1.3.5. Ultrafast spectroscopic studies on the photon-plasmon interaction at a technologically important interface	10

	Page
1.3.5.1. Ultrafast dynamics of excitons in semiconductor quantum dots on a plasmonically active nano-structured silver film	10
1.4. Plan of thesis	10
References	12
 Chapter 2: An overview of steady-state and dynamical tools and systems	
2.1. Steady-state and dynamical tools	17
2.1.1. Solvation dynamics	17
2.1.2. Fluorescence anisotropy	25
2.1.3. Estimation of microviscosity from Stokes-Einstein-Debye equation	32
2.1.4. Arrhenius theory of activation energy	32
2.1.5. Förster resonance energy transfer (FRET)	34
2.1.6. Circular dichroism (CD)	38
2.1.7. Twisted intramolecular charge transfer (TICT)	42
2.1.8. Tachiya model	43
2.1.9. Quantum yield calculation	44
2.1.10. Microfluidics theory	44
2.2. Systems	47
2.2.1. Organized assemblies (biomimetics)	47
2.2.1.1. Micelle	47
2.2.1.2. Reverse micelle	48
2.2.2. Protein	51
2.2.2.1. Human serum albumin	51
2.2.2.2. Lambda repressor (λ -repressor)	53

	Page
2.2.3. Deoxyribonucleic acid	55
2.2.4. Molecular probes	57
2.2.4.1. p-Benzoquinone (BQ)	57
2.2.4.2. Tryptophan [(2S)-2-amino-3-(1H-indol-3-yl)propanoic acid]	58
2.2.4.3. [2'-(4-Hydroxyphenyl)-5-(4-methyl-1-piperazinyl)-2,5'-bi-1H benzimidazole trihydrochloride hydrate], Hoechst 33258 (H258)	58
2.2.4.4. Ethidium bromide (EtBr)	58
2.2.4.5. Merocyanine 540	59
2.2.4.6. 6-Acryloyl-2-dimethylaminonaphthalene (acrylodan)	60
2.2.5. Quantum dots (QDs)	60
References	62

Chapter 3: Instrumentation and sample preparation

3.1. Instrumental Setup	69
3.1.1. Steady-state UV-Vis absorption and emission measurement	69
3.1.2. Circular dichroism (CD) measurement	70
3.1.3. Time correlated single photon counting (TCSPC) technique	71
3.1.4. Transmission electron microscopy (TEM)	73
3.1.5. Scanning electron microscopy (SEM)	74
3.1.6. Microfluidics methodology	74
3.1.7. Fluorescence microscope	77
3.2. Sample preparation	78
3.2.1. Chemicals used	78

	Page
3.2.2. λ -repressor isolation and purification	79
3.2.3. Preparation of reverse micelle	80
3.2.4. Preparation of synthetic and genomic DNA solutions	81
3.2.5. Chemical modification of serum albumin	81
3.2.6. Preparation of QDs-MC conjugate	81
3.2.7. Preparation of silver mirror	81
References	82
 Chapter 4: Time-resolved spectroscopic studies on biological and engineered environments	
4.1. Introduction	83
4.2. Results and discussion	85
4.2.1. Picosecond-resolved solvent reorganization and energy transfer in biological and model cavities.	85
4.3. Conclusion	100
References	101
 Chapter 5: Spectroscopic studies on the interfacial dynamics at a specific protein-DNA interface	
5.1. Introduction	105
5.2. Results and discussion	107
5.2.1. Ultrafast interfacial solvation dynamics in specific protein-DNA recognition	107
5.3. Conclusion	117
References	118
 Chapter 6: Development of an engineered platform for the detection of very fast molecular/biomolecular interaction	

	Page
6.1. Introduction	122
6.2. Results and discussion	124
6.2.1. An improved microfluidics approach for monitoring real-time interaction profiles of ultrafast molecular recognition	124
6.3. Conclusion	132
References	133
 Chapter 7: Spectroscopic studies on the ultrafast migration of radiation at the engineered dielectric interface	
7.1. Introduction	137
7.2. Results and discussion	139
7.2.1. Förster resonance energy transfer in nanoscopic system on dielectric interfaces	139
7.3. Conclusion	146
References	148
 Chapter 8: Ultrafast spectroscopic studies on the photon- plasmon interaction at a technologically important interface	
8.1. Introduction	151
8.2. Results and discussion	152
8.2.1. Ultrafast dynamics of excitons in semiconductor quantum dots on a plasmonically active nano structured silver film	152
8.3. Conclusion	158
References	159
List of Publications	162

Chapter 1

Introduction

1.1. Scope of the spectroscopic investigation on fluorescent probes in biologically relevant and engineered environments:

The use of fluorescent probes in biophysical research has been a common practice in recent years, and their use is continually increasing due to their versatility, sensitivity, quantitative capabilities, and technological applicability [1-3]. Among their myriad of uses, fluorescent probes are employed to perceive biomolecular interaction [4, 5] catalysis reaction, structural/conformational changes [6, 7] and to monitor biological processes in vivo and in vitro [8-10]. From the technological viewpoint, fluorescent probes also possess immense potentials [11]. Fluorescence based techniques have certain distinct advantages over the other biophysical/bioanalytical techniques (XRD, NMR etc.) due to some of its salient features related to the requirement of low sample concentration, solution phase data collection, noninvasiveness, cost-effectiveness, faster experimental timeframe [12]. Fluorescent probes can be categorized broadly into two classes. Organic dyes, a prominent class of fluorescent probes find its use and relevance in bioanalytical research arenas due to their active functional groups for site specific labelling, noncovalent conjugate formation with the target molecules, small sizes, distinct excitable wavelength region and biocompatibility [13-15].

On the other hand, semiconductor quantum dots (QDs) is an emerging class of fluorescent probes due to photostability, higher quantum yield, sharp emission band, which not only finds its relevance in innumerable biological applications [1, 16, 17] (bioimaging, bioconjugation), but also possess immense technological potentials (solar cell, photovoltaic, optoelectronic devices etc.) [18, 19]. However, the fluorescence property of dyes/QDs is of no use unless applied

intelligent and effective way. Fluorescence is a manifestation of spontaneous emission of radiation. It was long believed that spontaneous emission is molecular or atomic property and the 'Einstein A coefficient' is a constant parameter. Purcell first objectively predicted the modification of the spontaneous emission rate by cavity effects in the radiofrequency domain [20]. Since then, not much works have been persuaded [21, 22] until recently the use of modified engineered environments like optical cavity, photonic crystal, dielectric interface came into the play to modify the fluorescence behavior for variety of applications and for exploration of key physical processes [23-25]. Coincidentally, it was Purcell, who probably first visualized the importance of confined microenvironment (microchannel) and delivered a famous lecture entitled "Life at low Reynolds number" [26]. The effect of confined engineered environments on various fluorescent probes opens up the door to investigate and interpret a broad range of problems ranging from physics to biology. Confined engineered environment results in the significant modification of the fluoroprobe properties (fluorescence intensity, emission wavelength, fluorescence lifetime etc.) due to the geometrical restriction and interactions with the confining framework, thus providing important information about the system under study [27]. Cavity and cleft of proteins, minor groove of DNA and interface of protein-DNA complex are the well-defined examples of confined biologically relevant engineered environments. The hydrophobic effect, hydrogen bonding, side chain flexibility are important parameters which play crucial role in fluorescence behavior of the probe molecules within the confined biological systems. Some of the biomimetic systems including micelles and reverse micelles-isolated, surfactant-coated water droplets have emerged as a tenable artificially engineered model for confined water in biological systems [28, 29].

Intellectual use of fluorescent probes, in biologically relevant engineered environment can enrich the knowledgebase of key dynamical processes, structural

parameters involved in molecular recognition, protein folding, and protein-DNA interactions. Sometimes, the traditional confined environment and bulk study fall short to provide clear idea of various fundamental process like fast kinetics, involvement of intermediates in a recognition process, and also the role of diffusion/convection in key physicochemical process. For studying molecular recognition and fast kinetics reaction, flow-stopped kinetic is conveniently used. But the flow-stopped methodology has some inherent shortcomings due to the limited time resolution (~millisecond) associated with its characteristic 'dead time' [30, 31] and requirement of large sample volumes. To overcome the limitation, microfluidics techniques, a confined engineered environment is an alternative superior method as it provides location-specific in-depth information of reaction/interaction processes with superior spatiotemporal resolution [32-35]. On the other hand, optical cavity, dielectric interface, photonic crystal are good examples of technologically relevant engineered environments [36, 37]. The fluorescence can be enhanced, attenuated or even suppressed by such environments. The intellectual use of such environments to tailor or monitor the fluorescent properties of probes can be highly assistive to understand several key physical/biological processes and could have profound consequence in device designing and performance.

The key focus of this thesis is to explore the detail spectroscopic properties of various kinds of fluoroprobe including organic dyes/drugs and inorganic semiconductor QDs in different host environments of biological and technological interest. Many key chemical and biochemical reactions, particularly in living cells, take place in confined space at the microscopic scale [38, 39]. While exploring the biological/biomimetic cavities and interface, we investigated the solvent relaxation of acrylodan probe residing in the cleft of Serum albumin and inside a reverse micelle. Förster resonance energy transfer (FRET) was employed to monitor the distance between donor (tryptophan) and acceptor (acrylodan) and hence the dynamical and structural fluctuation over the time and a wide

temperature range. We also explored the interfacial water dynamics and DNA side chain flexibility using Hoechst 33258 (H258), a well-known DNA minor groove binder, in specific protein-DNA interaction between lambda repressor protein and different operator DNA. The effect on the exchangeability of minor groove water molecules with the bulk water molecules in protein-DNA complex was investigated using temperature dependent solvation study on H258. To capture and analyze the intermediate state of molecular recognition, an optofluidics platform was indigenously developed by coupling microfluidics to fluorescence spectrophotometer and fluorescence microscope. Molecular recognition of small molecules (drugs/ligands) with biomimetic and biological macromolecules was studied in the confined microchannel by collecting fluorescence image and lifetime along the microchannel at well-defined positions. The platform also demonstrated the capability of monitoring fast reaction kinetics of a model ionic reaction. The technologically relevant engineered environments and its effect on the emission properties of closely placed emitter (QDs) was also studied. In this respect, the effect of optical interference created by silver/silicon reflective surface on QDs fluorescence was systematically investigated. CdSe/ZnS QDs and QDs-merocyanine conjugate were placed in front of reflective silver/silicon surface at different distance by poly vinyl alcohol (PVA) spacer layers of different thickness to monitor the effect of optical interference on their excited state lifetime and its implication in biological arena (quantum yield calculation of intrinsic fluorophore) and in technological perspective (OLED, QDs based solar cell). In this direction, a quantitative and mechanistic study on excited state fluorescence lifetime of QDs on contact mode of silver film was carried out in order to understand the photon-plasmon interaction phenomenon.

1.2. Objective:

Protein is the key biological macromolecules which perform a vast array of functions within living organisms, including catalyzing metabolic reactions, replicating DNA, responding to stimuli, and transporting molecules from one location to another. To understand its activity and other structural and functional properties, thorough understanding of the energetics and dynamics of confined biological water molecules and protein's side chain flexibility at the cavity or binding site is very much essential. One of the model, protein endogenous serum albumin (ESA), is reported to be responsible for the binding of an anticancer drug doxorubicin [10] in domain I. The objective is to rationalize the cavity water dynamics and energetics of the protein by studying well characterized fluorescent probe acrylodan. The comparative study on biomimetic using the probe explores the possibility of drug delivery and other therapeutic applications.

Protein-DNA interactions play a crucial role in central biological processes, ranging from the mechanism of replication, transcription and recombination to enzymatic events utilizing nucleic acids as substrates. Various external and internal factors influence the interaction between protein-DNA. While considering the binding nature and extent of interaction, one need to account the hydrophobic effect, hydrogen bonding, DNA base pair sequences, shape complementarity, Vander wall repulsion etc. In this context, the present study exploits the unique opportunity to study a model protein-DNA complex comprising of lambda repressor (λ -repressor) protein and the two operator DNA sites, O_{R1} and O_{R2}. The study aims to unearth dynamical behavior of water molecules present in the DNA minor grooves and the flexibility of the DNA side chain in the process of protein-DNA complexation. The study of minor groove water molecules and the dynamical exchange of such water molecules with the bulk water molecules is one of the main motives of the study.

Molecular recognition process refers to the weak noncovalent interaction, which takes place selectively and specifically between small ligand molecules with biological macromolecules. Understanding of such recognition in biological and biomimetic milieu is the central attraction for drug designing, which is crucial for the improvement of human healthcare. A thorough knowledge of the structural, dynamical and energetic parameters that dictate such molecular interactions can find immense use in the modulations of the ligand-macromolecule recognition process. To explore the molecular recognition and fast kinetics in greater depth with superior time resolution, an optofluidics platform was ingeniously developed. The optofluidics platform enable to collect spectroscopic and microscopic data simultaneously providing a better analytical tool to understand and envisage various chemical and biological processes.

Excited state photo-physical behaviour is often used as a marker for various fields including molecular interaction, photo device performance. It has been established that the excited state photophysical behaviour or emission property is not always inherent, rather it is immensely influenced by the immediate environments. In this study, our objective is to make a technologically relevant confined environment and to explore the photophysical properties of a FRET (donor-acceptor) pair in the confined state. The study aims to explore the critical role of optical interference in excited state energy transfer process.

Direct contact of the photon sources with metallic thin film is almost unavoidable for the realization of several photonic devices, including plasmonically coupled single photon transistors. A few detailed systematic studies of the excitonic dynamics of photon sources in contact with plasmonically active metal film is present in the current literature. The objective of the study is to systematically investigate the excited state photophysical behaviour of QDs in contact mode of metallic surface. The study aims to decouple several possible competitive process like charge migration, nanosurface energy transfer, resonance

energy transfer, which might have played significant role in excited state lifetime alteration.

1.3. Summary of the work done:

1.3.1. Time-resolved spectroscopic studies on biological and engineered environments:

1.3.1.1. Picosecond-resolved solvent reorganization and energy transfer in biological and model cavities [40]: In this study, we have explored picosecond-resolved solvation dynamics of water molecules and associated polar amino acids in the hydrophobic cleft around Cys 34 position of endogenous serum albumin (ESA). While site selective acrylodan labeling to Cys 34 allows us to probe solvation in the cleft, FRET from intrinsic fluorescent amino acid Trp 214 to the extrinsic probe acrylodan reports the structural integrity of the protein in our experimental condition. Temperature dependent solvation in the cleft clearly shows that the dynamics follows Arrhenius type behavior up to 60 °C, after which a major structural perturbation of the protein is evident. The study also monitors polarization gated dynamics of the acrylodan probe and FRET from Trp 214 to acrylodan at various temperatures. The dynamical behavior of the immediate environments around the probe acrylodan in the cleft has been compared with a model biomimetic cavity of a reverse micelle ($w_0=5$). We have also estimated possible distribution of donor-acceptor distances in the protein and reverse micelles. The study reveals that the energetics of the water molecules in the biological cleft is comparable to that in the model cavity indicating a transition from bound state to quasibound state, closely consistent with existing MD simulation study.

1.3.2. Spectroscopic studies on the interfacial dynamics at a specific protein-DNA interface:

1.3.2.1. Ultrafast interfacial solvation dynamics in specific protein DNA recognition [41]: An overwhelming number of structural and functional studies on specific protein-DNA complexes reveal the existence of water molecules at the interaction interface. What role does the interfacial water molecules play in determining the specificity of association is thus a critical question. Herein, we have explored the dynamical role of minor groove water molecules and DNA side chain flexibility in lambda repressor-operator DNA interaction using well-characterized DNA minor groove binder dye, H258. The most striking finding of our studies reveals that the solvation time scale corresponding to the minor groove water molecules (~50 ps) and DNA side chain flexibility (~10 ns) remain unaltered even in protein-DNA complex in comparison to unbound operator DNA. The temperature dependent study further reveals the slower exchange of minor groove water molecules with bulk water in DNA-protein complex in comparison to the unbound DNA. Detailed structural studies including circular dichroism and FRET were performed to elucidate the interaction between protein and DNA.

1.3.3. Development of an engineered platform for the detection of very fast molecular/biomolecular interaction:

1.3.3.1. An improved microfluidics approach for monitoring real-time interaction profiles of ultrafast molecular recognition [34]: The study illustrates the development of a microfluidics platform combining fluorescence microscopy and femtosecond/picosecond-resolved spectroscopy to investigate ultrafast chemical processes in liquid-phase diffusion-controlled reactions. By controlling the flow rates of two reactants in a specially designed microfluidics chip, sub-100 ns time resolution for the exploration of chemical intermediates of the reaction in

the microchannel has been achieved. The developed system clearly rules out the possibility of formation of any intermediate reaction product in a so-called fast ionic reaction between sodium hydroxide and phenolphthalein, and reveals a microsecond time scale associated with the formation of the reaction product. The developed system was used for the investigation of intermediate states in the molecular recognition of various macromolecular self-assemblies (micelles) and genomic DNA by small organic ligands (H258 and ethidium bromide). The microfluidics based system is proposed to be an alternative to the existing millisecond-resolved “stopped-flow” technique for a broad range of time-resolved (sub-100 ns to minutes) experiments on complex chemical/biological systems.

1.3.4. Spectroscopic studies on the ultrafast migration of radiation at the engineered dielectric interface:

1.3.4.1. Förster resonance energy transfer in a nanoscopic system on dielectric interfaces [42]: The study investigates picosecond-resolved energy transfer between a quantum dot (donor) and an organic molecule (acceptor) in the proximity of a reflecting metallic/non-metallic surface. It was experimentally demonstrated that the FRET is significantly influenced by the proximity of the mirror. Locating CdSe quantum dots (donor) attached to an organic dye merocyanine (acceptor) at well-defined positions from the reflecting silver/silicon surface allows the transfer rate to be determined as a function of distance from the surface. An attempt to fit the experimental data to a model relying upon the change of the apparent energy transfer rate due to interference of direct and reflected light waves reveals reasonably good results. The results show that the observed FRET efficiency in a donor-acceptor pair on the mirror surface is oscillating in nature, providing information for the measured energy transfer, which could be potentially different from that of the actual transfer due to optical interference. This new understanding can be put forward to practical use. The

theoretical model fit for conjugate dipolar system having lifetime dependency on surface-dipole separation could provide useful information about the intrinsic quantum efficiency of the emitting dipole, which is otherwise not obtainable by general approach of quantum efficiency estimation using standard steady state and time-resolved technique.

1.3.5. Ultrafast spectroscopic studies on the photon-plasmon interaction at a technologically important interface:

1.3.5.1. Ultrafast dynamics of excitons in semiconductor quantum dots on a plasmonically active nano-structured silver film [43]: The excited state dynamics of core-shell type semiconductor QDs of various sizes in close contact with a plasmonically active silver thin film has been demonstrated by using picosecond resolved fluorescence spectroscopy. The non-radiative energy transfer from the QDs to the metal surface is found to be of FRET type rather than the widely expected nano-surface energy transfer (NSET) type. The slower rate of energy transfer processes compared to that of the electron transfer from the excited QDs to benzoquinone reveals an insignificant possibility of charge migration from the QDs to the metallic film. Though charge migration from the QDs to silver film is expected, yet it is not realized due to the formation of Schottky barrier.

1.4. Plan of thesis:

The plan of the thesis is as follows:

Chapter 1: This chapter gives a brief introduction to the scope and motivation behind the thesis work. A brief summary of the work done is also included in this chapter.

Chapter 2: This chapter provides a brief overview of the steady-state and dynamical tools, the structural aspects of biologically important systems (proteins,

biomimetic, engineered environments etc.) and fluorescent probes used in the experiments.

Chapter 3: Details of instrumentation, data analysis and experimental procedures have been discussed in this chapter.

Chapter 4: In this chapter, role of biological/biomimetic cavity on fluorescent probes is addressed. The ultrafast relaxation of water molecules around the probe within the cavity enlighten the nature of water transition and other photophysical aspects.

Chapter 5: Study on interfacial solvation dynamics of fluorescent probes in specific protein-DNA interaction between λ -repressor and different operator DNA is the elaborated in this chapter.

Chapter 6: The indigenously developed optofluidics platform and its applicability in molecular recognition and fast kinetic measurement is discussed in the chapter.

Chapter 7: In this chapter, role of reflective surface on the resonance energy transfer from donor to acceptor molecules is elaborated. Also the implication of optical interference in energy transfer process in technological viewpoint is exemplified.

Chapter 8: Spectroscopic studies on photon-plasmon interaction and its effect in fluorescence property of semiconductor QDs is discussed in this chapter.

References

1. W. Liu, M. Howarth, A.B. Greytak, Y. Zheng, D.G. Nocera, A.Y. Ting and M.G. Bawendi, Compact biocompatible quantum dots functionalized for cellular imaging. *J. Am. Chem. Soc.*, **130** (2008) 1274.
2. S.K. Pal, J. Peon and A.H. Zewail, Biological water at the protein surface: Dynamical solvation probed directly with femtosecond resolution. *Proc. Natl. Acad. Sci. USA*, **99** (2002) 1763.
3. J. Hofkens, M. Cotlet, T. Vosch, P. Tinnefeld, K.D. Weston, C. Ego, A. Grimsdale, K. Mullen, D. Beljonne, J.L. Bredas, S. Jordens, G. Schweitzer, M. Sauer and F. De Schryver, Revealing competitive Förster-type resonance energy-transfer pathways in single bichromophoric molecules. *Proc. Natl. Acad. Sci. USA*, **100** (2003) 13146.
4. T.-H. Zhang, J. Luo and J.-M. Zhou, Conformational changes at the active site of adenylate kinase detected using a fluorescent probe and monoclonal antibody binding. *Biochimie*, **84** (2002) 335.
5. D. Andreatta, S. Sen, J.L. Pérez Lustres, S.A. Kovalenko, N.P. Ernsting, C.J. Murphy, R.S. Coleman and M.A. Berg, Ultrafast dynamics in DNA: “Fraying” at the end of the helix. *J. Am. Chem. Soc.*, **128** (2006) 6885.
6. J.K.A. Kamal, L. Zhao and A.H. Zewail, Ultrafast hydration dynamics in protein unfolding: Human serum albumin. *Proc. Natl. Acad. Sci. USA*, **101** (2004) 13411.
7. K. Flora, J.D. Brennan, G.A. Baker, M.A. Doody and F.V. Bright, Unfolding of acrylodan-labeled human serum albumin probed by steady-state and time-resolved fluorescence methods. *Biophys. J.*, **75** (1998) 1084.
8. H.T. He and D. Marguet, Detecting nanodomains in living cell membrane by fluorescence correlation spectroscopy. *Annu. Rev. Phys. Chem.*, **62** (2011) 417.

9. B. Wu, K.D. Piatkevich, T. Lionnet, R.H. Singer and V.V. Verkhusha, Modern fluorescent proteins and imaging technologies to study gene expression, nuclear localization, and dynamics. *Curr. Opin. Cell Biol.*, **23** (2011) 310.
10. S. Sengupta, K.K. Dey, H.S. Muddana, T. Tabouillot, M.E. Ibele, P.J. Butler and A. Sen, Enzyme molecules as nanomotors. *J. Am. Chem. Soc.*, **135** (2013) 1406.
11. A. Eremenko, N. Smirnova, O. Rusina, O. Linnik, T.B. Eremenko, L. Spanhel and K. Rechthaler, Photophysical properties of organic fluorescent probes on nanosized TiO₂/SiO₂ systems prepared by the sol-gel method. *J. Mol. Struct.*, **553** (2000) 1.
12. S.L. Veatch, I.V. Polozov, K. Gawrisch and S.L. Keller, Liquid domains in vesicles investigated by NMR and fluorescence microscopy. *Biophys. J.*, **86** (2004) 2910.
13. Y. Umezawa, Assay and screening methods for bioactive substances based on cellular signaling pathways. *Rev. Mol. Biotechnol.*, **82** (2002) 357.
14. X. Chen, Y. Zhou, X. Peng and J. Yoon, Fluorescent and colorimetric probes for detection of thiols. *Chem. Soc. Rev.*, **39** (2010) 2120.
15. M. Sameiro and T. Goncalves, Fluorescent labeling of biomolecules with organic probes. *Chem. Rev.*, **109** (2009) 190.
16. M. Green, Semiconductor quantum dots as biological imaging agents. *Angew. Chem. Int. Ed.*, **43** (2004) 4129.
17. J.M. Klostranec and W.C.W. Chan, Quantum dots in biological and biomedical research: Recent progress and present challenges. *Adv. Mater.*, **18** (2006) 1953.
18. A. Ruland, C. Schulz-Drost, V. Sgobba and D.M. Guldi, Enhancing photocurrent efficiencies by resonance energy transfer in CdTe quantum dot multilayers: Towards rainbow solar cells. *Adv. Mater.*, **23** (2011) 4573.

19. M. Bruchez, M. Moronne, P. Gin, S. Weiss and A.P. Alivisatos, Semiconductor nanocrystals as fluorescent biological labels. *Science*, **281** (1998) 2013.
20. E.M. Purcell, Spontaneous emission probabilities at radio frequencies. *Phys. Rev.*, **69** (1946) 681.
21. K.H. Drexhage, Influence of a dielectric interface on fluorescence decay time. *J. Lumin.*, **1-2** (1970) 693.
22. R.R. Chance, A. Prock and R. Silbey, Molecular fluorescence and energy transfer near interfaces. *Adv. Chem. Phys.*, **37** (1978) 1.
23. P. Lodahl, A.F.v. Driel, I.S. Nikolaev, A. Irman, K. Overgaag, D.I. Vanmaekelbergh and W.L. Vos, Controlling the dynamics of spontaneous emission from quantum dots by photonic crystals. *Nature*, **430** (2004) 654.
24. Y. Cesa, C. Blum, J.M. van den Broek, A.P. Mosk, W.L. Vos and V. Subramaniam, Manipulation of the local density of photonic states to elucidate fluorescent protein emission rates. *Phys. Chem. Chem. Phys.*, **11** (2009) 2525.
25. M.D. Leistikow, J. Johansen, A.J. Kettelarij, P. Lodahl and W.L. Vos, Size-dependent oscillator strength and quantum efficiency of CdSe quantum dots controlled via the local density of states. *Phys. Rev. B*, **79** (2009) 045301.
26. E.M. Purcell, Life at low Reynolds number. *Am. J. Phys.*, **45** (1977) 3.
27. J.Y. Zhang, X.Y. Wang and M. Xiao, Modification of spontaneous emission from CdSe/CdS quantum dots in the presence of a semiconductor interface. *Opt. Lett.*, **27** (2002) 1253.
28. N.E. Levinger, Water in confinement. *Science*, **298** (2002) 1722.
29. P.L. Luisi and B.E. Straub, Reverse micelles: Biological and technological relevance of amphiphilic structures in apolar media. 1984, New York: Plenum.

30. R. Masuch and D.A. Moss, Stopped flow apparatus for time-resolved Fourier transform infrared difference spectroscopy of biological macromolecules in (H₂O)-H-1. *Appl. Spectrosc.*, **57** (2003) 1407.
31. G. Feng and T. Jia, A millisecond infrared stopped-flow apparatus. *Appl. Spectrosc.*, **60** (2006) 1477.
32. M.G. Whitesides, The origins and the future of microfluidics. *Nature*, **442** (2006) 368.
33. C. Wang, S.J. Li, Z.Q. Wu, J.J. Xu, H.Y. Chen and X.H. Xia, Study on the kinetics of homogeneous enzyme reactions in a micro/nanofluidics device. *Lab Chip*, **10** (2010) 639.
34. S. Batabyal, S. Rakshit, S. Kar and S.K. Pal, An improved microfluidics approach for monitoring real-time interaction profiles of ultrafast molecular recognition. *Rev. Sci. Instrum.*, **83** (2012) 043113.
35. Y. Gambin, C. Simonnet, V. VanDelinder, A. Deniz and A. Groisman, Ultrafast microfluidic mixer with three-dimensional flow focusing for studies of biochemical kinetics. *Lab Chip*, **10** (2010) 598.
36. P. Andrew and W.L. Barnes, Energy transfer across a metal film mediated by surface plasmon polaritons. *Science*, **306** (2004) 1002.
37. P. Andrew and W.L. Barnes, Förster energy transfer in an optical microcavity. *Science*, **290** (2000) 785.
38. N. Mohan, C.S. Chen, H.H. Hsieh, Y.C. Wu and H.C. Chang, In vivo imaging and toxicity assessments of fluorescent nanodiamonds in *caenorhabditis elegans*. *Nano Lett.*, **10** (2010) 3692.
39. L. Xiao, Y. Zhang, S.S. Berr, M.D. Chordia, P. Pramoonjago, L. Pu and D.F. Pan, A novel near-infrared fluorescence imaging probe for in vivo neutrophil tracking. *Mol Imaging.*, **11** (2012) 372.
40. S. Batabyal, T. Mondol and S.K. Pal, Picosecond-resolved solvent reorganization and energy transfer in biological and model cavities. *Biochimie*, **95** (2013) 1127.

41. S. Batabyal, T. Mondol, S. Choudhury, A. Mazumder and S.K. Pal, Ultrafast interfacial solvation dynamics in specific protein DNA recognition. *Biochimie*, **95** (2013) 2168.
42. S. Batabyal, T. Mondol, K. Das and S.K. Pal, Förster resonance energy transfer in a nanoscopic system on a dielectric interface. *Nanotechnology*, **23** (2012) 495402.
43. S. Batabyal, A. Makhal, K. Das, A.K. Raychaudhuri and S.K. Pal, Ultrafast dynamics of excitons in semiconductor quantum dots on a plasmonically active nano-structured silver film. *Nanotechnology*, **22** (2011) 195704.

Chapter 2

An overview of experimental techniques and systems

In order to investigate the various processes involved in the course of study on the fluorescent robes in biologically relevant engineered environments, different steady-state and dynamical tools have been employed. These include solvation dynamics, fluorescence anisotropy, Förster resonance energy transfer (FRET), determination of activation energy barrier using Arrhenius theory, Twisted intramolecular charge transfer (TICT), Nano surface energy transfer (NSET), diffusion studies, and Circular dichroism (CD). In this chapter, brief discussions about these tools and an overview of various systems used in our studies have been provided.

2.1. Steady-state and dynamical tools:

2.1.1. Solvation dynamics:

2.1.1.1. Theory: Solvation dynamics refer to the process of reorganization of solvent dipoles around a dipole created instantaneously or an electron/proton injected suddenly in a polar liquid. In order to understand the meaning and scope of solvation dynamics, let us first visualize the physical essence of the dynamical process involved for a solute molecule in a polar solvent [1]. A change in the probe (solute) is made at time $t=0$, by an excitation pulse, which leads to the creation of a dipole. This dipole gives rise to an instantaneous electric field on the solvent molecules. The interaction of permanent dipoles of the solvent with the instantaneously created electric field, shifts the free energy minimum of the solvent to a non-zero value of the polarization. The solvent motion is crucial (Figure 2.1). Since the probe is excited instantaneously (a Franck-Condon transition as far as the nuclear degrees of freedom are concerned), the solvent molecules at $t=0$ find themselves in a relatively high-energy configuration.

Subsequently, the solvent molecules begin to move and rearrange themselves to reach their new equilibrium positions (Figure 2.2). The nuclear motion involved can be broadly classified into rotational and translational motions.

When the solvent is bulk water, rotational motion would also include hindered rotation and libration, while translation would include the intermolecular vibration due to the extensive hydrogen bonding. The two specific motions, libration and intermolecular vibration, are relatively high in frequency and are expected to play a dominant role in the initial part of solvation [2]. The molecular motions involved are shown schematically in

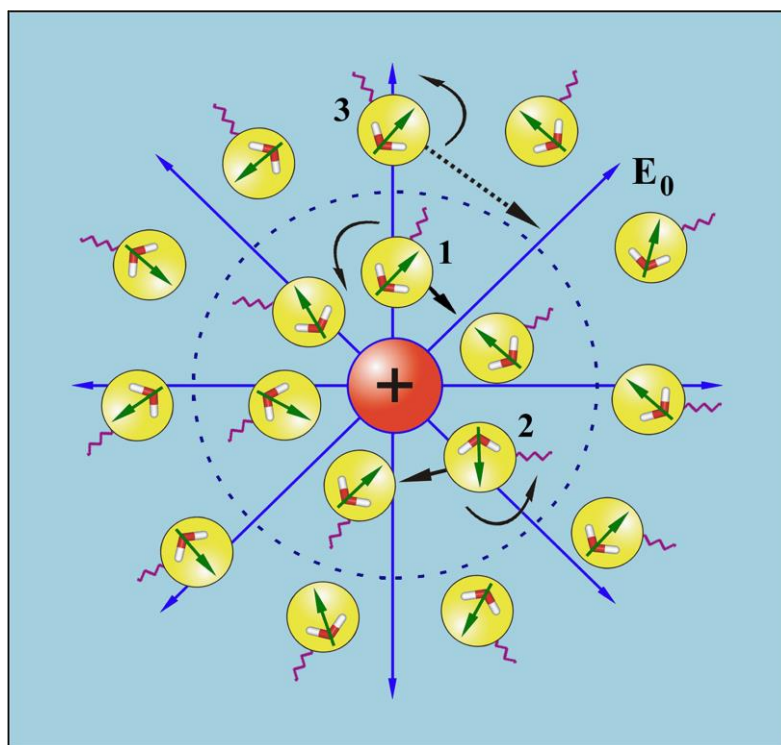


Figure 2.1. Schematic illustration of solvation of an ion (or dipole) by water. The neighboring molecules (numbered 1 and 2) can either rotate or translate to attain the minimum energy configuration. On the other hand, distant water molecule 3 can only rotate to attain minimum energy configuration. The field is shown as E_0 . The springs connected to the molecules are meant to denote hydrogen bonding.

Figure 2.1, and in Figure 2.3 a typical solvation time correlation function is depicted. For clarity, we approximate the motions responsible for the decay in different regions.

A simple way to address the dynamics of polar solvation is to start with the following expression for the solvation energy, $E_{solv}(t)$ [3],

$$E_{solv}(t) = -\frac{1}{2} \int dr E_0(r) \cdot P(r,t) \quad (2.1)$$

where $E_0(r)$ is the instantaneously created, position-dependent electric field from the ion or the dipole of the solute and $P(r,t)$ is the position and time-dependent polarization.

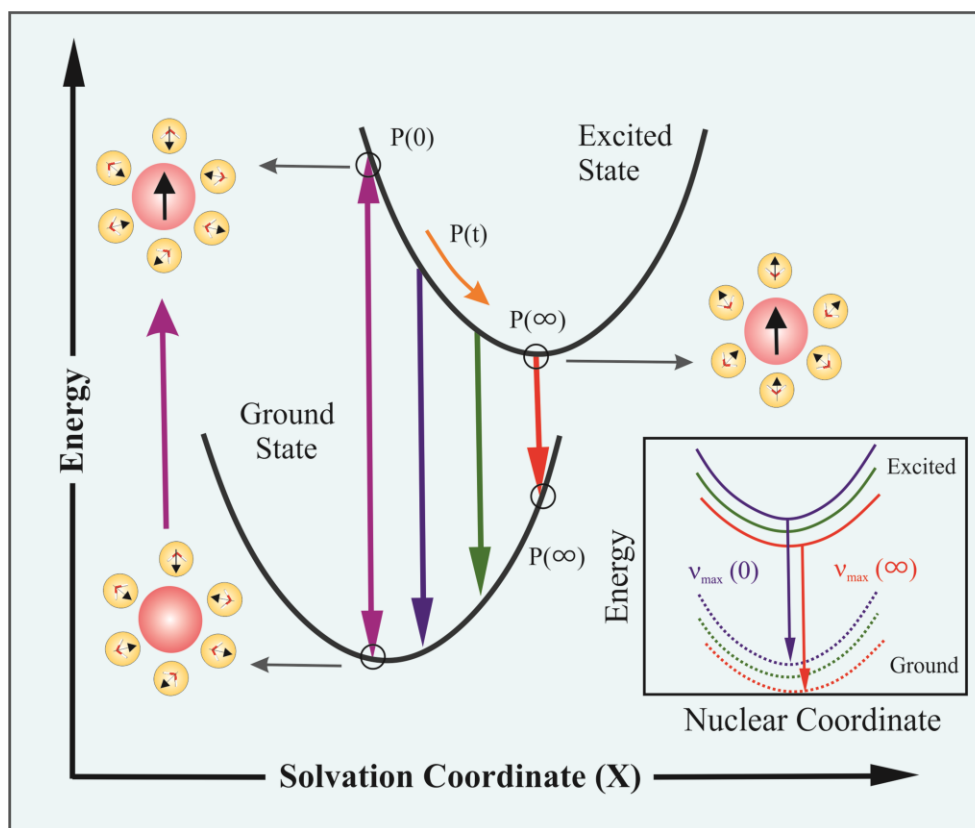


Figure 2.2. Schematic representation of the potential energy surfaces involved in solvation dynamics showing the water orientational motions along the solvation coordinate together with instantaneous polarization P . In the inset we show the change in the potential energy along the intramolecular nuclear coordinate. As solvation proceeds the energy of the solute comes down giving rise to a red shift in the fluorescence spectrum. Note the instantaneous P , e.g., $P(\infty)$, on the two connected potentials.

The latter is defined by the following expression,

$$P(r, t) = \partial dWm(W)r(r, W, t) \quad (2.2)$$

where $\mu(\Omega)$ is the dipole moment vector of a molecule at position r , and $\rho(r, \Omega, t)$ is the position, orientation and time-dependent density. Therefore, the time dependence of the solvation energy is determined by the time dependence of polarization that is in turn determined by the time dependence of the density. If the perturbation due to the probe on dynamics of bulk water is negligible, then the time dependence of polarization is dictated by the natural dynamics of the liquid. The theoretical analysis of the time-dependent density is usually carried out using a molecular hydrodynamic approach that is based on the basic conservation (density, momentum and energy) laws and includes the effects of intermolecular (both spatial and orientational) correlations. The latter provides the free energy surface on which solvation proceeds. The equation of motion of the density involves both orientational and translational motions of the solvent molecules.

The details of the theoretical development are reported in literature [1]; here we shall present a simple physical picture of the observed biphasic solvation dynamics. Within linear response theory, the solvation correlation function is directly related to the solvation energy as,

$$C(t) = \frac{\langle \delta E(0) \cdot \delta E(t) \rangle}{\langle \delta E^2 \rangle} = \frac{\langle E(t) \rangle - \langle E(\infty) \rangle}{\langle E(0) \rangle - \langle E(\infty) \rangle} \quad (2.3)$$

where δE is the fluctuation of solvation energy from the average, equilibrium value. Note that the equality in equation (2.3) indicates the direct relation for the average of the fluctuations over the equilibrium distribution (left) and the non-equilibrium function (right) which relates to observables; without $\langle E(\infty) \rangle$ the correspondence is clear, and $\langle E(\infty) \rangle$ is rigorously the result of the equilibrium term in the numerator and for normalization in the denominator.

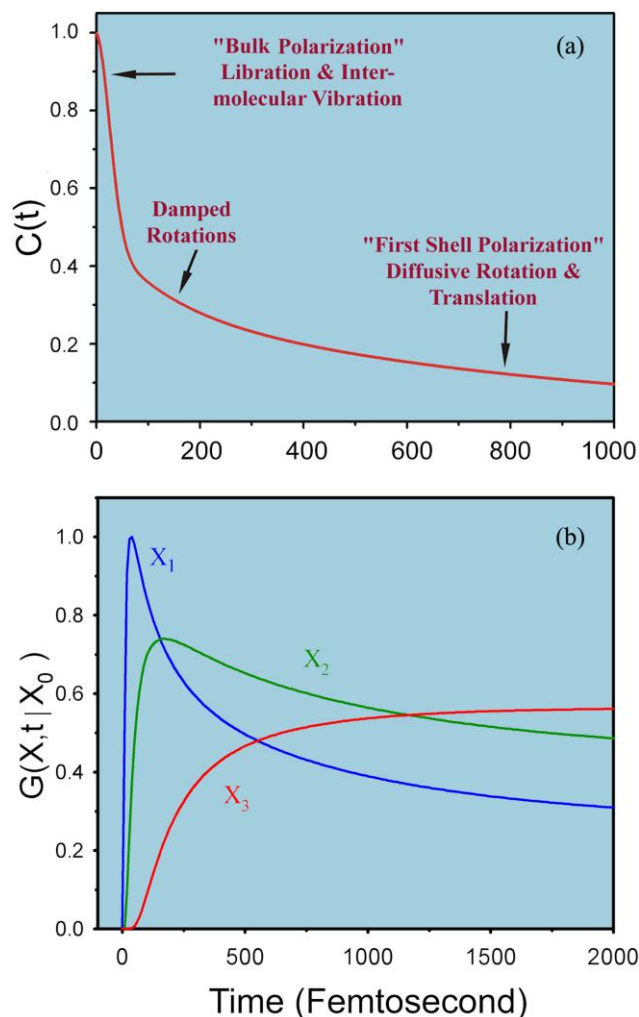


Figure 2.3. (a) A typical solvation time correlation function for water is shown here. The time correlation function exhibits three distinct regions: The initial ultrafast decay, an intermediate decay of about 200 fs and the last slow decay with time constant of 1 ps. The physical origin of each region is indicated on the plot itself; see text. (b) Green's function $G(X, t | X_0)$ for population relaxation along the solvation coordinate (X) is plotted against time in femtosecond. In G , X_0 is the initial position at $t = 0$. This Figure shows the position and time dependence of the population fluorescence intensity. At early times (when the population is at X_1) there is ultrafast rise followed by an ultrafast decay. At intermediate times (when the population is at X_2) there is a rise followed by a slow decay as shown by the green line. At long times when the population is nearly relaxed (position X_3 , red line) we see only a rise.

The ultrafast component in the solvation time correlation function (see Figure 2.3a), originates from the initial relaxation in the steep collective solvation potential. The collective potential is steep because it involves the total polarization of the system [1, 4]. This initial relaxation couples mainly to the hindered rotation

(i.e., libration) and the hindered translation (i.e., the intermolecular vibration), which are the available high frequency modes of the solvent; neither long amplitude rotation nor molecular translation are relevant here. The last part in the decay of the solvation correlation function involves larger amplitude rotational and translational motions of the nearest neighbor molecules in the first solvation shell. In the intermediate time, one gets contributions from the moderately damped rotational motions of water molecules. In a sense, with the above description one recovers the famous Onsager's "inverse snow-ball" picture of solvation [5]. The slowest time constant is ~ 1 ps, which is determined by the individual rotational and translational motions of the molecules in the "first solvation shell" nearly close to the probe. The femtosecond component is dominated by the high frequency hindered rotational and translational (vibration) polarization [6].

Figure 2.2 shows a schematic of the solvation potential and the orientational motions for the water molecules involved. From the shape of the potential, it can be seen that the transient behavior for the population during solvation should be a decay function on the blue edge of the spectrum and a rise function on the red edge. These wavelength-dependent features can be explained nicely within a generalized model of relaxation in which a Gaussian wave packet relaxes on a harmonic surface. The relaxation is non-exponential and a Green's function can describe the approach of the wave packet along the solvation coordinate, X , to its equilibrium value. For the general non-Markovian case it is given by [7],

$$G(X, t | X_0) = \frac{1}{\sqrt{2\pi \langle X^2 \rangle [1 - C^2(t)]}} \exp \left[-\frac{[X - X_0 C(t)]^2}{2 \langle X^2 \rangle [1 - C^2(t)]} \right] \quad (2.4)$$

where $\langle X^2 \rangle$ is the equilibrium mean square fluctuation of the polarization coordinate in the excited state surface, $C(t)$ is the solvation correlation function described in equation (2.3) and X_0 is the initial value of the packet on the solvation coordinate. Equation (2.4) describes the motion of the wave packet (polarization

density) beginning at $t = 0$ (X_0) as a delta function and according to the solvation time correlation function. As $t \rightarrow \infty$, $C(t) \rightarrow 0$ and we recover the standard Gaussian distribution. Initially, ($t \rightarrow 0$), the exponential is large, so the decay is ultrafast, but at long times, the relaxation slows down, ultimately to appear as a rise. In Figure 2.3b, we present calculations of $G(X, t | X_0)$ at different positions along the solvation coordinate giving decays at X_1 and X_2 , but with different time constants, and a rise at X_3 , as demonstrated experimentally.

2.1.1.2. Experimental methods: In order to study solvation stabilization of a probe in an environment, a number of fluorescence transients are taken at different wavelengths across the emission spectrum of the probe. As described earlier, blue and red ends of the emission spectrum are expected to show decay and rise, respectively in the transients. The observed fluorescence transients are fitted by using a nonlinear least square fitting procedure to a function,

$$\left(X(t) = \int_0^t E(t') R(t-t') dt' \right) \quad (2.5)$$

comprising of convolution of the instrument response function (IRF) ($E(t)$) with a sum of exponentials,

$$\left(R(t) = A + \sum_{i=1}^N B_i \exp(-t/\tau_i) \right) \quad (2.6)$$

with pre-exponential factors (B_i), characteristic lifetimes (τ_i) and a background (A). Relative concentration in a multiexponential decay is finally expressed as;

$$\alpha_n = \frac{B_n}{\sum_{i=1}^N B_i} \quad (2.7)$$

The relative contribution of a particular decay component (f_n) in the total fluorescence is defined as,

$$f_n = \frac{\tau_n B_n}{\sum_{i=1}^N B_i \tau_i} \times 100. \quad (2.8)$$

The quality of the curve fitting is evaluated by reduced chi-square (0.9-1.1) and residual data. The purpose of the fitting is to obtain the decays in an analytical form suitable for further data analysis.

To construct time resolved emission spectra (TRES) we follow the technique described in references [8]. As described above, the emission intensity decays are analyzed in terms of the multiexponential model,

$$I(\lambda, t) = \sum_{i=1}^N \alpha_i(\lambda) \exp(-t/\tau_i(\lambda)) \quad (2.9)$$

where $\alpha_i(\lambda)$ are the pre-exponential factors, with $\sum \alpha_i(\lambda) = 1.0$. In this analysis we compute a new set of intensity decays, which are normalized so that the time-integrated intensity at each wavelength is equal to the steady-state intensity at that wavelength. Considering $F(\lambda)$ to be the steady-state emission spectrum, we calculate a set of $H(\lambda)$ values using,

$$H(\lambda) = \frac{F(\lambda)}{\int_0^{\infty} I(\lambda, t) dt} \quad (2.10)$$

which for multiexponential analysis becomes,

$$H(\lambda) = \frac{F(\lambda)}{\sum_i \alpha_i(\lambda) \tau_i(\lambda)} \quad (2.11)$$

Then, the appropriately normalized intensity decay functions are given by,

$$I'(\lambda, t) = H(\lambda) I(\lambda, t) = \sum_{i=1}^N \alpha'_i(\lambda) \exp(-t/\tau_i(\lambda)) \quad (2.12)$$

where $\alpha'_i(\lambda) = H(\lambda) \alpha_i(\lambda)$. The values of $I'(\lambda, t)$ are used to calculate the intensity at any wavelength and time, and thus the TRES. The values of the emission maxima and spectral width are determined by nonlinear least-square fitting of the spectral shape of the TRES. The spectral shape is assumed to follow a lognormal line shape [8, 9],

$$I(\bar{\nu}) = I_0 \exp \left\{ - \left[\ln 2 \left(\frac{\ln(\alpha + 1)}{b} \right)^2 \right] \right\} \quad (2.13)$$

with $\alpha = \frac{2b(\bar{\nu} - \bar{\nu}_{\max})}{\Delta} - 1$ where I_0 is amplitude, $\bar{\nu}_{\max}$ is the wavenumber of the emission maximum and spectral width is given by, $\Gamma = \Delta \left[\frac{\sinh(b)}{b} \right]$. The terms b and Δ are asymmetry and width parameters, respectively and equation (2.9) reduces to a Gaussian function for $b=0$.

The time-dependent fluorescence Stokes shifts, as estimated from TRES are used to construct the normalized spectral shift correlation function or the solvent correlation function $C(t)$ and is defined as,

$$C(t) = \frac{\bar{\nu}(t) - \bar{\nu}(\infty)}{\bar{\nu}(0) - \bar{\nu}(\infty)} \quad (2.14)$$

where, $\bar{\nu}(0)$, $\bar{\nu}(t)$ and $\bar{\nu}(\infty)$ are the emission maxima (in cm^{-1}) of the TRES at time zero, t and infinity, respectively. The $\bar{\nu}(\infty)$ value is considered to be the emission frequency beyond which insignificant or no spectral shift is observed. The $C(t)$ function represents the temporal response of the solvent relaxation process, as occurs around the probe following its photoexcitation and the associated change in the dipole moment.

In order to further investigate possible heterogeneity in the positional distribution of fluoroprobes at the interfaces of biomimicking self-assemblies we follow time-resolved area normalized emission spectroscopy (TRANES), which is a well-established technique [10, 11] and is a modified version of TRES. TRANES were constructed by normalizing the area of each spectrum in TRES such that the area of the spectrum at time t is equal to the area of the spectrum at $t = 0$. A useful feature of this method is the presence of an isoemissive point in the spectra involves emission from two species, which are kinetically coupled either irreversibly or reversibly or not coupled at all.

2.1.2. Fluorescence anisotropy: Anisotropy is defined as the extent of polarization of the emission from a fluorophore. Anisotropy measurements are commonly

used in biochemical applications of fluorescence. It provides information about the size and shape of proteins or the rigidity of various molecular environments. Anisotropy measurements have also been used to measure protein-protein associations, fluidity of membranes and for immunoassays of numerous substances. These measurements are based on the principle of photoselective excitation of those fluorophore molecules whose absorption transition dipoles are parallel to the electric vector of polarized excitation light. In an isotropic solution, fluorophores are oriented randomly. However, upon selective excitation, partially oriented population of fluorophores with polarized fluorescence emission results. The relative angle between the absorption and emission transition dipole moments determines the maximum measured anisotropy (r_0). The fluorescence anisotropy (r) and polarization (P) are defined by,

$$r = \frac{I_{\parallel} - I_{\perp}}{I_{\parallel} + 2I_{\perp}} \quad (2.15)$$

$$P = \frac{I_{\parallel} - I_{\perp}}{I_{\parallel} + I_{\perp}} \quad (2.16)$$

where the fluorescence intensities of vertically and horizontally polarized emission when the fluorophore is excited with vertically polarized light. Polarization and anisotropy are interrelated as,

$$r = \frac{2P}{3 - P} \quad (2.17)$$

$$P = \frac{3r}{2 + r} \quad (2.18)$$

Although polarization and anisotropy provides the same information, anisotropy is preferred since the latter is normalized by total fluorescence intensity ($I_T = I_{\parallel} + 2I_{\perp}$) and in case of multiple emissive species anisotropy is additive while polarization is not. Several phenomena, including rotational diffusion and energy transfer, can decrease the measured anisotropy to values lower than maximum

theoretical values. Following a pulsed excitation the fluorescence anisotropy, $r(t)$ of a sphere is given by,

$$r(t) = r_0 \exp(-t/\tau_{rot}) \quad (2.19)$$

where r_0 is the anisotropy at time $t = 0$ and τ_{rot} is the rotational correlation time of the sphere.

2.1.2.1. Theory: For a radiating dipole the intensity of light emitted is proportional to the square of the projection of the electric field of the radiating dipole onto the transmission axis of the polarizer. The intensity of parallel and perpendicular projections are given by,

$$I_{||}(\theta, \psi) = \cos^2 \theta \quad (2.20)$$

$$I_{\perp}(\theta, \psi) = \sin^2 \theta \sin^2 \psi \quad (2.21)$$

where θ and ψ are the orientational angles of a single fluorophore relative to the z and y-axis, respectively (Figure 2.4a). In solution, fluorophores remain in random distribution and the anisotropy is calculated by excitation photoselection. Upon photoexcitation by polarized light, the molecules having absorption transition moments aligned parallel to the electric vector of the polarized light have the highest probability of absorption. For the excitation polarization along z-axis, all molecules having an angle ψ with respect to the y-axis will be excited. The population will be symmetrically distributed about the z-axis. For experimentally accessible molecules, the value of ψ will be in the range from 0 to 2π with equal probability. Thus, the ψ dependency can be eliminated.

$$\langle \sin^2 \psi \rangle = \frac{\int_0^{2\pi} \sin^2 \psi d\psi}{\int_0^{2\pi} d\psi} = \frac{1}{2} \quad (2.22)$$

$$\text{and } I_{||}(\theta) = \cos^2 \theta \quad (2.23)$$

$$I_{\perp}(\theta) = \frac{1}{2} \sin^2 \theta \quad (2.24)$$

Consider a collection of molecules oriented relative to the z-axis with probability $f(\theta)$. Then, measured fluorescence intensities for this collection after photoexcitation are,

$$I_{||} = \int_0^{\pi/2} f(\theta) \cos^2 \theta d\theta = k \langle \cos^2 \theta \rangle \quad (2.25)$$

$$I_{\perp} = \frac{1}{2} \int_0^{\pi/2} f(\theta) \sin^2 \theta d\theta = \frac{k}{2} \langle \sin^2 \theta \rangle \quad (2.26)$$

where $f(\theta)d\theta$ is the probability that a fluorophore is oriented between θ and $\theta + d\theta$ and is given by,

$$f(\theta)d\theta = \cos^2 \theta \sin \theta d\theta \quad (2.27)$$

k is the instrumental constant. Thus, the anisotropy (r) is defined as,

$$r = \frac{3 \langle \cos^2 \theta \rangle - 1}{2} \quad (2.28)$$

when $\theta = 54.7^\circ$ i.e. when $\cos^2 \theta = 1/3$, the complete loss of anisotropy occurs. Thus, the fluorescence taken at $\theta = 54.7^\circ$ with respect to the excitation polarization is expected to be free from the effect of anisotropy and is known as magic angle emission. For collinear absorption and emission dipoles, the value of $\langle \cos^2 \theta \rangle$ is given by the following equation,

$$\langle \cos^2 \theta \rangle = \frac{\int_0^{\pi/2} \cos^2 \theta f(\theta) d\theta}{\int_0^{\pi/2} f(\theta) d\theta} \quad (2.29)$$

Substituting equation (2.27) in equation (2.29) one can get the value of $\langle \cos^2 \theta \rangle = 3/5$ and anisotropy value to be 0.4 (from equation (2.28)). This is the maximum value of anisotropy obtained when the absorption and emission dipoles are collinear and when no other depolarization process takes place. However, for most fluorophore, the value of anisotropy is less than 0.4 and it is dependent on the excitation wavelength. It is demonstrated that as the displacement of the

absorption and emission dipole occurs by an angle γ relative to each other, it causes further loss of anisotropy (reduction by a factor 2/5) [12] from the value obtained from equation (2.28). Thus, the value of fundamental anisotropy, r_0 is given by,

$$r_0 = \frac{2}{5} \left(\frac{3 \cos^2 \gamma - 1}{2} \right) \quad (2.30)$$

For any fluorophore randomly distributed in solution, with one-photon excitation, the value of r_0 varies from -0.20 to 0.40 for γ values varying from 90° to 0° .

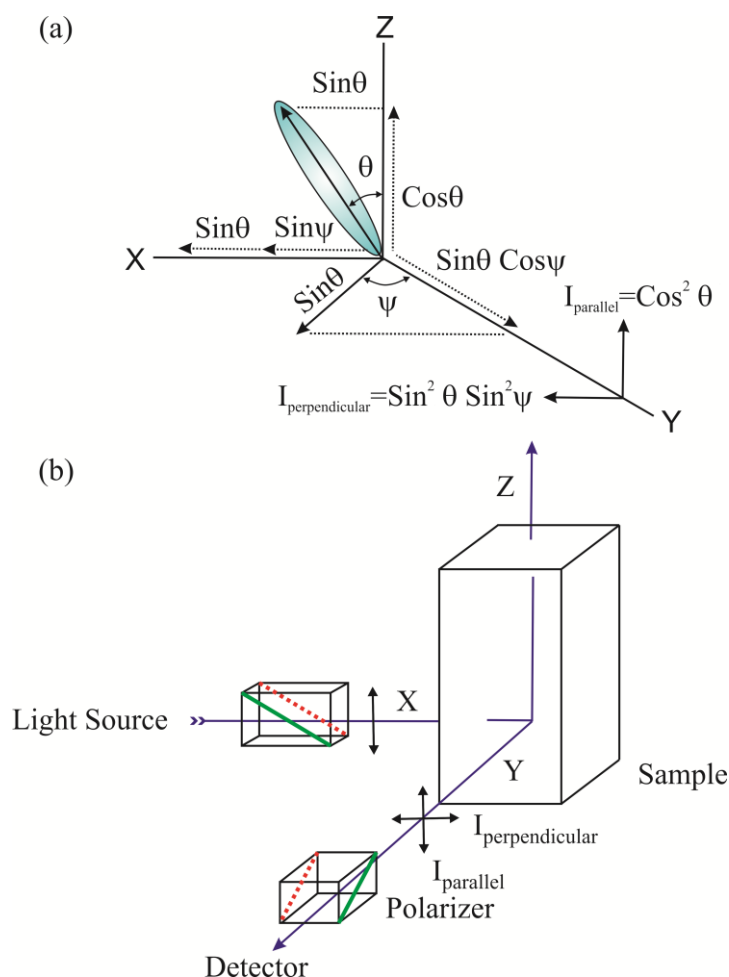


Figure 2.4. (a) Emission intensity of a single fluorophore (blue ellipsoid) in a coordinate system. (b) Schematic representation of the measurement of fluorescence anisotropy.

2.1.2.2. Experimental methods: For time resolved anisotropy ($r(t)$) measurements (Figure 2.4b), emission polarization is adjusted to be parallel and perpendicular to that of the excitation polarization. Spencer and Weber [13] have derived the relevant equations for the time dependence of $I_{||}(t)$ (equation (2.31)) and $I_{\perp}(t)$ (equation (2.32)) for single rotational and fluorescence relaxation times, τ_{rot} and τ_f , respectively,

$$I_{||}(t) = \exp(-t/\tau_f) (1 + 2r_0 \exp(-t/\tau_{rot})) \quad (2.31)$$

$$I_{\perp}(t) = \exp(-t/\tau_f) (1 - r_0 \exp(-t/\tau_{rot})) \quad (2.32)$$

The total fluorescence is given by,

$$F(t) = I_{||}(t) + 2I_{\perp}(t) = 3 \exp(-t/\tau_f) = F_0 \exp(-t/\tau_f) \quad (2.33)$$

The time dependent anisotropy, $r(t)$ is given by,

$$r(t) = \frac{I_{||}(t) - I_{\perp}(t)}{I_{||}(t) + 2I_{\perp}(t)} = r_0 \exp(-t/\tau_{rot}) \quad (2.34)$$

$F(t)$ depends upon τ_f and $r(t)$ depends upon τ_{rot} so that these two lifetimes can be separated. This separation is not possible in steady-state measurements. It should be noted that the degree of polarization (P) is not independent of τ_f and is therefore not as useful quantity as r . For reliable measurement of $r(t)$, three limiting cases can be considered.

- (a) If $\tau_f < \tau_{rot}$, the fluorescence decays before the anisotropy decays, and hence only r_0 can be measured.
- (b) If $\tau_{rot} < \tau_f$, in contrast to steady-state measurements, τ_{rot} can be measured in principle. The equations (2.31) and (2.32) show that the decay of the parallel and perpendicular components depends only upon τ_{rot} . The only experimental disadvantage of this case is that those photons emitted after the period of a few times τ_{rot} cannot contribute to the determination of τ_{rot} , but provided the signal-to-noise ratio is favorable, this need not be of great concern.

- (c) If $\tau_{rot} \approx \tau_f$, then it becomes the ideal situation since almost all photons are counted within the time (equal to several rotational relaxation times) in which $r(t)$ shows measurable changes.

For systems with multiple rotational correlation times, $r(t)$ is given by,

$$r(t) = r_0 \sum_i \beta_i e^{-t/\tau_i} \quad (2.35)$$

where $\sum_i \beta_i = 1$. It should be noted that the instrument monitoring the fluorescence, particularly the spectral dispersion element, responds differently to different polarizations of light, thus emerging the need for a correction factor. For example, the use of diffraction gratings can yield intensities of emission, which depend strongly upon orientation with respect to the plane of the grating. It is inevitably necessary when using such instruments to correct for the anisotropy in response. This instrumental anisotropy is usually termed as G-factor (grating factor) and is defined as the ratio of the transmission efficiency for vertically polarized light to that for horizontally polarized light ($G = I_{\parallel} + I_{\perp}$). Hence, values of fluorescence anisotropy, $r(t)$ corrected for instrumental response, would be given by [12],

$$r(t) = \frac{I_{\parallel}(t) - GI_{\perp}(t)}{I_{\parallel}(t) + 2GI_{\perp}(t)} \quad (2.36)$$

The G-factor at a given wavelength can be determined by exciting the sample with horizontally polarized excitation beam and collecting the two polarized fluorescence decays, one parallel and other perpendicular to the horizontally polarized excitation beam. G-factor can also be determined following longtime tail matching technique [12]. If $\tau_{rot} < \tau_f$, it can be seen that the curves for $I_{\parallel}(t)$ and $I_{\perp}(t)$ should become identical. If in any experiment they are not, it can usually be assumed that this is due to a nonunitary G-factor. Hence normalizing the two decay curves on the tail of the decay eliminates the G-factor in the anisotropy measurement.

2.1.3. Estimation of microviscosity from Stokes-Einstein-Debye equation: The interfacial microviscosity, η_m as experienced by probe molecule in the biological/biomimicking systems like protein cavities, reverse micelle/micelle, can be estimated from the time-resolved fluorescence anisotropy using the modified Stokes-Einstein-Debye equation (SED) [14, 15],

$$\tau_r = \frac{\eta_m V_h}{k_B T} \quad (2.37)$$

where k_B is the Boltzmann constant, T is the absolute temperature. Hydrodynamic volume of the probe (V_h) can be calculated as:

$$V_h = V_m f C \quad (2.38)$$

where f is the shape factor ($f = 1$ for a spherical probe) and C represents solute-solvent coupling constant ($C = 1$ for “stick” condition and $C < 1$ for “slip” condition) and V_m is the molecular volume of the probe [16]. In case of $f = C = 1$, equation (2.37) reduces to the original simple SED equation,

$$\tau_r = \frac{\eta_m V_m}{k_B T} \quad (2.39)$$

For probe molecules with prolate ellipsoid shape, the value of f is calculated using the equation [14, 15],

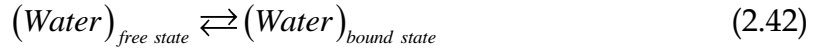
$$f = \frac{2}{3} \frac{1 - p^4}{[(2 - p^2)p^2(1 - p^2)^{-1/2} \ln \frac{1 + (1 - p^2)^{1/2}}{p}] - p^2} \quad (2.40)$$

where p is the axial ratio (ratio of minor axis to major axis) of the prolate ellipsoid. The energy barrier, E_η for the viscous flow is estimated according to the relation [17],

$$\eta_m = \eta_0 \exp\left(\frac{E_\eta}{RT}\right) \quad (2.41)$$

2.1.4. Arrhenius theory of activation energy: The dynamics of solvation at a biomolecular interface can be exploited to give information about the energetics of the participating water molecules [3]. Water present at the surface of biomolecules

or biomimetic can broadly be distinguished as bound type (water hydrogen bonded to the interface, BW) and free type water (FW). In the water layer around the surface, the interaction with water involves hydrogen bonding to the polar and charged groups of the surface. When strongly bonded to the biomacromolecules or biomimicking surfaces, the water molecules cannot contribute to solvation dynamics because they can neither rotate nor translate. However, hydrogen bonding is transient and there exists a dynamic equilibrium between the free and the bound water molecules. The potential of the interaction can be represented by a double-well structure to symbolize the processes of bond breaking and bond forming. In general, the bonded water molecules become free by translational and rotational motions. The equilibrium between bound and free water can be written as [17],



Using the dynamic exchange model, an expression for this equilibrium can be derived. In a coupled diffusion-reaction equation the rate constant k_{\pm} can be written as,

$$k_{\pm} = 0.5[-B \pm (B^2 - 4D_R k_{bf})^{1/2}] \quad (2.43)$$

where $B = 2D_R + k_{bf} + k_{fb}$ and D_R is the rotational diffusion constant, k_{bf} is the rate constant of the bound to free transition and k_{fb} is that of the reverse process. Typically, the rate constant of free to bound reaction, is larger than that for the reverse process. It can be shown that, when the rates of interconversion between “bound” and “free” water molecules are small as compared to $2D_R$, then,

$$\tau_{slow} \approx k_{bf}^{-1} \quad (2.44)$$

and from the activated complex theory one can have,

$$k_{bf} = (k_B T / h) \exp(-\Delta G^0 / RT) \quad (2.45)$$

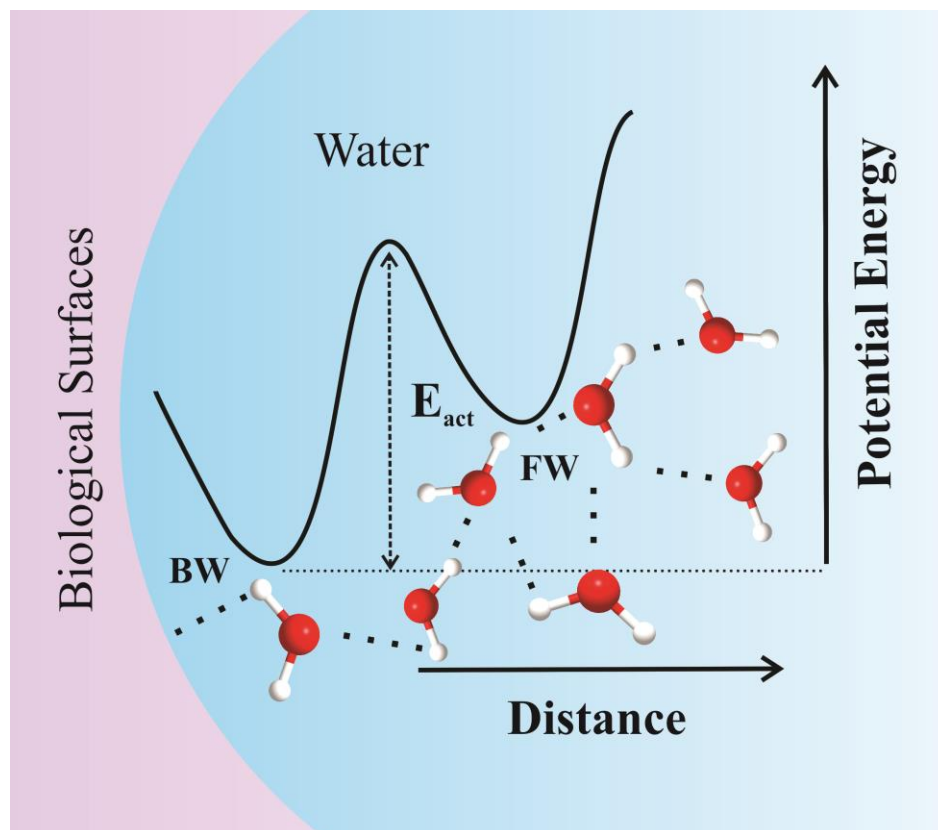


Figure 2.5. Schematic representation of different types of water molecules (BW and FW) present at various bimolecular interfaces and the corresponding activation energy barrier.

If the transition process (equation (2.42)) follows a typical Arrhenius type of energy barrier crossing model, one can write,

$$\tau_{slow}^{-1} \approx k_{bf} = A \exp(-E_{act}/RT) \quad (2.46)$$

where ' E_{act} ' is the activation energy for the transition process and ' A ' is the pre-exponential factor. A plot of $\ln(1/\tau_{slow})$ against $1/T$ produces a straight line and from the slope of the line E_{act} can be calculated. The temperature dependence of the solvation follows the Arrhenius equation and yields the activation energy needed for the conversion of bound and free forms [18].

2.1.5. Förster resonance energy transfer (FRET): FRET is an electrodynamic phenomenon involving the nonradiative transfer of the excited state energy from the donor dipole (D) to an acceptor dipole (A) in the ground state (Figure 2.6a). FRET has got wide applications in all fluorescence applications including medical

diagnostics, DNA analysis and optical imaging. Since FRET can measure the size of a protein molecule or the thickness of a membrane, it is also known as 'spectroscopic ruler' [19]. FRET is very often used to measure the distance between two sites on a macromolecule [20]. Basically, FRET is of two types: (i) homo-molecular FRET and (ii) hetero-molecular FRET. In the former case the same fluorophore acts both as energy donor and acceptor, while in the latter case two different molecules act as donor and acceptor.

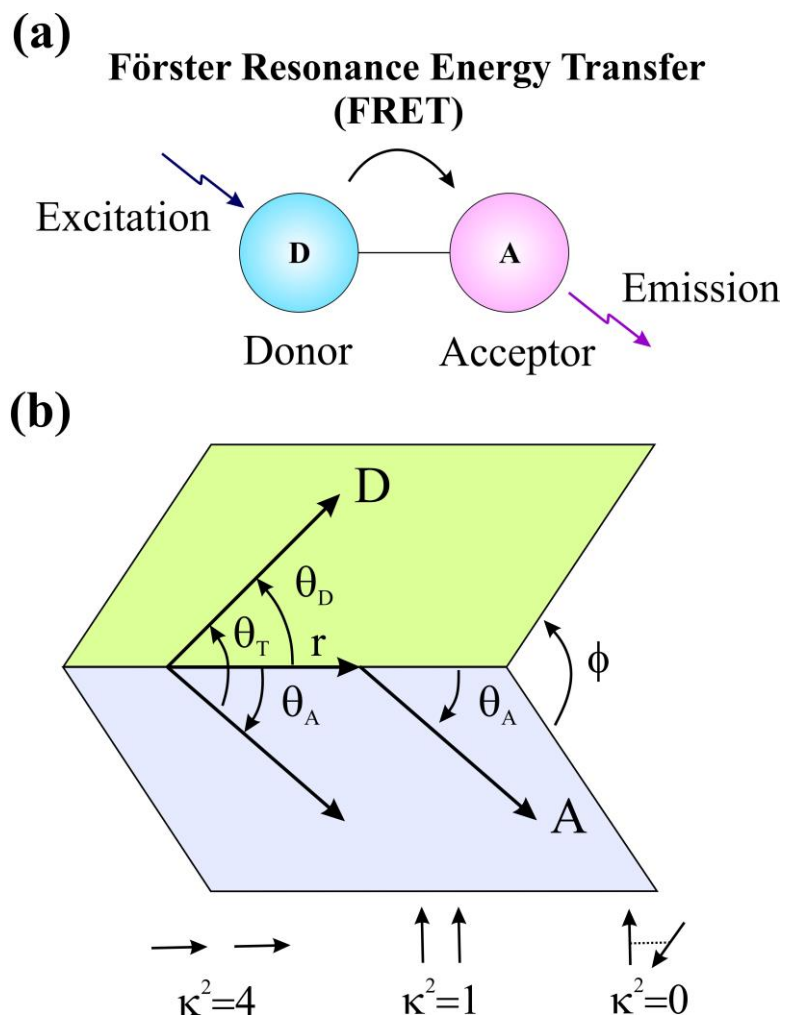


Figure 2.6. (a) Schematic illustration of the FRET process. (b) Dependence of the orientation factor κ^2 on the directions of the emission and absorption dipoles of the donor and acceptor, respectively.

Each donor-acceptor (D-A) pair participating in FRET is characterized by a distance known as Förster distance (R_0) i.e., the D-A separation at which energy transfer is 50% efficient. The R_0 value ranges from 20 to 60 Å. The rate of resonance energy transfer (k_T) from donor to an acceptor is given by [12],

$$k_T = \frac{1}{\tau_D} \left(\frac{R_0}{r} \right)^6 \quad (2.47)$$

where τ_D is the lifetime of the donor in the absence of acceptor and r is the donor to acceptor (D-A) distance. The rate of transfer of donor energy depends upon the extent of overlap of the emission spectrum of the donor with the absorption spectrum of the acceptor ($J(\lambda)$), the quantum yield of the donor (Q_D), the relative orientation of the donor and acceptor transition dipoles (κ^2) and the distance between the donor and acceptor molecules (r) (Figure 2.6b). In order to estimate FRET efficiency of the donor and hence to determine distances between donor-acceptor pairs, the methodology described below is followed [12]. R_0 is given by,

$$R_0 = 0.211 \left[\kappa^2 n^4 Q_D J(\lambda) \right]^{1/6} \text{ (in Å)} \quad (2.48)$$

where n is the refractive index of the medium, Q_D is the quantum yield of the donor and $J(\lambda)$ is the overlap integral. κ^2 is defined as,

$$\kappa^2 = (\cos \theta_T - 3 \cos \theta_D \cos \theta_A)^2 = (\sin \theta_D \sin \theta_A \cos \varphi - 2 \cos \theta_D \cos \theta_A)^2 \quad (2.49)$$

where θ_T is the angle between the emission transition dipole of the donor and the absorption transition dipole of the acceptor, θ_D and θ_A are the angles between these dipoles and the vector joining the donor and acceptor and φ is angle between the planes of the donor and acceptor (Figure 2.6b). κ^2 value can vary from 0 to 4. For collinear and parallel transition dipoles, $\kappa^2 = 4$; for parallel dipoles, $\kappa^2 = 1$; and for perpendicularly oriented dipoles, $\kappa^2 = 0$. For donor and acceptors that randomize by rotational diffusion prior to energy transfer, the magnitude of κ^2 is assumed to be 2/3. However, in systems where there is a definite site of attachment of the donor and acceptor molecules, to get physically relevant results, the value of κ^2 has to be estimated from the angle between the donor emission and

acceptor absorption dipoles [21]. $J(\lambda)$, the overlap integral, which expresses the degree of spectral overlap between the donor emission and the acceptor absorption, is given by,

$$J(\lambda) = \frac{\int_0^{\infty} F_D(\lambda) \varepsilon_A(\lambda) \lambda^4 d\lambda}{\int_0^{\infty} F_D(\lambda) d\lambda} \quad (2.50)$$

where $F_D(\lambda)$ is the fluorescence intensity of the donor in the wavelength range of λ to $\lambda+d\lambda$ and is dimensionless. $\varepsilon_A(\lambda)$ is the extinction coefficient (in $M^{-1}cm^{-1}$) of the acceptor at λ . If λ is in nm, then $J(\lambda)$ is in units of $M^{-1}cm^{-1}nm^4$.

Once the value of R_0 is known, the efficiency of energy transfer can be calculated. The efficiency of energy transfer (E) is the fraction of photons absorbed by the donor which are transferred to the acceptor and is defined as,

$$E = \frac{k_T(r)}{\tau_D^{-1} + k_T(r)} \quad (2.51)$$

$$\text{Or, } E = \frac{R_0^6}{r^6 + R_0^6} \quad (2.52)$$

For D-A systems decaying with multiexponential lifetimes, E is calculated from the amplitude weighted lifetimes $\langle \tau \rangle = \sum_i \alpha_i \tau_i$ of the donor in absence (τ_D) and presence (τ_{DA}) of the acceptor as,

$$E = 1 - \frac{\tau_{DA}}{\tau_D} \quad (2.53)$$

The D-A distances can be measured using equations (2.52) and (2.53).

Distance distribution between donor and acceptor was estimated according to the procedure described in the literature [12, 22]. The observed fluorescence transients of the donor molecules in absence of acceptor were fitted using a

nonlinear least-squares fitting procedure (software SCIENTIST) to the following function,

$$I_D(t) = \int_0^t E(t') p(t' - t) dt' \quad (2.54)$$

which comprises the convolution of the instrument response function (IRF) ($E(t)$) with exponential ($p(t) = \sum_i \alpha_{Di} \exp(-t / \tau_{Di})$). The convolution of the distance distribution function $P(r)$ in the fluorescence transients of donor in presence of acceptor in the system under studies is estimated using the same software (SCIENTIST) in the following way.

The intensity decay of D-A pair, spaced at a distance r , is given by

$$I_{DA}(r, t) = \sum_i \alpha_{Di} \exp \left[-\frac{t}{\tau_{Di}} - \frac{t}{\tau_{Di}} \left(\frac{R_0}{r} \right)^6 \right] \quad (2.55)$$

and the intensity decay of the sample considering distance distribution probability function, $P(r)$ is given by,

$$I_{DA}(t) = \int_{r=0}^{\infty} P(r) I_{DA}(r, t) dr \quad (2.56)$$

where $P(r)$ consist of the folowing terms:

$$P(r) = \frac{1}{\sigma \sqrt{2\pi}} \exp \left[-\frac{1}{2} \left(\frac{\bar{r} - r}{\sigma} \right)^2 \right] \quad (2.57)$$

In this equation \bar{r} is the mean of the Gaussian with a standard deviation of σ . Usually distance distributions are described by the full width at half maxima (hw). This half width is given by $hw = 2.354\sigma$.

2.1.6. Circular dichroism (CD): CD is now a routine tool in many laboratories with applications to determine whether a chiral molecule has been synthesized or resolved into pure enantiomers and probing the structures of biomolecules, in particular determining the α -helical content of proteins [23, 24].

2.1.6.1. Theory: When a plane polarized light passes through an optically active substance, not only do the left (L) and right (R) circularly polarized light rays travel at different speeds, $c_L \neq c_R$, but these two rays are absorbed to a different extent, i.e. $A_L \neq A_R$. The difference in the absorbance of the left and right circularly polarized light, i.e., $\Delta A = A_L - A_R$, is defined as circular dichroism (CD). Circular dichroism spectroscopy follows Beer-Lambert law. If I_0 is the intensity of light incident on the cell, and I , that of emergent light, then absorbance is given by,

$$A = \log_{10} \left(\frac{I_0}{I} \right) = \varepsilon cl \quad (2.58)$$

i.e., A is proportional to concentration (c) of optically active substance and optical path length (l). If ' c ' is in moles litre⁻¹ and ' l ' is in cm, then ε is called the molar absorptivity or molar extinction coefficient. In an optically active medium, two absorbances, A_L and A_R are considered, where $A_L = \log_{10} (I_0/I_L)$ and $A_R = \log_{10} (I_0/I_R)$. At the time of incidence on the sample, intensity of left and right circularly polarized light are same, i.e. $I_0 = I_L = I_R$. Any micrograph passes periodically changing light through the medium, oscillating between left and right circular polarization, and the difference in absorbances are recorded directly.

$$\Delta A = A_L - A_R = \log_{10} \left(\frac{I_0}{I_L} \right) - \log_{10} \left(\frac{I_0}{I_R} \right) = \log_{10} \left(\frac{I_R}{I_L} \right) \quad (2.59)$$

$$\Delta A = (\Delta \varepsilon) cl \quad (2.60)$$

As seen from equation (2.59), I_0 does not appear in this final equation, so there is no need for a reference beam. The instruments are, therefore, of single beam type.

After passing through an optically active substance, light is changed in two aspects. The maximal amplitude of intensity is no longer confined to a plane; instead it traces out an ellipse. Ellipticity is defined as the arctangent of the ratio of minor axis to the major axis of the ellipse (Figure 2.7). The orientation of ellipse is another aspect. The major axis of the ellipse no longer remains parallel to the

polarization of the incident light. Thus, after passing through an optically active substance, neither do the absorbance nor do the radii of the emergent left and right circularly polarized light remains same. Hence, CD is equivalent to ellipticity.

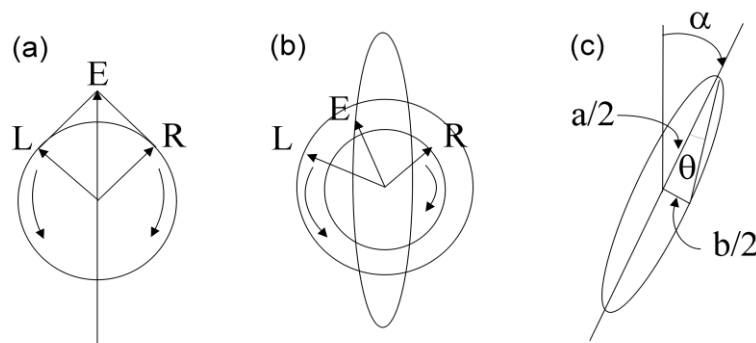


Figure 2.7. (a) Left (L) and right (R) circularly polarized light component having same intensities and phases lying in one plane and oscillating with same magnitude, (b) R component being less intense (more absorbed) than L component leading to elliptically polarized light and (c) θ , ellipticity is the angle made by semi-major and semi-minor axes of the ellipse. The major axis has rotated through angle α corresponding to optical rotation.

Most of the CD spectropolarimeters, although they measure differential absorption, produce a CD spectrum in units of ellipticity (θ) expressed in millidegrees versus λ , rather than ΔA versus λ . The relation between ellipticity and CD is given by,

$$\theta = \frac{2.303 \times 180 \times (A_L - A_R)}{4\pi} \text{ (in degrees)} \quad (2.61)$$

To compare the results from different samples, optical activity is computed on a molar or residue basis. Molar ellipticity, $[\theta]$ is defined as,

$$[\theta] = \frac{\theta}{cl} \quad (2.62)$$

where (θ) is in degrees, ' c ' is in moles per litre and ' l ' is in cm. The unit of molar ellipticity is $\text{deg.M}^{-1}.\text{cm}^{-1}$. Sometimes, CD is reported as $\Delta\epsilon = \Delta\epsilon_L - \Delta\epsilon_R$. From Beer-Lambert law and molar ellipticity relation it can be shown that,

$$[\theta] = 3300.\Delta\epsilon \quad (2.63)$$

2.1.6.2. Experimental methods: In biophysical studies, CD is mostly used to determine the secondary structures of proteins and nucleic acids and the changes in secondary structures upon recognition by small molecules and other biomolecules. Through CD spectropolarimeter, we obtain CD spectrograph having a plot of optical rotation in millidegrees versus wavelength in nm. In order to obtain information about the secondary structures of proteins, the graph is fitted with non-linear least square fitting method using freely available software. The percentages of different secondary structures are calculated by matching the experimental data with that of reference standard. In proteins, the secondary structural content includes α -helix, β -sheet, β -turn and random coil while for DNA, CD is used to determine the structures of different A, B, Z and condensed forms of DNA. The CD spectrum of α -helix contains two negative peaks, one at 208 nm (π - π^* transition) and 222 nm (n - π^* transition). β -sheet has a negative band at 216 nm and a positive band of similar magnitude at 195 nm. β -turn has weak negative peak at 225 nm (n - π^* transition), a strong positive peak between 200 nm and 205 nm due to π - π^* transition and a strong negative band between 180 nm and 190 nm. Random coil or unordered conformation has a strong negative band below 200 nm; a positive band at 218 nm and in some cases has a very weak negative band at 235 nm. A positive band centered at 275 nm and a negative band at 240 nm with crossover at 258 nm characterizes B-DNA. Under high salt condition, the band at 275 nm collapse due to reduction in number of base pairs per turn. A-DNA has a positive band at 260 nm, a very weak band at 190 nm and fairly intense negative band at 210 nm. Z-form DNA has a negative and a positive band at 290 nm and 260 nm, which are mirror images of B-DNA spectrum. Condensed DNA has a negative peak between 250 nm and 260 nm and long stretching positive molar ellipticity above 300 nm, not observed for normal B-form DNA.

2.1.7. Twisted intramolecular charge transfer (TICT): While interpretation of solvent-dependent emission spectra appears simple, this is a very complex topic. The complexity is due to the variety of interactions that can result in spectral shifts. The theory for general solvent effects is often inadequate for explaining the detailed behavior of fluorophores in a variety of environments.

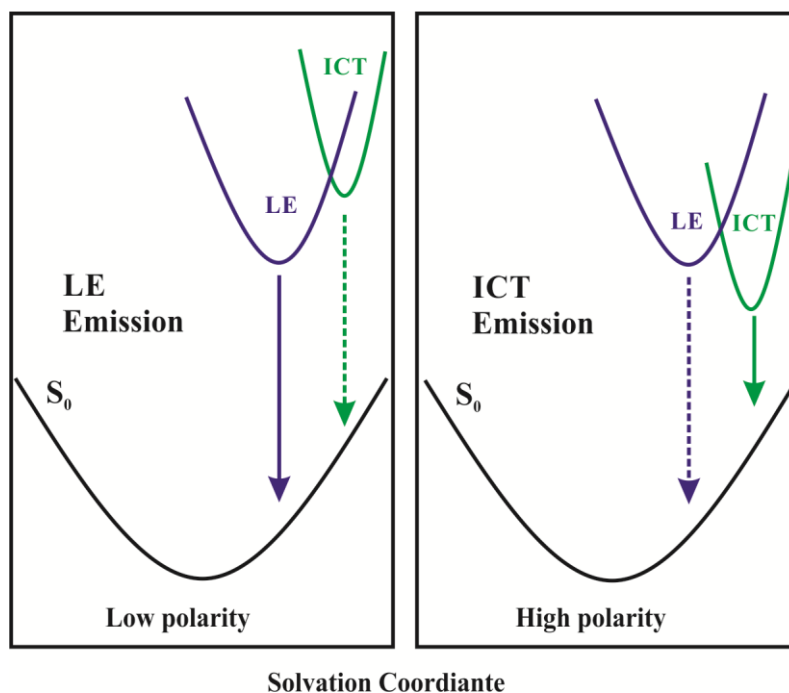


Figure 2.8. Effect of solvent polarity on the energies of locally excited (LE) and ICT states [9].

The Jablonski diagram for solvent effects should also reflect the possibility of specific solvent-fluorophore interactions that can lower the energy of the excited state. In addition to specific solvent-fluorophore interactions, many fluorophores can form an internal charge transfer (ICT) state, or a twisted internal charge transfer (TICT) state (Figure 2.8). For instance, suppose the fluorophore contains both an electron-donating and an electron-accepting group. Such groups could be amino and carbonyl groups, respectively, but numerous other groups are known. Following excitation there can be an increase in charge separation within the fluorophore. If the solvent is polar, then a species with charge separation (the

ICT state) may become the lowest energy state. In a nonpolar solvent the species without charge separation, the so-called locally excited (LE) state, may have the lowest energy. Hence, the role of solvent polarity is not only to lower the energy of the excited state due to general solvent effects, but also to govern which state has the lowest energy. In some cases, formation of the ICT state requires rotation of groups on the fluorophore to form the TICT state. Formation of ICT states is not contained within the theory of general solvent effects. Some probes display charge transfer in the excited state. In a highly viscous environment, the molecule cannot distort as needed for charge transfer, and the decay is radiative. In a less viscous environment, the molecule displays internal rotation and charge transfer, which results in radiation less decay.

2.1.8. Tachiya model: The excited state decay of the donor may be described by the following kinetic model assuming a competition of the energy transfer with unimolecular decay processes [25, 26]



where P_n^* stands for excited state of the donor with n number of adjacent acceptor molecules, while P_n stands for ground state donor molecules. k_0 is the total decay constant of donor in excited state in absence of the acceptor molecules. k_q is the rate constant for energy transfer for one donor molecule. In this model, it is assumed that the distribution of the number of acceptor molecules in proximity with one donor follows a Poisson distribution [26], namely,

$$p(n) = (m^n / n!) \exp(-m) \quad (2.66)$$

where m is the mean number of acceptor molecules in close proximity to one donor molecule and

$$m = k_+ [A] / k_- \quad (2.67)$$

where k_+ is the rate constant for attachment of a acceptor to a donor molecule, while k_- is the rate constant for detachment of a acceptor from the donor. $[A]$ stands for the concentration of acceptor molecules in the aqueous phase. Based upon the above model, the equation for the total concentration $P^*(t)$ of excited state donor at time t is given by

$$P^*(t) = P^*(0) \exp\left[-\left(k_0 + \frac{k_0 k_+ [A]}{k_- + k_q}\right)t - \frac{k_q^2 k_+ [A]}{k_- (k_- + k_q)^2} \{1 - \exp[-(k_- + k_q)t]\}\right] \quad (2.68)$$

If ' k_- ' is much smaller than k_q , equation (2.68) reduces to:

$$P^*(t) = P^*(0) \exp\{-k_0 t - m[1 - \exp(-k_q t)]\} \quad (2.69)$$

2.1.9. Quantum yield calculation: Quantum yield of the dye Hoechst 33258 (H258) bound to DNA was calculated according to the following equation using ethanol as a reference standard,

$$Q = Q_R \left(\frac{I}{I_R} \right) \left(\frac{OD_R}{OD} \right) \left(\frac{n^2}{n_R^2} \right) \quad (2.70)$$

where Q denotes quantum yield, OD is optical density at the excitation wavelength of 375 nm, I is the integrated fluorescence intensity and n is the refractive indices of Hoechst in respective solutions. Considering the Q_R of H258 in ethanol to be 0.50 [27], the Q of H258 bound to DNA was measured [28].

2.1.10. Microfluidics theory: The flow of a fluid through a microfluidic channel can be characterized by the Reynolds number, defined as,

$$R_e = \frac{LV_{avg}\rho}{\mu} \quad (2.71)$$

where L is the most relevant length scale, μ is the viscosity, ρ is the fluid density, and V_{avg} is the average velocity of the flow. For microchannels, L is equal to $4A/P$ where A is the cross sectional area of the channel and P is the wetted perimeter of the channel. Due to the small dimensions of microchannels, the R_e is usually much less than 100. In this Reynolds number regime, flow is completely laminar and no

turbulence occurs. The transition to turbulent flow generally occurs in the range of Reynolds number 2000. Laminar flow provides a means by which molecules can be transported in a relatively predictable manner through microchannels.

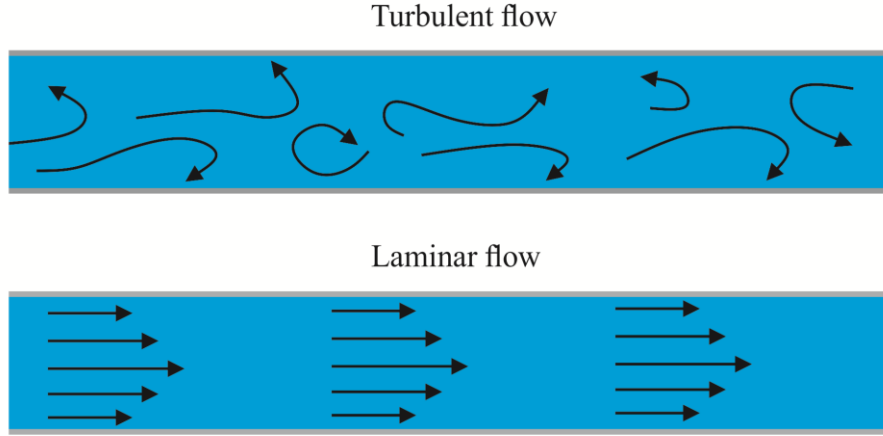


Figure 2.9. Graphical representation of turbulent and laminar flow within a microchannel.

Due to laminar flow in the microchannel, the transport of the mass of the subjected species within the microchannel follows the diffusion law. Figure 2.10 depicts the molecular diffusion of the species under study in the microchannel. The diffusion coefficient is estimated according to the procedure described by in the literature [29]. Considering the two-dimensional diffusion law, Einstein's equation of Brownian motion states that,

$$\tau = \frac{d^2}{2D} \quad (2.72)$$

where, d is the root mean square distance traversed by a molecule during the time interval for a given diffusion coefficient D .

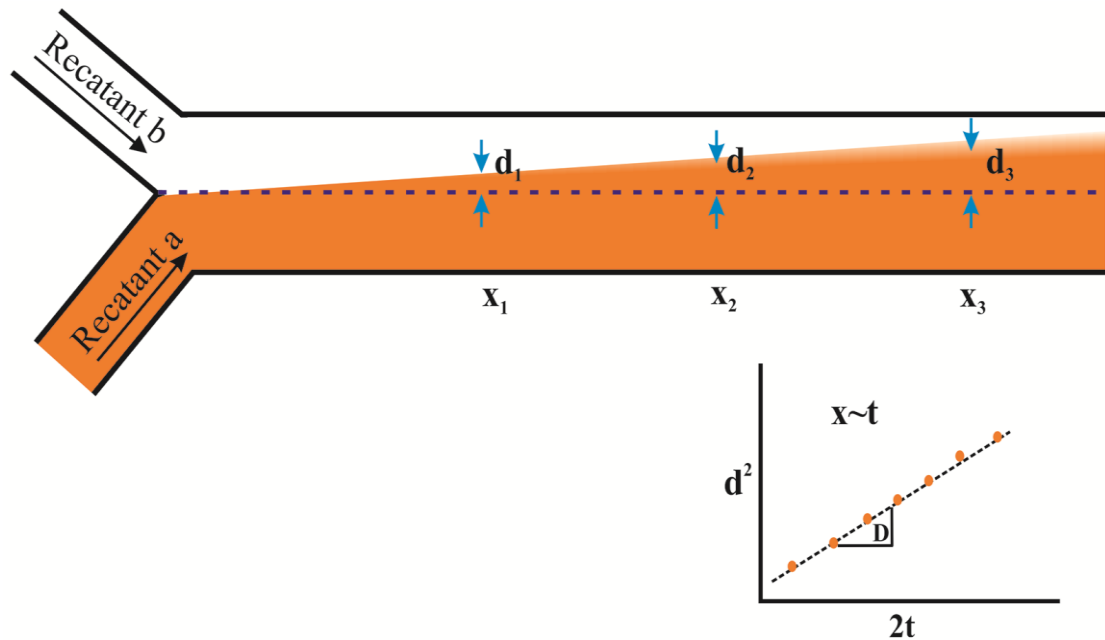
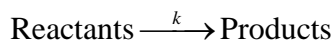


Figure 2.10. Measurement of the diffusion of the subjected species by monitoring the spreading width at different time interval is graphically represented.

The kinetics of molecular recognition/interaction was analyzed by measuring the fluorescence intensity of fluoroprobe along the microchannel. For a single step first order reaction, reactants will produce products as follows:



The rate equation can be written as [30],

$$x = a(1 - e^{-kt}) \quad (2.73)$$

where, 'x' corresponds to the product concentration at time t and k is the first-order rate constant. Considering a reaction having an intermediate step, i.e. $A \xrightarrow{k_1} I \xrightarrow{k_2} P$, the product concentration at time, t would be [30],

$$x = a \left(1 + \frac{k_1 e^{-k_2 t} - k_2 e^{-k_1 t}}{k_2 - k_1} \right) \quad (2.74)$$

Where, 'a' denotes the initial concentration at time $t=0$ and k_1 , k_2 are the respective rate constants. The precision of the measurement of the kinetics parameter will depend on the uniformity and accuracy of the flow velocity and the signal-to-noise ratio in the fluorescence measurement.

2.2. Systems:

2.2.1. Organized assemblies (biomimetics): Amphiphilic molecules like surfactant aggregates to form macromolecular assemblies, like micelles and reverse micelles, which very often resemble the structural properties of biomolecules. In the following section, we will discuss about these entities.

2.2.1.1. Micelles: Micelles are spherical or nearly spherical aggregates of amphiphilic surfactant molecules formed in aqueous solution above a concentration known as critical micellar concentration (CMC). Micelles are formed above a critical temperature called “Kraft point” which is different for different surfactants. Micellar aggregates have diameter varying within 10 nm and the aggregation number, i.e., the number of surfactant molecules per micelle, ranges from 20 to 200. Israelachvili et al. [31] have proposed that surfactant molecular packing considerations are determinant in the formation of large surfactant aggregates. In particular, it is considered that the surfactant packing parameter θ ($\theta = \nu/\sigma l$, where ν is the surfactant molecular volume, σ is the area per polar head, and l is the length of hydrophobic part) gives a good idea of the shape of aggregates which will form spontaneously [31]. It is considered that normal or direct rod-like micelles are formed when $2 < \theta < 3$ [32]. Micelles can be both neutral (triton X-100) and ionic (sodium dodecyl sulfate, SDS (anionic) and cetyl trimethyl ammonium bromide, CTAB (cationic)). The structure of a typical micelle is schematically shown in Figure 2.11. The core of a micelle is essentially “dry” and consists of the hydrocarbon chains with the polar and charged head groups projecting outward toward the bulk water. The stern layer, surrounding the core, comprises of the ionic or polar head groups, bound counter ions and water molecules. Between the stern layer and the bulk water there is a diffused Guoy-Chapman (GC) layer, which contains the free counter ions and water molecules.

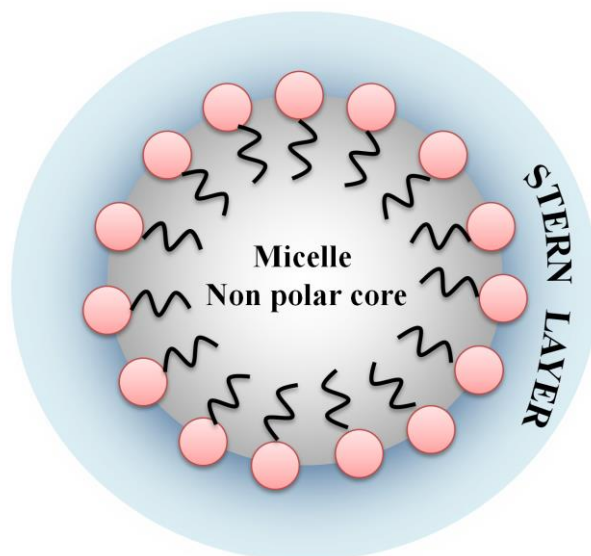


Figure 2.11. The schematic representation of the structure of a micelle.

In non-ionic polyoxyethylated surfactants e.g. triton X-100 (TX-100), the hydrocarbon core is surrounded by a palisade layer, which consists of the polyoxyethylene groups hydrogen-bonded to water molecules [33]. Small angle X-ray and neutron scattering have provided detailed information on the structure of the CTAB micelles [34, 35]. According to these studies, CMC and aggregation number of CTAB micelle are 0.8 mM and 52 respectively and the thickness of the stern layer is 6-9 Å. The overall radius of CTAB micelle is about 50 Å. For TX-100 micelle, the CMC, thickness of the palisade layer and overall radius of the hydrophobic core are reported to be 0.1 mM, 51 Å and 25-27 Å, respectively and that of SDS micelles are 8.6 mM [36], 33 Å [37] and 5 Å, respectively [38].

2.2.1.2. Reverse micelle: Reverse micelles (RMs) or water-in-oil microemulsions (Figure 2.12) are nanopools of polar solvent protected by a monolayer of surfactant molecules at the periphery with polar head groups pointing inward into the polar solvent, and the hydrocarbon tails directed toward the non-polar organic solvents [39, 40]. RMs with water nanopools resemble the water pockets found in various bio-aggregates such as proteins, membranes, and mitochondria. Thus, these systems are very often considered as templates for the synthesis of

nanoparticles and as excellent biomimetic for exploration of biological membranes and biologically confined water molecules [41]. Aqueous RMs are generally characterized by the degree of hydration (w_0), which is the ratio of molar concentration of water to that of surfactant, where the radius of the water pool (r in Å) is empirically defined as, $r = 2 \times w_0$ [42]. Shapes and sizes of the surfactant aggregates depend strongly on the type and concentration of the surfactant, and on the nature of counterion and external solvent. In principle, reverse micelles can be formed in the presence and in the absence of solubilized water. However, it has generally been proposed that if the medium is completely water-free, there is not a well-defined CMC (critical micelle concentration), and the aggregates formed are very small and polydisperse, indicating minimum cooperativity in the surfactant association.

This has been particularly established for surfactant bis (2-ethylhexyl) sulfosuccinate sodium salt (AOT) in several organic solvents. RMs with w_0 values less than 20 are stable and mono disperse over a wide range of temperatures. The AOT-alkane-water system is interesting as the solution is homogeneous and optically transparent over a wide range of temperature, pressure, and pH. The AOT-RMs can compartmentalize a large amount of water in its central core, and the nanoscale aggregation process is fairly well characterized with respect to size and shape at various water contents. The CMC of AOT in hydrocarbon solvent is about 0.1 mM. In liquid alkanes, AOT-RMs ($w_0 = 0$) are completely associated and each micelle contains 23 monomers. The structures of these RMs are slightly asymmetric and are of round cylindrical nature. Spherical RMs are generally formed by surfactants with high values of the packing parameter, $\theta > 3$. AOT RMs can dissolve large amounts of water, being able to reach w_0 values as large as 40-60, depending on the surrounding non-polar organic medium and temperature [43]. At low w_0 values, the systems are usually referred to as RMs, whereas the term water-in-oil microemulsion is frequently used for higher w_0 values. Fluorescence spectroscopy has been extensively used to study the AOT-RMs

system. Fluorescent probes have been used to determine the viscosity, binding site, rigidity and proximity within the water pool. These studies have shown that water inside the RMs is generally of two types: i) interfacial (bound) and ii) core (free) water. One of the studies [44] has shown the existence of third type of water (trapped) molecules present between the polar head groups of the individual surfactant molecules. Thus, the interior of RMs is extremely heterogeneous. Dielectric relaxation studies [45] indicate the presence of 7 ns component for bound water in RM, very similar to those of water molecules in the close vicinity of biological macromolecules (biological water). In contrast to AOT which does not require any cosurfactant to form RMS, cationic surfactants do not form RMs in the absence of cosurfactants. Several non-ionic or neutral surfactants (TX-100) have been reported to form RMs in pure and mixed hydrocarbon solvents [46].

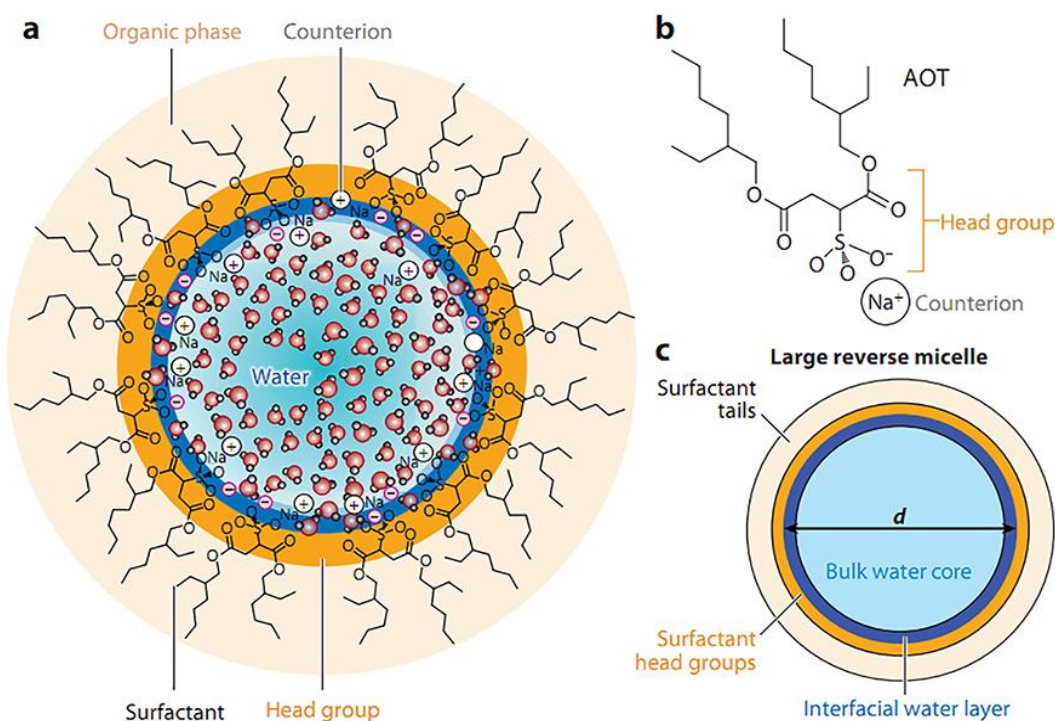


Figure 2.12. (a) Schematic depiction of a potential structure of a reverse micelle. Water molecules reside in the interior, sometimes interacting with head groups and counterions. Surfactant tails reside in contact with the continuous, nonpolar, organic supporting phase. (b) Chemical structure of Aerosol OT (AOT; sodium bis(2-ethylhexyl) sulfosuccinate) (c) Schematic of a large reverse micelle showing important features of the structure.

2.2.2. Proteins: Two types of proteins; human serum albumin (HSA) also known as endogenous serum albumin (ESA) and λ -repressor have been used in our study.

2.2.2.1. Human serum albumin: Human serum albumin (HSA) is a multi-domain protein (Figure 2.13) forming the major soluble protein constituent (60 % of the blood serum) of the blood circulatory system [47]. HSA (molecular weight 66,479 Da) is a heart-shaped tridomain protein with each domain comprising of two identical subdomains-A and B with each domain depicting specific structural and functional characteristics [48]. HSA having 585 amino acid residues assumes solid equilateral triangular shape with sides ~ 80 Å and depth ~ 30 Å [49]. Its amino acid sequence comprises of 17 disulfide bridges distributed over all domains, one free thiol (Cys 34) in domain-I and a tryptophan residue (Trp 214) in domain-IIA. About 67% of HSA is α -helical while the rest of the structure being turns and extended polypeptides [49]. Each domain contains 10 principle helices (h1-h10). Subdomains-A and B share a common motif that includes h1, h2, h3 and h4 for subdomain-A, and h7, h8, h9, h10 for subdomain-B. The non-existence of disulfide linkage connecting h1 and h3 in subdomain-IA is an exception. HSA is engaged with various physiological functions involving maintenance of osmotic blood pressure, transportation of a wide variety of ligands in and out of the physiological system. The protein binds various kinds of ligands [50] including photosensitizing drugs [51] and the principal binding regions are located in subdomains-IIA and IIIA of which IIIA binding cavity is the most active one [49] and binds digitoxin and ibuprofen. It is known that HSA undergoes reversible conformational transformation with change in pH of the protein solution [52, 53], which is very essential for picking up and releasing drugs at sites of differing pH inside physiological system. At normal pH = 7, HSA assumes the normal form (N) which abruptly changes to fast migrating form (F) at pH values less than 4.3, as this form moves “fast” upon gel electrophoresis [47]. Upon further reduction in

pH to less than 2.7, the F-form changes to the fully extended form (E). Above pH=8, the N-form changes to basic form (B) and above pH=10, the structure changes to another aged form (A). Serum albumin undergoes an ageing process when stored at low ionic strength at alkaline pH. The aging process is catalyzed by the free sulfhydryl group involving sulfhydryl-disulfide interchange that results in the conservation of the sulfhydryl at its origin position. This A-form is stable and does not undergo N-F transition [54, 55].

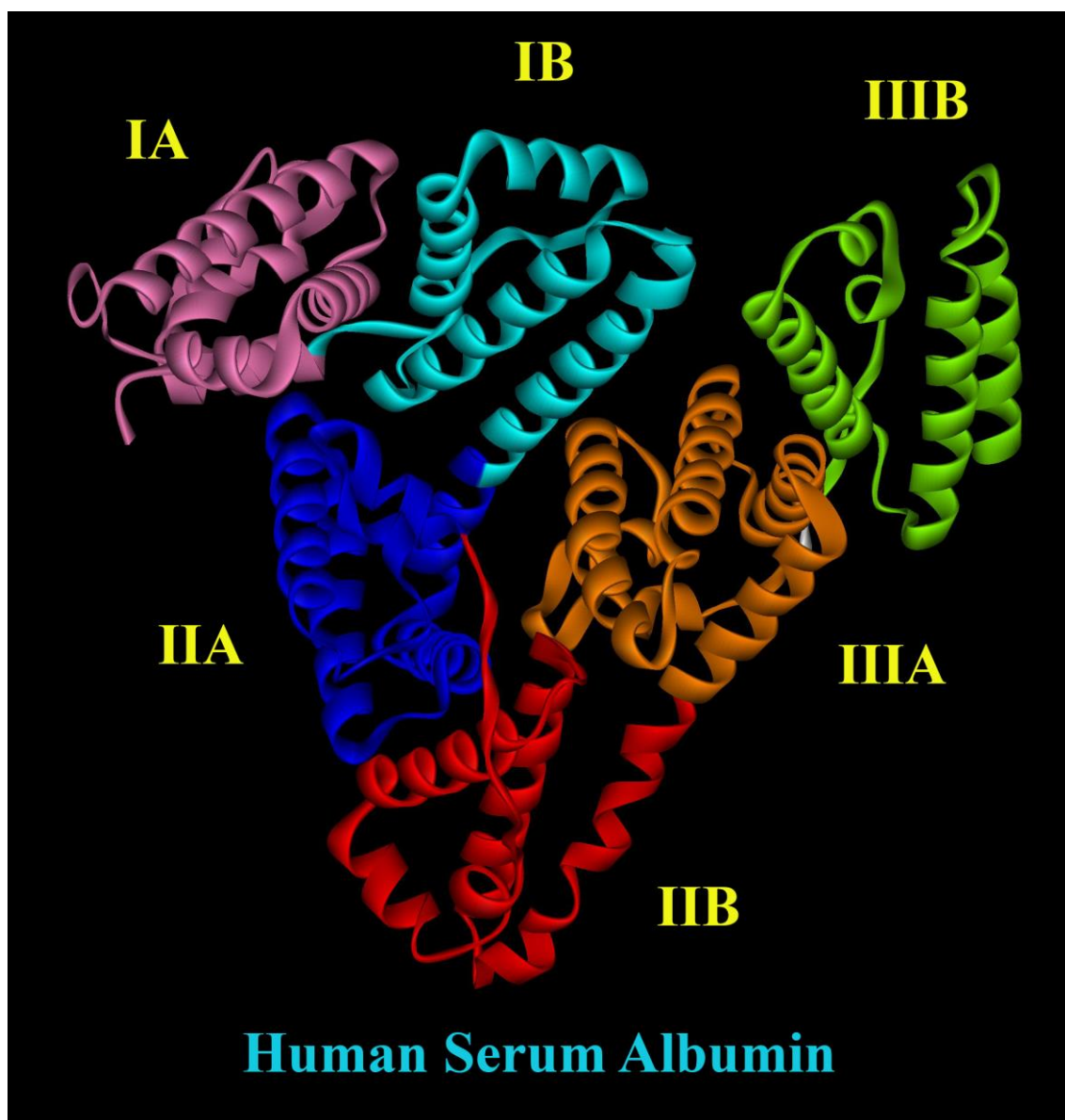


Figure 2.13. X-ray crystallographic structure (PDB code: 1N5U) of HSA depicting the different domains.

2.2.2.2. λ -Repressor: The λ -repressor has been a useful model system for studying the role of specific protein-DNA and protein-protein interaction in maintaining complex gene regulatory circuits. The λ -repressor is a single polypeptide chain of 236 amino acids. λ -repressor is a two domain viral protein (Figure 2.14) that binds to operator DNA, induces lysogenic life cycle of an infected bacteria, and exists in dimeric and higher order oligomeric form depending on concentration. Cleavage of λ -repressor with papain revealed that it has two functional domains [56]. The N-terminal domain containing residues 1-92 is responsible for DNA binding and activation of RNA polymerase bound at P_{RM} . The region from residue 92 to 131, the protease sensitive part, is less tightly folded and flexible, and is usually referred to as the hinge region. The fragment, containing residues 132 to 236 is the C-terminal domain, which is responsible for protein-protein contact. Although isolated N-terminal domains can form dimers, they do so only weakly and hence they bind the cognate operator sequence with a much weaker affinity than the intact repressor molecule.

Mark Ptashne and coworkers have established the λ genetic switch, which is governed by λ -repressor and cro-repressor. The switching system consists of three contiguous 17 base pair sequences known as the right operator sites, O_{R1} , O_{R2} and O_{R3} , and two proteins λ -repressor and cro-repressor. This collection of operator sites known as right operator or O_R , also contains two promoters P_{RM} and P_R . The structural gene of λ -repressor (*cI*) is under the control of P_{RM} and the structural gene of *cro* is under the control of the promoter P_R . λ -repressor binds to the three operator sites, cooperatively, in the order of decreasing affinity $O_{R1} > O_{R2} > O_{R3}$ [57]. In the lysogenic state, two λ -repressor dimers occupy O_{R1} and O_{R2} and activate the promoter P_{RM} repressing the promoter P_R . Thus, it shuts off *cro* synthesis and activates λ -repressor synthesis.

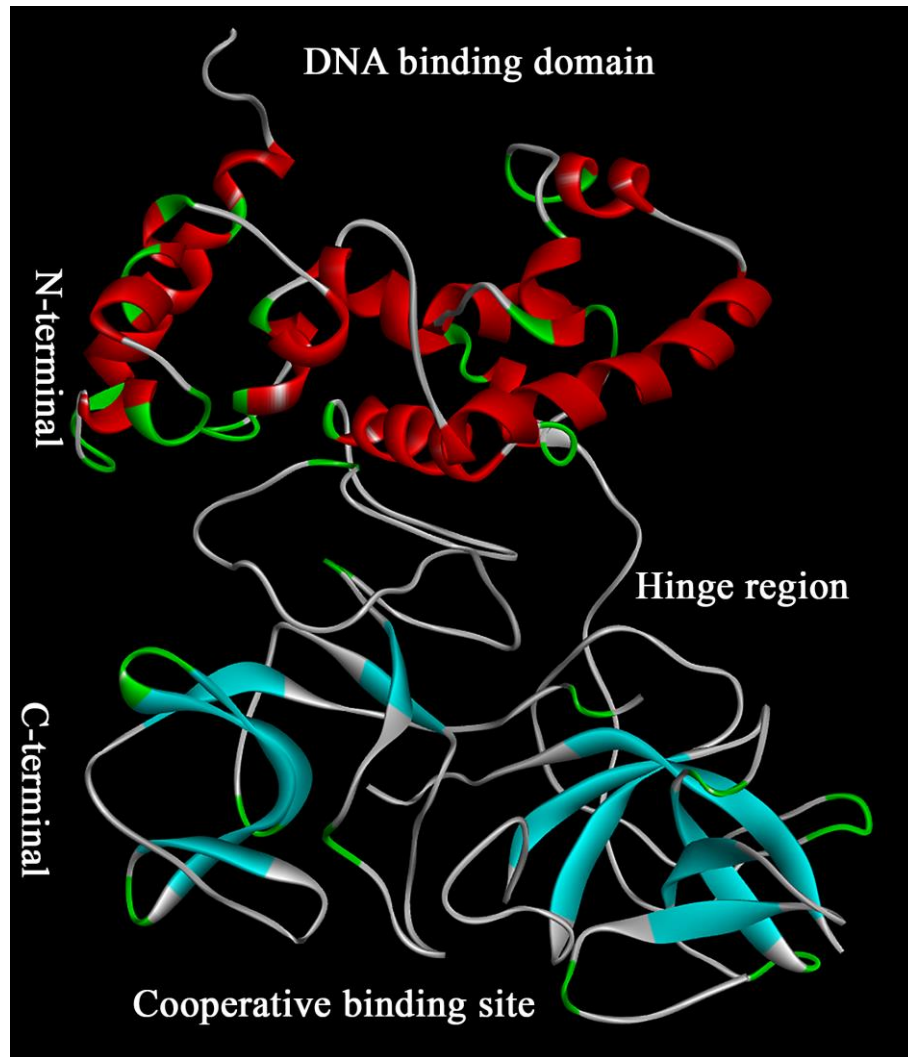


Figure 2.14. X-ray crystallographic structure of λ -repressor (PDB code: 3BDN), depicting the different domains.

A stable lysogenic state is maintained by multimeric complexes of λ -repressor cooperatively bound to a pair of operators, O_L (left operator sites) and O_R (right operator sites), on the bacteriophage λ genome involving a long range looping. It is generally believed that during lysogeny, an octameric complex is initially formed in which four dimers of λ -repressor are bound to O_{R1} - O_{R2} and O_{L1} - O_{L2} with concomitant looping of the intervening DNA. The proteolytic cleavage that is activated by UV radiation separates the λ -repressor C-terminal domain from the N-terminal domain thus resulting in a decreased affinity of repressor towards O_{R1} which initiates the switch from lysogeny to lysis cycle [58, 59]. A schematic

representation of the control exerted by the λ -repressor on the right operator region of bacteriophage λ is shown in Figure 2.15.

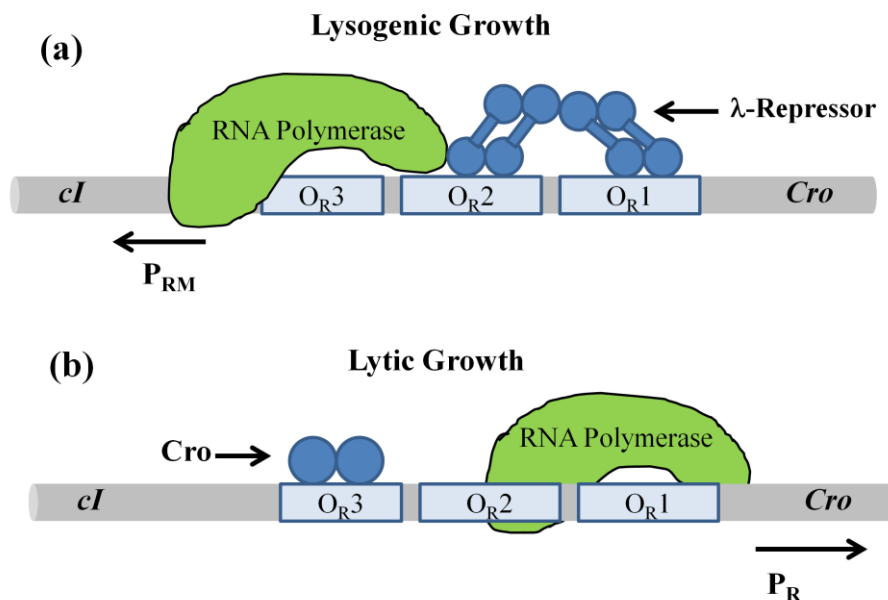


Figure 2.15. The λ phage genetic switch depicting (a) Lysogenic cycle and (b) Lytic cycle.

2.2.3. Deoxyribonucleic acid: Deoxyribonucleic acids (DNA) are polynucleotide with each nucleotide comprising of deoxyribose sugar, purine and pyrimidine bases and phosphate groups. The main bases whose intermolecular hydrogen bonding holds the DNA strands together are adenine, guanine, thymine and cytosine. DNA serves as carrier of genetic information [60, 61]. The classic example of how biological function follows from biomolecular structure comes from the elucidation of double helical structure of DNA by Watson and Crick [62]. There are generally three forms of DNA-A, B and Z-form. Natural DNA, however, exists in B-form. Natural DNA is about meter long and comprises of hundreds of base pairs. The distance between two base pairs in B-DNA is 3.4 Å [63]. In about 4 M NaCl, B-form assumes Z-form. DNA structures consist of major and minor grooves and intercalation spaces through which DNA interacts with ligands. There are two modes of interaction between DNA and ligands: (i) intercalation,

where the planar polycyclic hetero-aromatic ligands sit in between the base pairs of DNA and interact through π - π interaction [64, 65], and (ii) groove binding, where the ligands bind in the major and minor grooves of DNA [66]. The water molecules at the surface of DNA are critical for the molecular recognition and maintaining the structure. The DNA codes for proteins and that code is copied into messenger RNA during a process called transcription. Transcription is the first step leading to gene expression and an intricate regulation of this step is critical for the complex functioning of a living cell. The process of transcription is carried out by an enzyme called the RNA polymerase and is tightly regulated by a class of proteins called the transcription factors. Transcription factors are proteins that bind specifically to target DNA sequences upstream or downstream of a particular gene and thereby influence its expression pattern. The basic principle of transcription regulation was established in 1960, primarily by the pioneering work of Francois Jacob and Jacques Monod. The fundamental units of gene regulation in prokaryotes are three types of DNA sequences that determine the level of gene expression under physiological conditions.

(a) Promoters: Originally defined as elements that determine the maximum potential level of gene expression. Promoters are recognized by RNA polymerase, and contain all the information necessary for accurate transcription initiation.

(b) Operators: These are sequences recognized by transcription factors which inhibit transcription that would otherwise occur from the promoters.

(c) Some positive control DNA elements are recognized by activator proteins that stimulate transcription from the promoter. The function of activators and repressors can be modulated by specific physiological conditions thereby regulating expression of the cognate genes.

We have used right operators DNA (O_{R1} and O_{R2}) of λ phage genome, in our studies. O_{R1} (5'CGTACCTCTGGCGGTGATAG3') and its complementary oligonucleotide, O_{R2} (5'TACAACACGCACGGTGTAT3') and its complementary

oligonucleotide were used in our experiments. The schematic of operator DNA is represented in Figure 2.16. We have also used Salmon sperm DNA for studying the DNA drug interaction.

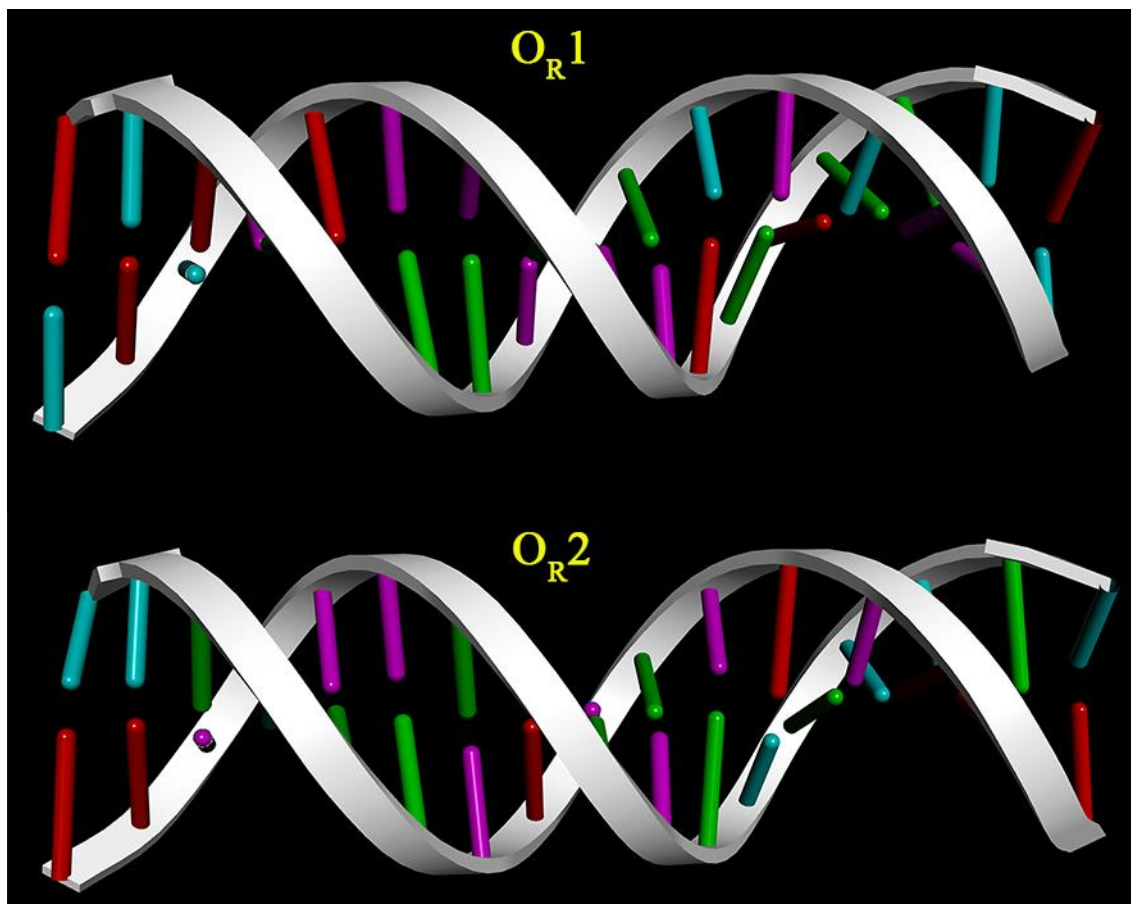


Figure 2.16. Schematic representation of operator DNA O_{R1} and O_{R2} (DNA structures were made by employing the WEBLAB VIEWERLITE program).

2.2.4. Molecular probes: In this section we will discuss about the different probe molecules that have been used in the course of study.

2.2.4.1. *p*-Benzoquinone (BQ): BQ (Figure 2.17f) is a well-known probe for electron accepting and shuttling for any electron rich material/compound, which readily accepts electron and adapted to the resonance species hydroquinone [67]. Large doses could induce local irritation, clonic convulsions, decreased blood pressure and death due to paralysis of the medullary centres.

2.2.4.2. Tryptophan [(2S)-2-amino-3-(1H-indol-3-yl) propanoic acid]: Tryptophan (Figure 2.17c) is one of the 22 standard amino acids and an essential amino acid in the human diet. Only the L-stereoisomer of tryptophan is found in enzymes and proteins. However, the D-stereoisomer is occasionally found in naturally produced peptides. Tryptophan has large bulky aromatic side chain. Tryptophan is significantly more polar than other aromatic amino acids, because of the nitrogen of the tryptophan indole ring. Tryptophan is rare amino acid and has a single codon. It absorbs light at 280 nm. The molar extinction coefficient value of tryptophan in water is $5,579 \text{ M}^{-1} \text{ cm}^{-1}$ at 278 nm. The fluorescence emission peak of tryptophan dissolved in water is at $\sim 355 \text{ nm}$ and the quantum yield of this molecule is 0.14 [68].

2.2.4.3. [2'-(4-Hydroxyphenyl)-5-(4-methyl-1-piperazinyl)-2,5'-bi-1H benzimidazole trihydrochloride hydrate], Hoechst 33258 (H258): The commercially available probe H258 (Figure 2.17a) is widely used as fluorescent cytological stain of DNA. Since it has affinity for the double stranded DNA. H258 is soluble in water. In bulk water the absorption peak and emission peaks of H258 are at 366 and 500 nm [69], respectively and it is sensitive to the polarity of the medium. The significant solvchromic effect (solvation) in the absorption and emission spectra of H258 makes the dye an attractive solvation probe for microenvironments [70].

2.2.4.4. Ethidium bromide (EtBr): EtBr is a well-known fluorescent probe (Figure 2.17b) for DNA, which readily intercalates into the DNA double helix [71]. Compared to bulk water, the emission intensity and lifetime of EtBr increases significantly when EtBr intercalates into the double helix of DNA [72]. This remarkable fluorescence enhancement of EtBr is utilized to study the motion of DNA segments, and the interaction of DNA with surfactants and drug [73]. Absorption maxima of EtBr in aqueous solution are at 285 nm and 480 nm, after excitation EtBr emits orange light with wavelength maxima at 620 nm [74].

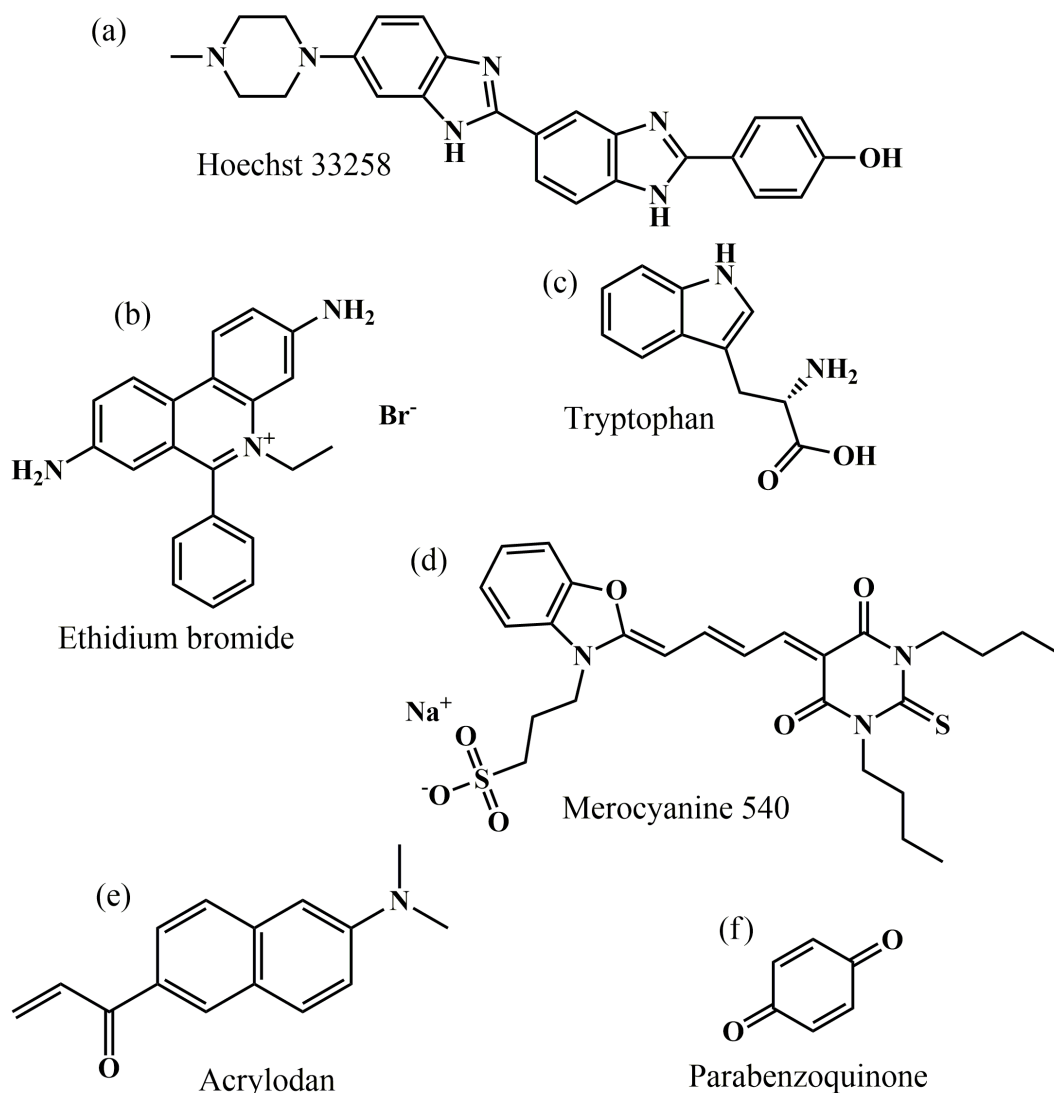


Figure 2.17. Molecular structure of (a) Hoechst 33258, (b) Ethidium bromide, (c) Tryptophan, (d) Merocyanine 540, (e) Acrylodan, (f) Parabenzoquinone.

2.2.4.5. Merocyanine 540 (MC540): MC540 is an anionic lipophilic (Figure 2.17d) polymethine dye and is commonly used as a sensitizer in chemotherapy [75]. It has the ability to readily bind to quantum dots, biomembranes, micelles, and proteins. In aqueous solutions, the fluorescence intensity of MC540 increases by an order of magnitude on binding to these biological systems. The fluorescence quantum yield and lifetime of MC540 in aqueous solutions are markedly lower than those in nonpolar solvents while its absorption maximum exhibits a blue shift in aqueous solution compared to that in a nonpolar solvent. In water an additional

absorption peak arises at 500 nm which is assigned to the MC540 dimer. It has been proposed that in aqueous solutions MC540 forms nonfluorescent dimers. When MC540 binds to micelles or vesicles, the nonfluorescent dimers break to form the fluorescent monomers, and this is responsible for the emission enhancement of MC540. The photophysical processes of MC540 in solutions and in organized media have recently been explored [76].

2.2.4.6. 6-Acryloyl-2-dimethylaminonaphthalene (acrylodan): The thiol reactive acrylodan (Figure 2.17e) generally reacts with thiols more slowly than iodoacetamides or maleimides, but does form very strong thioether bonds that remains stable under conditions required for complete amino acid analysis. The fluorescence emission peak and intensity of these adducts are particularly sensitive to conformational changes or ligand binding, making this dye one of the most useful thiol-reactive probe for protein structure studies. The environment-sensitive spectral shift of acrylodan conjugates may make this probe useful for distinguishing thiols that are located in membranes versus those exposed to aqueous solvation in cells.

2.2.5. Quantum dots (QDs): QDs are semiconductors whose excitons are confined in all three spatial dimensions. Amongst the various types of nanomaterials, QDs have been widely investigated and are quite understandable [77, 78]. They exhibit size-tunable band gaps and luminescence energies owing to the “quantum-size effect”. In order to understand that effect, first consider an electron excited from the valence band by the absorption of a quantum of light moves to the conduction band, leaving behind a hole in the valence band. Together, the bound state of the electron and the electron hole which are attracted

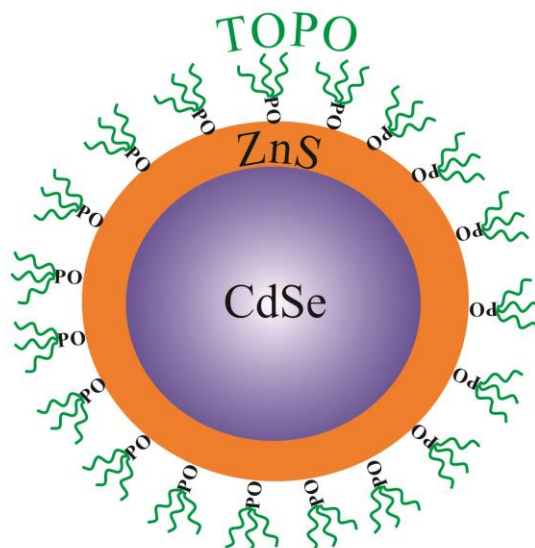


Figure 2.18. Schematic representation of a core-shell quantum dots. The core consist of CdSe and shell consists of ZnS. Trioctylphosphine oxide (TOPO) is used a capping ligand.

by coulombic force is called exciton. Taking a simple Bohr model picture of the exciton, the electron and hole orbit each other at a distance known as the Bohr radius, which varies depending on the material, ranging from a few to tens of nanometers. In a semiconductor crystallite whose diameter is smaller than the size of its excitons Bohr radius, the excitons are squeezed, leading to quantum confinement [77]. Compared with the organic fluorophores that were previously used for biological labelling, quantum dots are much brighter and do not photobleach. They also provide a readily accessible range of colours. As fluorophores, high quality QDs are extremely bright, with quantum yields (QYs) approaching unity. QDs have been used for a wide variety of applications, such as light emitting diodes, lasers and solar cells, staining and lighting up cells for visualization, photocatalysis etc. However, with regard to biological applications toxicity remains a complicated question. Additionally, cellular uptake of QDs is extremely complex, varying not only with size but with QD surface properties as well as cell type [79]. In our study we have mainly used Trioctylphosphine oxide (TOPO) capped CdSe/ZnS QDs dispersed in toluene solution.

References

1. B. Bagchi and R. Biswas, Polar and nonpolar solvation dynamics, ion diffusion and vibrational relaxation: Role of biphasic solvent response in chemical dynamics. *Adv. Chem. Phys.*, **109** (1999) 207.
2. R. Jimenez, G.R. Fleming, P.V. Kumar and M. Maroncelli, Femtosecond solvation dynamics of water. *Nature*, **369** (1994) 471.
3. S.K. Pal, J. Peon, B. Bagchi and A.H. Zewail, Biological water: Femtosecond dynamics of macromolecular hydration. *J. Phys. Chem. B*, **106** (2002) 12376.
4. B. Bagchi, Dynamics of solvation and charge transfer reactions in dipolar liquids. *Ann. Rev. Phys. Chem.*, **40** (1989) 115.
5. L. Onsager, Comments on "effects of phase density on the ionization process and electron localization in fluids" by J. Jortner and A. Gathon. *Can. J. Chem.*, **55** (1977) 1819.
6. R.M. Stratt and M. Maroncelli, Nonreactive dynamics in solution: The emerging molecular view of solvation dynamics and vibrational relaxation. *J. Phys. Chem.*, **100** (1996) 12981.
7. J.T. Hynes, Outer-sphere electron transfer reactions and frequency-dependent friction. *J. Phys. Chem.*, **90** (1986) 3701.
8. M.L. Horng, J.A. Gardecki, A. Papazyan and M. Maroncelli, Subpicosecond measurements of polar solvation dynamics: Coumarin 153 revisited. *J. Phys. Chem.*, **99** (1995) 17311.
9. J.R. Lakowicz, Principles of fluorescence spectroscopy. Second ed. 1999, New York: Kluwer Academic/Plenum Publishers.
10. N. Periasamy and A.S.R. Koti, Time resolved fluorescence spectroscopy: TRES and TRANES. *Proc. Indian Natn. Sci. Acad.*, **69A** (2003) 41.
11. A.S.R. Koti, M.M.G. Krishna and N. Periasamy, Time-resolved area-normalized emission spectroscopy (TRANES): A novel method for

- confirming emission from two excited states. *J. Phys. Chem. A*, **105** (2001) 1767.
12. J.R. Lakowicz, Principles of Fluorescence Spectroscopy. 2nd ed. 2006, New York: Kluwer Academic/Plenum.
 13. R.D. Spencer and G. Weber, Measurements of subnanosecond fluorescence lifetimes with a cross-correlation phase fluorometer. *Ann. N. Y. Acad. Sci*, **158** (1969) 361.
 14. L. A. Philips, S. P. Webb and J. H. Clark, High-pressure studies of rotational reorientation dynamics: The role of dielectric friction. *J. Chem. Phys.*, **83** (1985) 5810.
 15. B. Kalman, N. Clarke and L. B. A. Johansson, Dynamics of a new fluorescent probe, 2,5,8,11-tetra-tert-butylperylene in solution, cubic lyotropic liquid crystals, and model membranes. *J. Phys. Chem.*, **93** (1989) 4608.
 16. N. Ito, O. Kajimoto and K. Hara, Picosecond time-resolved fluorescence depolarization of p-terphenyl at high pressures. *Chem. Phys. Lett.*, **318** (2000) 118.
 17. R. Zana, Microviscosity of aqueous surfactant micelles: Effect of various parameters. *J. Phys. Chem. B*, **103** (1999) 9117.
 18. N. Nandi and B. Bagchi, Dielectric relaxation of biological water. *J. Phys. Chem. B*, **101** (1997) 10954.
 19. L. Stryer, Fluorescence energy transfer as a spectroscopic ruler. *Ann. Rev. Biochem.*, **47** (1978) 819.
 20. P.K. Verma and S.K. Pal, Ultrafast resonance energy transfer in biomolecular systems. *Eur. Phys. J. D*, **60** (2010) 137.
 21. D. Banerjee and S.K. Pal, Simultaneous binding of minor groove binder and intercalator to dodecamer DNA: Importance of relative orientation of donor and acceptor in FRET. *J. Phys. Chem. B*, **111** (2007) 5047.

22. S. Batabyal, T. Mondol and S.K. Pal, Picosecond-resolved solvent reorganization and energy transfer in biological and model cavities. *Biochimie*, **95** (2013) 1127.
23. A. Rodger and B. Norden, Circular dichroism and linear dichroism. 1997, Oxford: Oxford University Press.
24. N. Berova, K. Nakanishi and R.W. Woody, Circular dichroism. 2nd ed. 2000, New York: Wiley-VCH.
25. M. Tachiya, Application of a generating function to reaction kinetics in micelles. Kinetics of quenching of luminescent probes in micelles. *Chem. Phys. Lett.*, **33** (1975) 289.
26. M. Tachiya, Kinetics of quenching of luminescent probes in micellar systems. II. *J. Chem. Phys.*, **76** (1982) 340.
27. H. Gerner, Direct and sensitized photoprocesses of bis-benzimidazole dyes and the effect of surfactant and DNA. *Photochem. Photobiol.*, **73** (2001) 339.
28. R. Saha, P.K. Verma, R.K. Mitra and S.K. Pal, Structural and dynamical characterization of unilamellar AOT vesicles in aqueous solutions and their efficacy as potential drug delivery vehicle. *Colloids Surf., B*, **88** (2011) 345.
29. R.F. Ismagilov, A.D. Stroock, P.J.A. Kenis, G. Whitesides and H.A. Stone, Experimental and theoretical scaling laws for transverse diffusive broadening in two-phase laminar flows in microchannels. *Appl. Phys. Lett.*, **76** (2000) 2376.
30. K.J. Laidler, Chemical Kinetics. 3rd ed. 1987: Prentice Hall.
31. J.N. Israelachvili, D.J. Mitchell and B.W. Ninham, Theory of self-assembly of hydrocarbon amphiphiles into micelles and bilayers. *J. Chem. Soc., Faraday Trans.*, **272** (1976) 1525.
32. D.J. Mitchell and B.W. Ninham, Micelles, vesicles and microemulsions. *J. Chem. Soc., Faraday Trans.*, **77** (1981) 601.
33. H.H. Paradies, Shape and size of a nonionic surfactant micelle. Triton X-100 in aqueous solution. *J. Phys. Chem.*, **84** (1980) 599.

34. S.S. Berr, Solvent isotope effects on alkytrimethylammonium bromide micelles as a function of alkyl chain length. *J. Phys. Chem.*, **91** (1987) 4760.
35. S.S. Berr, E. Caponetti, J.S. Johnson, J.R.R.M. Jones and L.J. Magid, Small-angle neutron scattering from hexadecyltrimethylammonium bromide micelles in aqueous solutions. *J. Phys. Chem.*, **90** (1986) 5766.
36. N.J. Turro, X.-G. Lei, K.P. Ananthapadmanabhan and M. Aronson, Spectroscopic probe analysis of protein-surfactant interactions: The BSA/SDS system. *Langmuir*, **11** (1995) 2525.
37. P.A. Hassan, S.R. Raghavan and E.W. Kaler, Microstructural changes in SDS micelles induced by hydrotropic salt. *Langmuir*, **18** (2002) 2543.
38. A.K. Shaw and S.K. Pal, Activity of subtilisin carlsberg in macromolecular crowding. *J. Photochem. Photobiol., B*, **86** (2007) 199.
39. P.L. Luisi, M. Giomini, M.P. Pileni and B.H. Robinson, Reverse micelles as hosts for proteins and small molecules. *BBA*, **947** (1988) 209.
40. K.E. Tettey and D. Lee, Effect of thermal treatment and moisture content on the charge of silica particles in non-polar media. *Soft Matter*, **9** (2013) 7242.
41. B. Cohen, D. Huppert, K.M. Solntsev, Y. Tsfadia, E. Nachliel and M. Gutman, Excited state proton transfer in reverse micelles. *J. Am. Chem. Soc.*, **124** (2002) 7539.
42. M.P. Pileni, Water in oil colloidal droplets used as microreactors. *Adv. Colloid Interface Sci.*, **46** (1993) 139.
43. C. Petit, P. Lixon and M.P. Pileni, Structural study of divalent metal bis(2-ethylhexyl) sulfosuccinate aggregates. *Langmuir*, **7** (1991) 2620.
44. T.K. Jain, M. Varshney and A. Maitra, Structural studies of aerosol of reverse micellar aggregates by Ft-Ir spectroscopy. *J. Phys. Chem.*, **93** (1989) 7409.
45. M.A. Middleton, R.S. Schechter and K.P. Johnston, Dielectric-properties of anionic and nonionic surfactant microemulsions. *Langmuir*, **6** (1990) 920.

46. D.M. Zhu, X. Wu and Z.A. Schelly, Reverse micelles and water in oil microemulsions of triton x-100 in mixed-solvents of benzene and n-hexane. Dynamic light-scattering and turbidity studies. *Langmuir*, **8** (1992) 1538.
47. J.F. Foster, Some aspects of the structure and conformational properties of serum albumin. 1977, Oxford: Pergamon.
48. M. Dockal, D.C. Carter and F. R  ker, The three recombinant domains of human serum albumin: Structural characterization and ligand binding properties. *J. Biol. Chem.*, **274** (1999) 29303.
49. X.M. He and D.C. Carter, Atomic structure and chemistry of human serum albumin. *Nature*, **358** (1992) 209.
50. J. Ghuman, P.A. Zunszain, I. Petitpas, A.A. Bhattacharya, M. Otagiri and S. Curry, Structural basis of the drug-binding specificity of human serum albumin. *J. Mol. Biol.*, **353** (2005) 38.
51. M. Wardell, Z. Wang, J.X. Ho, J. Robert, F. R  ker, J. Ruble and D.C. Carter, The atomic structure of human methemalbumin at 1.9   . *Biochem. Biophys. Res. Commun.*, **291** (2002) 813.
52. J.A. Luetscher, Serum albumin. II. identification of more than one albumin in horse and human serum by electrophoretic mobility in acid solution. *J. Am. Chem. Soc.*, **61** (1939) 2888.
53. J.F. Foster, The plasma proteins. 1960, New York: Academic Press.
54. H.J. Nikkel and J.F. Foster, A reversible sulfhydryl-catalyzed structural alteration of bovine mercaptalbumin. *Biochemistry*, **10** (1971) 4479.
55. C.N. Cornell and L.J. Kaplan, Spin-label studies of the sulfhydryl environment in bovine plasma albumin. 2. The neutral transition and the A isomer. *Biochemistry*, **17** (1978) 1755.
56. C.O. Pabo, R.T. Sauer, J.M. Sturtevant and M. Ptashne, The λ -repressor contains two domains. *Proc. Natl. Acad. Sci. USA*, **76** (1979) 1608.

57. A.D. Johnson, B.J. Meyer and M. Ptashne, Interactions between DNA-bound repressors govern regulation by the λ phage repressor. *Proc. Natl. Acad. Sci. USA*, **76** (1979) 5061.
58. A. Mazumder, S. Bandyopadhyay, A. Dhar, D.E.A. Lewis, S. Deb, S. Dey, P. Chakrabarti and S. Roy, A genetic network that balances two outcomes utilizes asymmetric recognition of operator sites. *Biophys. J.*, **102** (2012) 1580.
59. A. Hochschild and M. Lewis, The bacteriophage λ CI protein finds an asymmetric solution. *Curr. Opin. Struct. Biol.*, **19** (2009) 79.
60. A.D. Hershey and M. Chase, Independent functions of viral protein and nucleic acid in growth of bacteriophage. *J. Gen. Physiol.*, **36** (1952) 39.
61. O. Avery, C. Macleod and M. MacCarty, Studies on the chemical nature of the substances inducing transformation of pneumococcal types. *J. Expt. Med.*, **7** (1944) 137.
62. J.D. Watson and F.H.C. Crick, Molecular structure of nucleic acids. A structure for deoxyribose nucleic acid. *Nature*, **171** (1953) 737.
63. D.L. Nelson and M.M. Cox, *Lehninger principles of biochemistry*. 2000, New York: W.H. Freeman & Co.
64. L.S. Lerman, The structure of the DNA-acridine complex. *Proc. Natl. Acad. Sci. USA*, **49** (1963) 94.
65. M.B. Lyles and I.L. Cameron, Interactions of the DNA intercalator acridine orange, with itself, with caffeine, and with double stranded DNA. *Biophys. Chem.*, **96** (2002) 53.
66. P.B. Dervan, Molecular recognition of DNA by small molecules. *Bioorg. Med. Chem.*, **9** (2001) 2215.
67. C. Burda, T.C. Green, S. Link and M.A. El-Sayed, Electron shuttling across the interface of CdSe nanoparticles monitored by femtosecond laser spectroscopy. *J. Phys. Chem. B*, **103** (1999) 1783.
68. P.G. Wu and L. Brand, Resonance energy transfer: Methods and applications. *Anal. Biochem.*, **218** (1994) 1.

69. R. Saha, S. Rakshit, D. Majumdar, A. Singha, R. Mitra and S. Pal, Nanostructure, solvation dynamics, and nanotemplating of plasmonically active SERS substrate in reverse vesicles. *J. Nanopart. Res.*, **15** (2013) 1576.
70. D. Banerjee, S.S. Sinha and S.K. Pal, Interplay between hydration and electrostatic attraction in ligand binding: Direct observation of hydration barrier at reverse micellar interface. *J. Phys. Chem. B*, **111** (2007) 14239.
71. D.P. Millar, R.J. Robbins and A.H. Zewail, Torsion and bending of nucleic acids studied by subnanosecond time-resolved fluorescence depolarization of intercalated dyes. *J. Chem. Phys.*, **76** (1982) 2080.
72. J. Olmsted and D.R. Kearns, Mechanism of ethidium bromide fluorescence enhancement on binding to nucleic acids. *Biochemistry*, **16** (1977) 3647.
73. R. Sarkar and S.K. Pal, Ligand-DNA interaction in a nanocage of reverse micelle. *Biopolymers*, **83** (2006) 675.
74. S.K. Pal, D. Mandal and K. Bhattacharyya, Photophysical processes of ethidium bromide in micelles and reverse micelles. *J. Phys. Chem. B*, **102** (1998) 11017.
75. F.M. Hamer, The chemistry of heterocyclic compound. The cyanine dyes and related compounds. 1963, New York: Interscience.
76. D. Mandal, S.K. Pal, D. Sukul and K. Bhattacharyya, Photophysical processes of merocyanine 540 in solutions and in organized media. *J. Phys. Chem. A*, **103** (1999) 8156.
77. J.A. Smyder and T.D. Krauss, Coming attractions for semiconductor quantum dots. *Mater. Today*, **14** (2011) 382.
78. Y. Yin and A.P. Alivisatos, Colloidal nanocrystal synthesis and the organic-inorganic interface. *Nature*, **437** (2005) 664.
79. T.-G. Iversen, T. Skotland and K. Sandvig, Endocytosis and Intracellular Transport of Nanoparticles: Present Knowledge and Need for Future Studies. *Nano Today*, **6** (2011) 176.

Chapter 3

Instrumentation and sample preparation

In this chapter the details of instrumental setup and sample preparation techniques used in our studies have been described.

3.1. Instrumental setups:

3.1.1. Steady-State UV-Vis absorption and emission measurement: Steady-state UV-Vis absorption and emission spectra of the probe molecules were measured with Shimadzu UV-2450 spectrophotometer and Jobin Yvon Fluoromax-3 fluorimeter, respectively. Schematic ray diagrams of these two instruments are shown in Figures 3.1 and 3.2.

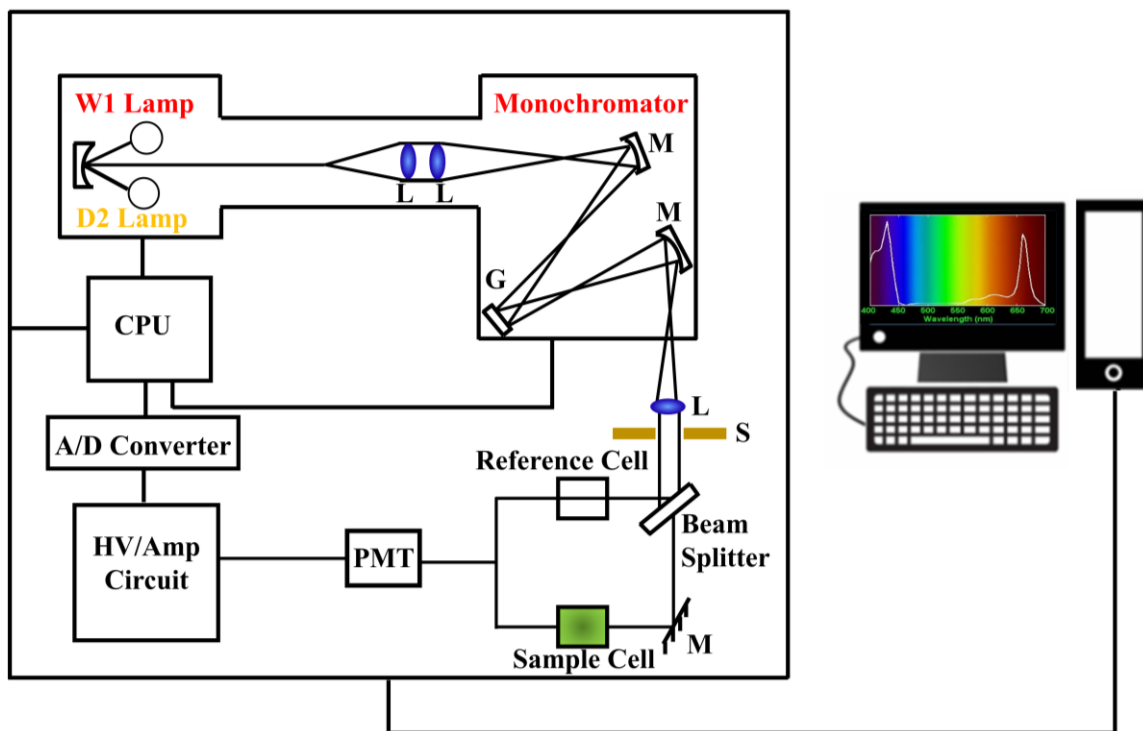


Figure 3.1. Schematic ray diagram of an absorption spectrophotometer. Tungsten halogen (W1) and deuterium lamps (D2) are used as light sources in the visible and UV regions, respectively. M, G, L, S, PMT designate mirror, grating, lens, shutter and photomultiplier tube, respectively. CPU, A/D converter and HV/amp indicate central processing unit, analog to digital converter and high-voltage/amplifier circuit, respectively.

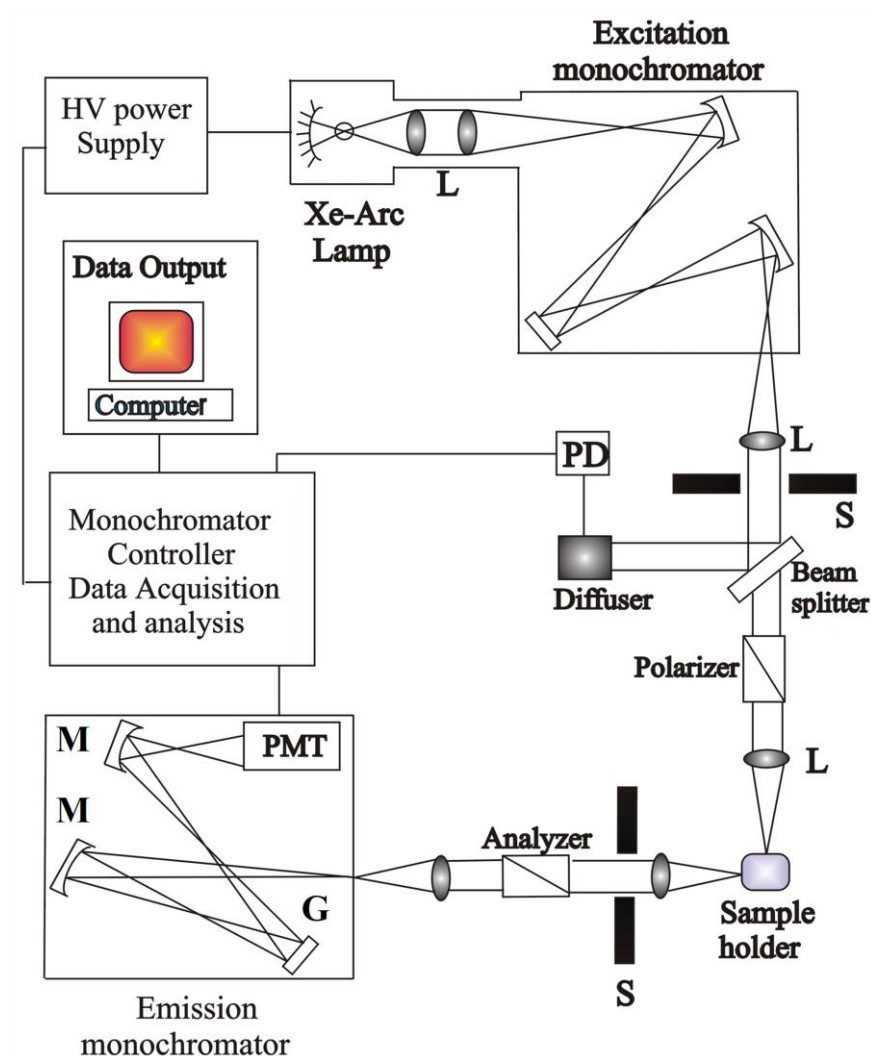


Figure 3.2. Schematic ray diagram of an emission spectrofluorimeter. M, G, L, S, PMT and PD represent mirror, grating, lens, shutter, and photomultiplier tube and reference photodiode, respectively.

3.1.2. Circular dichroism (CD) measurement: CD is a form of spectroscopy based on the differential absorption of left and right-handed circularly polarized light. It can be used to determine the structure of macromolecules (including the secondary structure of proteins and the handedness of DNA). The CD measurements were done in a JASCO spectropolarimeter with a temperature controller attachment (Peltier) (Figure 3.3). The CD spectra were acquired using quartz cells of 0.1 and 1.0 cm path length. For proteins and DNA the typical concentration used for CD measurements were within 10 μM .

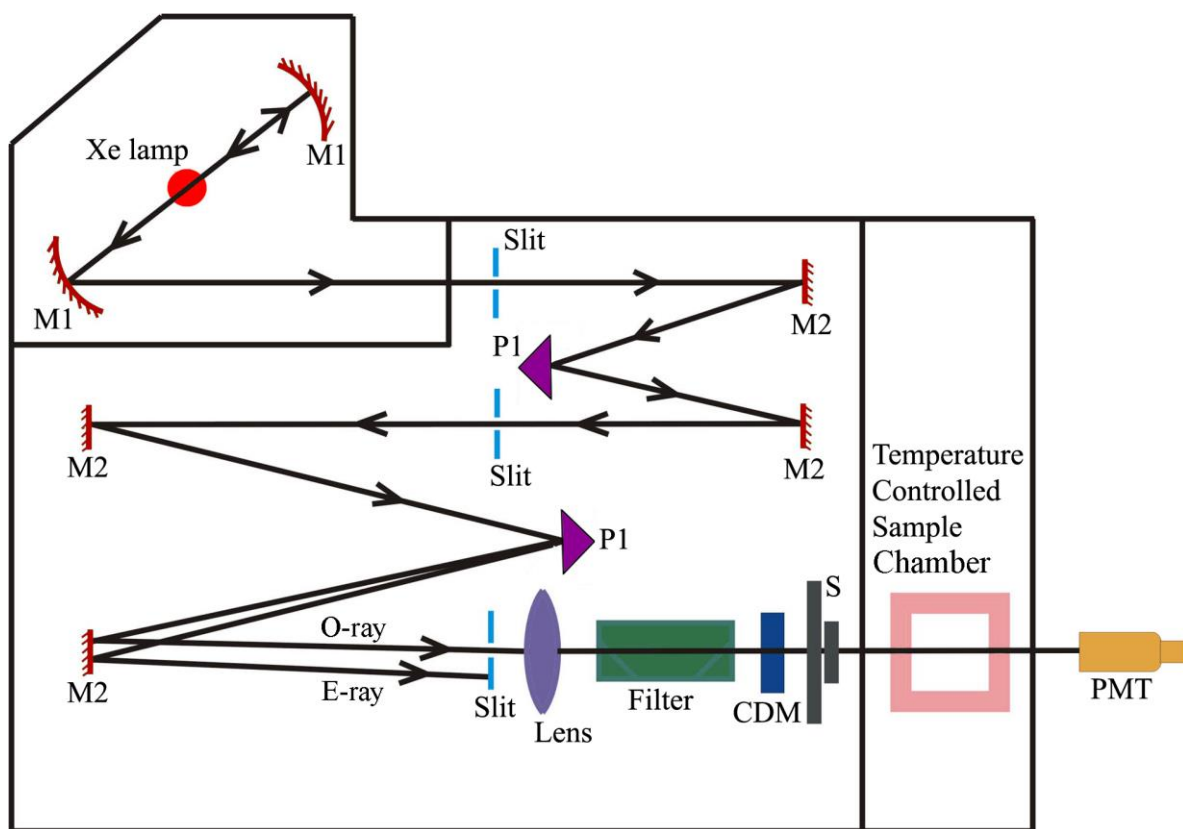


Figure 3.3. Schematic ray diagram of a circular dichroism (CD) spectropolarimeter. M1, M2, P1, S, PMT, CDM, O-ray and E-ray represent concave mirror, plain mirror, reflecting prism, photomultiplier tube, CD-modulator, ordinary ray and extraordinary ray, respectively.

3.1.3. Time-correlated single photon counting (TCSPC) technique: All the picosecond-resolved fluorescence transients were recorded using TCSPC technique. The schematic block diagram of a TCSPC system is shown in Figure 3.4. TCSPC setup from Edinburgh instruments, U.K., was used during fluorescence decay acquisitions. The instrument response functions (IRFs) of the laser sources at different excitation wavelengths varied between 70 ps to 80 ps. The fluorescence from the sample was detected by a photomultiplier after dispersion through a grating monochromator [1]. For all transients, the polarizer in the emission side

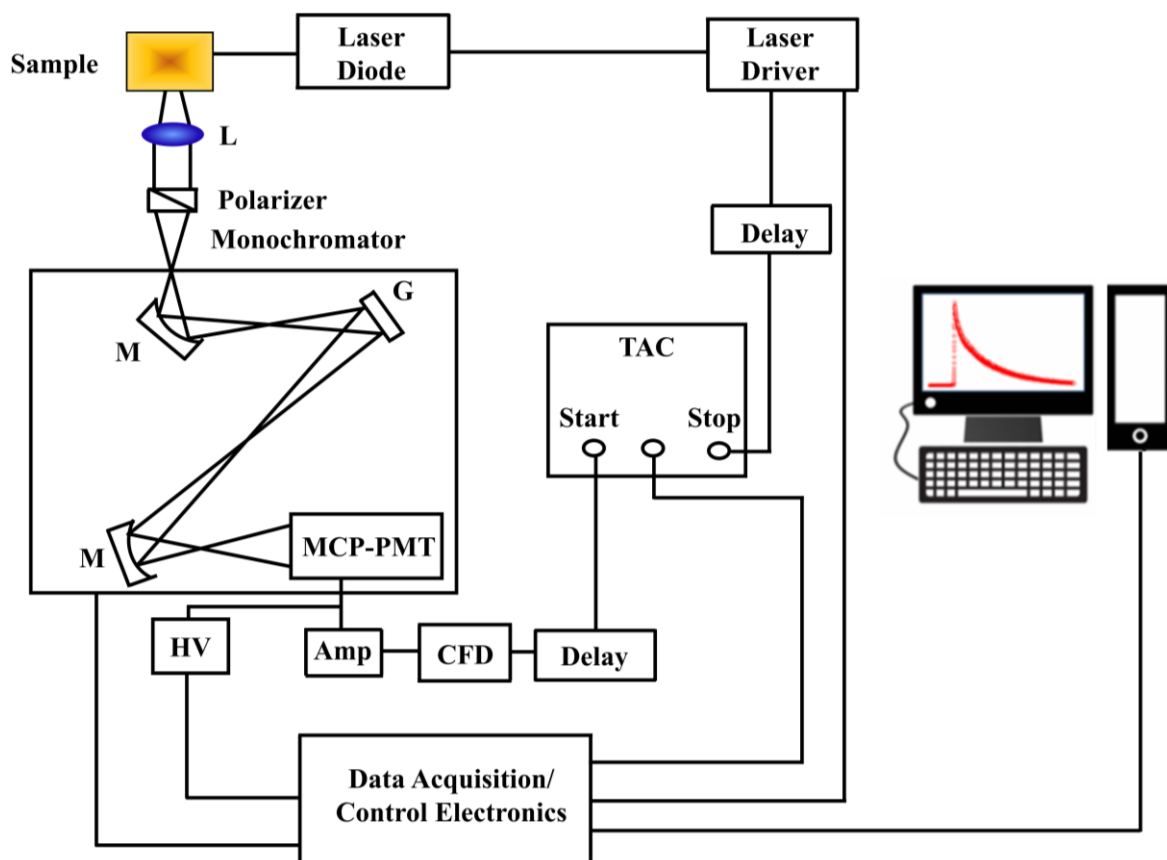


Figure 3.4. Schematic ray diagram of a time correlated single photon counting (TCSPC) spectrophotometer. A signal from microchannel plate photomultiplier tube (MCP-PMT) is amplified (Amp) and connected to start channel of time to amplitude converter (TAC) via constant fraction discriminator (CFD) and delay. The stop channel of the TAC is connected to the laser driver via a delay line. L, M, G and HV represent lens, mirror, grating and high voltage source, respectively.

was adjusted to be at 54.7° (magic angle) with respect to the polarization axis of excitation beam. In order to measure anisotropy, fluorescent transients were taken with emission polarizer aligned in parallel and perpendicular directions with respect to vertical polarization of excitation light. For tryptophan excitation of protein, femtosecond-coupled TCSPC setup were employed in which the sample was excited by the third harmonic laser beam (300 nm) of the 900 nm (0.5 nJ per pulse) using a mode-locked Ti-sapphire laser with an 80 MHz repetition rate (Tsunami, spectra physics), pumped by a 10 W Millennia (Spectra physics) followed by a pulse-peaker (rate 8 MHz) and a third harmonic generator (Spectra-physics, model 3980). The third harmonic beam was used for excitation of the

sample inside the TCSPC instrument (IRF = 70 ps) and the second harmonic beam was collected as for the start pulse.

3.1.4. Transmission electron microscope (TEM): A FEI TecnaiTF-20 field-emission high-resolution TEM (Figure 3.5) equipped with an energy dispersive X-ray (EDAX) spectrometer was used to characterize the microscopic

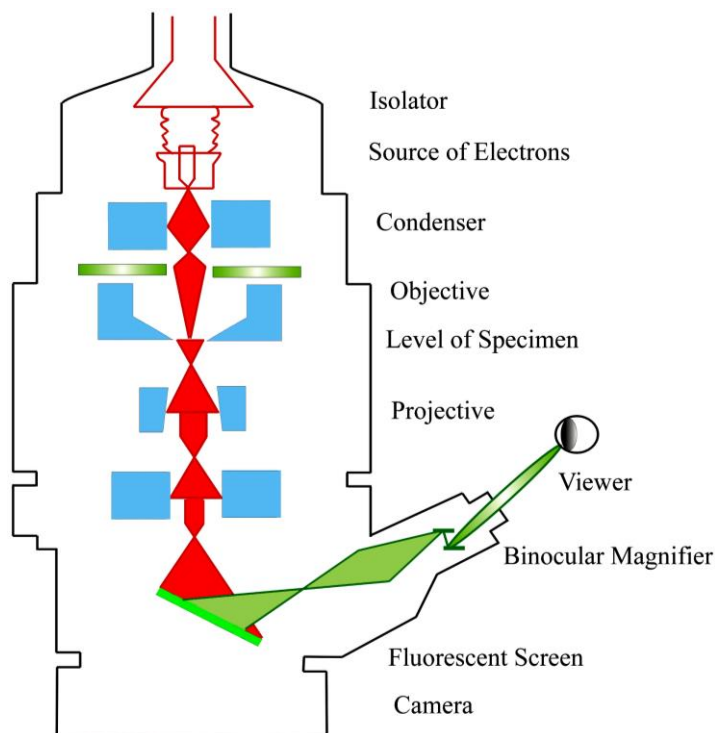


Figure 3.5. Schematic diagram of a typical transmission electron microscope (TEM). After the transmission of electron beam through a specimen, the magnified image is formed either in the fluorescent screen or can be detected by a CCD camera.

structures of samples and to analyze their elemental composition. The sizes of the quantum dots (QDs) were determined from the TEM images obtained at 200 kV acceleration voltage of the microscope. Samples for TEM were prepared by placing a drop of the QDs solution on a carbon-coated copper grid and allowing the film to evaporate overnight at room-temperature.

3.1.5. Scanning electron microscopy (SEM): Characterization of Ag thin film and PVA coated Ag/Si film were done by scanning electron microscope FE (field emission)-SEM; JEOL. Ltd., JSM-6500F. An electron-gun is attached to SEM and the electrons from filament triggered by 0 KV to 30 KV voltages. These electrons go first through a condenser lens and then through an objective lens, then through an aperture and finally reach to the specimen. The high energy electrons go a bit in the sample and back again give secondary electrons. The signal from secondary electrons are detected by detector and amplified. The ray diagram of the SEM setup is shown in Figure 3.6.

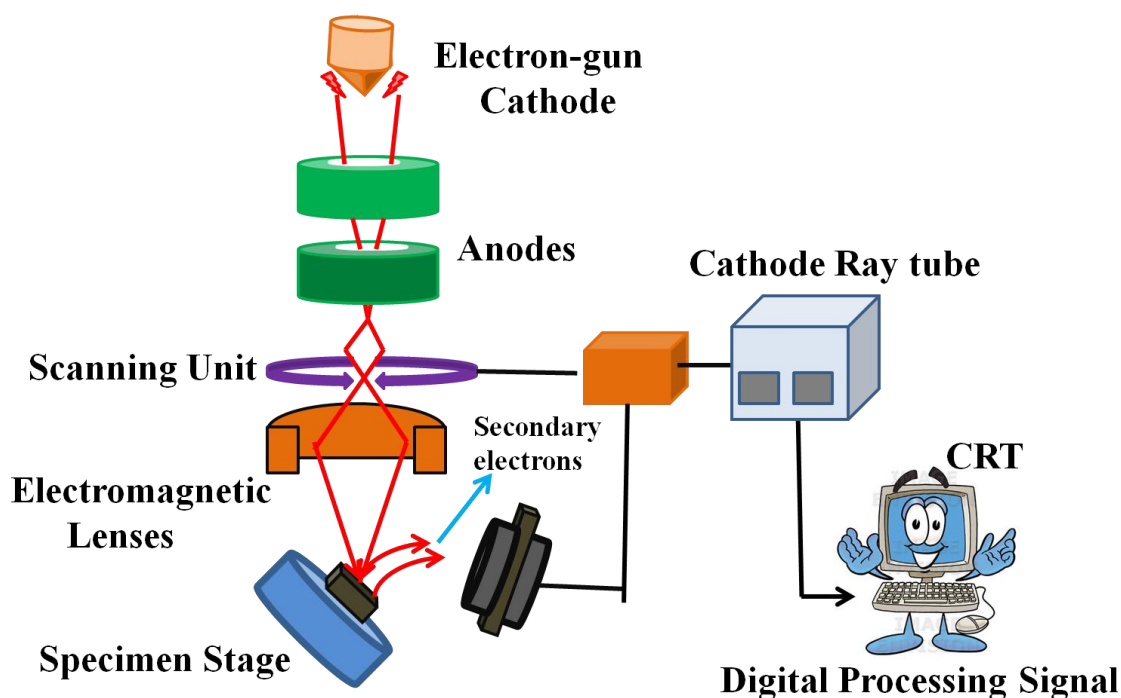


Figure 3.6. Schematic diagram of typical scanning electron microscope (SEM).

3.1.6. Microfluidics methodology: Figure 3.7 portrays the used microfluidics (MF) system, represented as the Y-shaped MF chip. The specially designed MF chip with the connectors and the syringe pumps (Atlas-ASP011) were bought from Dolomite, UK and Syrris Ltd., UK respectively. The specially designed MF chip consists of two inlets and a common outlet. The chip was made out of

optically transparent glass, which can sustain higher temperature if required. The diameter of the microchip (440 μm) was designed to withstand high flow rates. A small special region just after the confluence (X region) with a diameter of 150 μm and a length scale around 2200 μm was deliberately added in the design, after which it expands to 440 μm (Y region). The small diameter guarantees a higher fluid front velocity with reasonably low Reynolds number. The special geometry empowers to study very fast kinetics with a time resolution in the order of nanoseconds. For the study of slow kinetics in the range of millisecond to microsecond, the other portion of the microchannel with a diameter of 440 μm is suitable. The two inlets were attached to a syringe pump by capillary tubes.

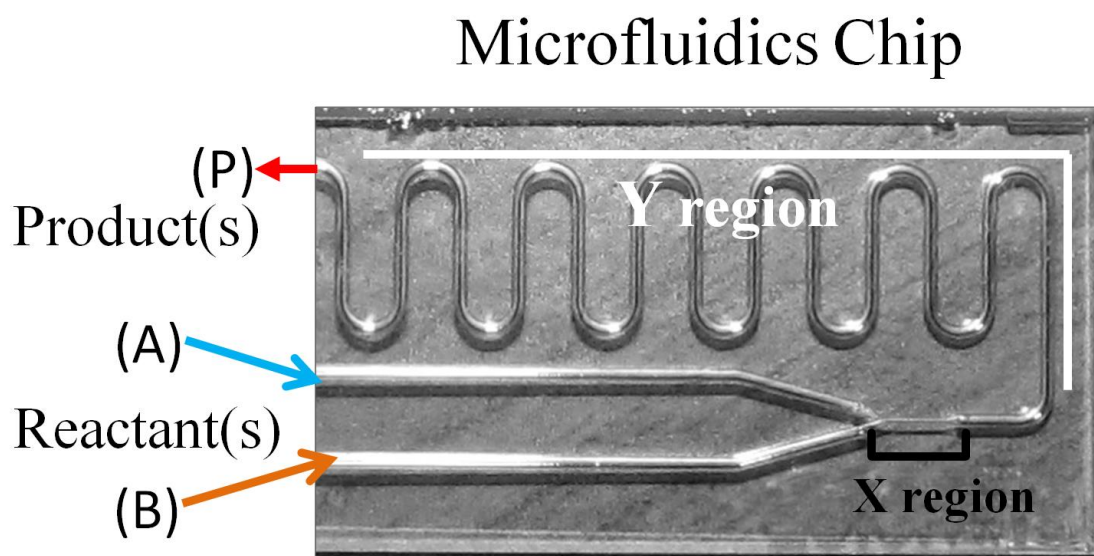


Figure 3.7. Custom designed microfluidics chip to monitor fast reaction. Two specific regions are shown: X, for fast sub-100 ns kinetics and Y, for slower kinetics [2].

The capillaries were passed through the shaft of the holder prior to connection with the MF chip. The reagents were propelled using the syringe pump and the total volumetric flow rate was adjusted according to the requirements.

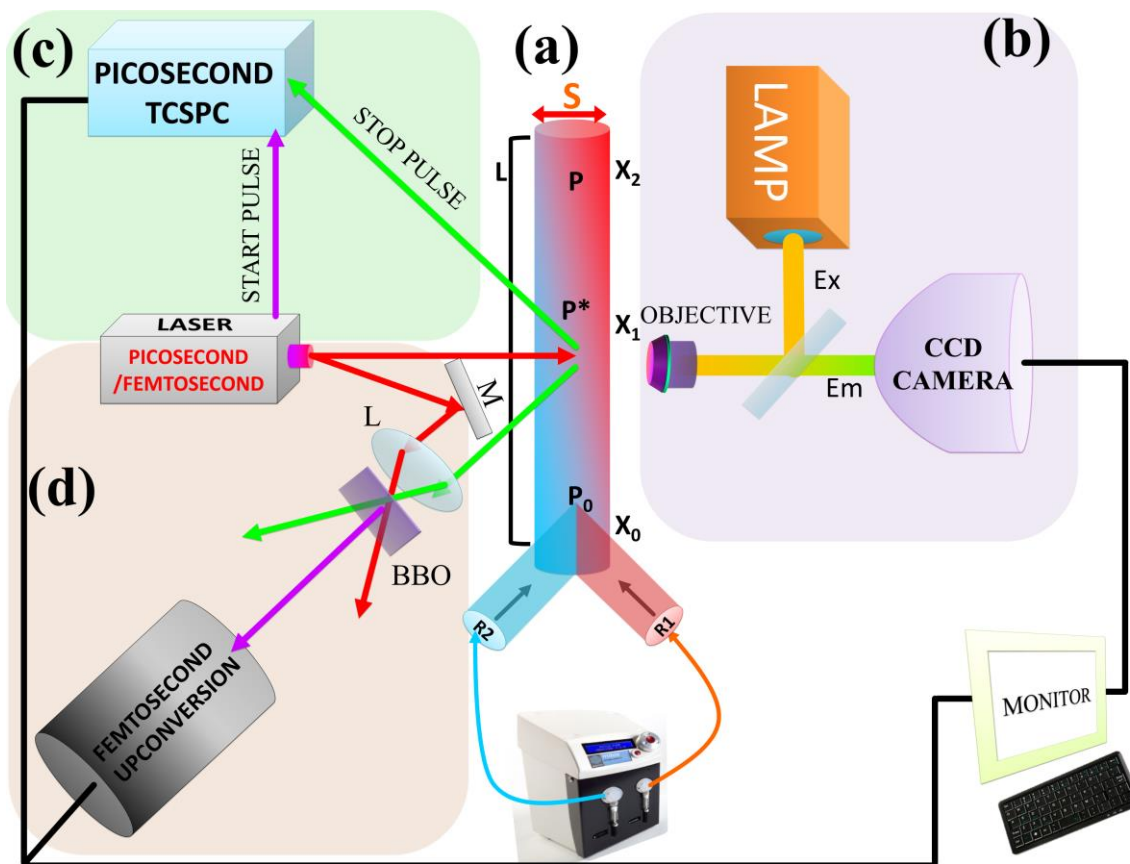


Figure 3.8. (a) Schematic presentation of the developed microfluidics platform. L denotes the flow path length, X_i are the positions for measurements along the channel and S is the cross section of the micro-channel. (b) The fluorescence microscope coupled to the microfluidics channel. A CCD camera captures images of the ongoing reactions inside the micro-channel. (c) Picosecond resolved fluorescence technique for the collection of decay profiles along the micro-channel. (d) Femtosecond upconversion technique combined with the microfluidics platform for studying ultrafast dynamics [2].

The term “flow rate” refers to the combined volumetric flow rate of the reagents through the micro-channel. The schematic of the MF channel is presented as a tube with a cross section S , length L , and total volume $V=SL$ (Figure 3.8). The streams converge and their mixing starts in the micro-channel junction, position X_0 in the Figure 3.8. The total length of the flow path of the micro-channel is around 10 cm. Fluorescence images were captured with a fluorescence microscope (BX-51, Olympus America, Inc.) equipped with a 100 W mercury arc lamp which was used as the excitation source (UV light excitation) and a DP72 CCD camera (Figure 3.8). The excitation light was cut off by using a standard filter and the fluorescence was

collected through a 10 \times objective. The image processing and analysis were done by the 'analySIS' software provided with the microscope. A region of interest (ROI) was selected at a specific height and width. This ROI was used to obtain an intensity profile along the microchannel. Intensity profiles were acquired at a particular microchannel distance from the initial mixing confluence. The RGB analysis was performed wherever required. This channel distance was converted into the reaction time (t_n) by dividing it by the velocity of the flow (U [m/s]), obtained from the known volumetric flow rate and cross-section (S) of the micro-channel [2].

3.1.7. Fluorescence microscope: Commercially available fluorescence microscope (BX-51, Olympus America, Inc.) was used in our study. The light source is usually a mercury-vapor lamp. For bright field, Tungsten-halogen lamp was used.

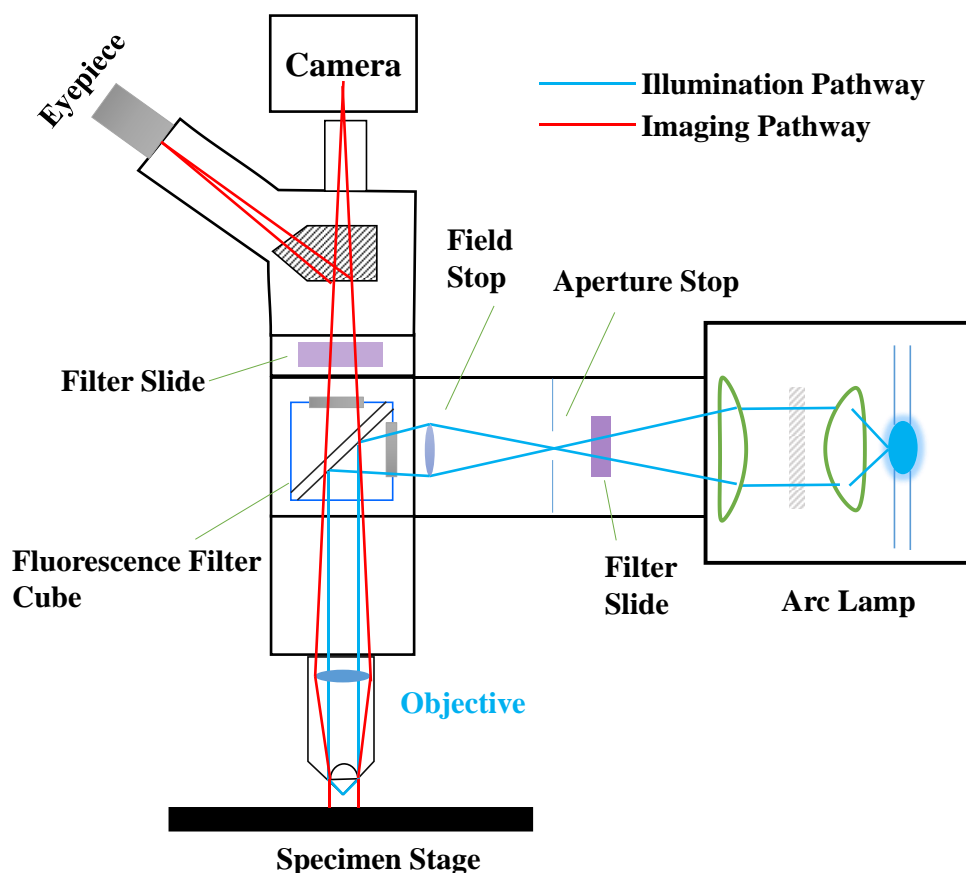


Figure 3.9. Schematic presentation of the fluorescence microscope.

In particular, an inverted setup with a mercury-vapor lamp as light source is shown. The dichroic mirror, excitation and emission filter are joined together within the filter cube (Figure 3.9). Since mercury-vapor lamps emit light over the whole optical spectrum as well as in the ultraviolet range, an optical excitation filter is used to isolate one specific wavelength. Due to the Stokes shift, it is possible to separate excitation and emission light in the same light path optically via a dichroic mirror. This way, only the emission light is collected by the objective. An emission filter helps to suppress unwanted background light.

3.2. Sample preparation: In this section the different sample preparation methods have been discussed.

3.2.1. Chemicals used: The chemicals, spectroscopic probes, and proteins were procured from the following sources. Double distilled water was used to prepare all the aqueous solutions. The chemicals Merocyanine-540 (1,3-dibutyl-5-[4-[3-(3-sulfopropyl)-2-benzoxazolinyldiene]-2,4-butyldiene]-2 thiobarbituric acid sodium salt), poly vinyl alcohol (PVA), toluene, silver nitrate (AgNO_3), sodium borohydride (NaBH_4), Salmon sperm DNA, Bis (2-ethylhexyl) sulphosuccinate (AOT), Tryptophan, Human serum albumin (HSA) were purchased from Sigma Aldrich. The fluorescent probes 2'-(4-hydroxyphenyl)-5-(4-methyl-1-piperazinyl)-2,5'-Bi-1H-benzimidazole trihydrochloride hydrate (H258), ethidium bromide (EtBr), dansyl chloride (DC) and acrylodan were purchased from Molecular probes. Sodium dodecyl sulphate (SDS) and cetyl trimethyl ammonium bromide (CTAB) were obtained from Fluka, and polyethylene glycol p-(1,1,3,3-tetramethylbutyl)-phenyl ether (TX-100) was purchased from ROMIL. *p*-Benzoquinone (BQ) was from Alfa Aesar. Sodium hydroxide and phenolphthalein were purchased from Merck. Acrylamide, isopropyl β -D-thiogalactopyranoside (IPTG), ampicillin, Coomassie brilliant blue, poly(ethyleneimine) and phenylmethanesulfonyl fluoride (PMSF) were purchased from Sigma Chemical Co. (St. Louis, MO). Bacto-tryptone, bacto-agar, and yeast extract were purchased from Difco Laboratories (Detroit, MI). β -Mercaptoethanol and glycerol were

purchased from Aldrich Chemical Co. (Milwaukee, WI). Operator 1 DNA (O_{R1}-5'CGTACCTCTGGCGGTGATAG3') and its complementary oligonucleotide, operator 2 DNA (O_{R2}-5'TACAACACGCACGGTGTAT3') and its complementary oligonucleotide were purchased from Trilink (USA). 100 mM phosphate buffer (pH 7) was prepared by using sodium dihydrogen phosphate (50 mM), di-sodium hydrogen phosphate (50 mM) in millipore water and the sample solutions were prepared in the same. All other reagents were of highest analytical grade quality.

3.2.2. λ -repressor isolation and purification: λ -repressor isolation and purification was carried out at IICB, Kolkata under the supervision of Prof. Siddhartha Roy. Plasmids pEA305 and *Escherichia coli* strains DH5- α and XL-1 blue were maintained as glycerol stocks at -80 °C. Luria broth was used as a growth medium which composed of 10 g bacto-tryptone, 5 g bacto-yeast extract and 5 g sodium chloride (NaCl) per litre. The pH was brought to 7.2 by addition of 1 M sodium hydroxide (NaOH). Luria agar (LA) was composed of 10 g bacto-tryptone, 5 g bacto-yeast extract, 15 g bacto-agar and 5 g NaCl per litre. Solutions used for repressor isolation and purification were lysis buffer and standard buffer. Lysis buffer was composed of 100 mM tris-HCl (pH 8.0) containing 1 mM ethylene diamine tetra acetic acid (EDTA) (pH 8.0), 2 mM calcium chloride (CaCl₂), 10 mM magnesium chloride (MgCl₂), 0.1 mM 2-mercaptoethanol, 200 mM potassium chloride (KCl) and 5 % glycerol (V/V). Standard buffer (SB) was composed of 10 mM tris-HCl (pH 8.0) containing 1 mM EDTA (pH 8.0), 2 mM CaCl₂, 0.1 mM 2-mercaptoethanol, 200 mM KCl and 5 % glycerol (V/V). Bacterial cells (XL1-gold and XL-1 blue) were grown until absorbance at 590 nm (A_{590} nm) reaches to 0.4-0.5 in LB and then chilled in ice for 10 minutes. The cells were then centrifuged at 4000 rpm for 5 minutes at 4 °C, suspended in half of the original volume of ice-cold 50 mM CaCl₂ and were kept at 0 °C for 15 minutes. It was then centrifuged at 4000 rpm for 5 minutes and the cells were re-suspended in 1/15th of the original volume of the ice-cold 50 mM CaCl₂ and were kept on ice for 24 hours after which,

the cells became competent and could be used for transformation with the desired DNA. A 0.2 ml of competent cell suspension was taken and a required amount of DNA in a maximum volume of 10 μ l tris-EDTA buffer was added to it. The DNA-cell mixture was kept on ice for 40 minutes, and then incubated at 42 $^{\circ}$ C in a water bath for 2 minutes and then allowed to stand on ice for 5 minutes. Next the cell suspension was diluted with 1 ml of LB and incubated at 37 $^{\circ}$ C in an incubator for 1-2 hours with shaking. An appropriate quantity of cell was then spread on ampicillin agar plate. The plate was incubated at 37 $^{\circ}$ C for 16-20 hours. The plasmids were isolated from the colonies. λ -repressor was isolated from a strain of *Escherichia coli* RR1 15 Δ lac Z carrying a plasmid pEA305 which contains the wild type *cl* gene (λ -repressor gene) under the control of *tac* promoter [3, 4].

The *tac* promoter is tryptophan-lac fusion promoter which is repressed by lac repressor and inducible with IPTG. λ -repressor constitutes about 30 % of the total cellular proteins in fully induced condition. The cells containing the above plasmid were grown until the absorbance at 590 nm (A_{590} nm) reaches to 0.6. Next, IPTG at a final concentration of 1 mM was added and grown for further 2 hours. Repressor was purified according to Johnson et al., [5] involving poly(ethyleneimine) precipitation followed by chromatography on CM-sephadex A-50 and hydroxylapatite column. The native repressor concentration was determined using extinction coefficient of 26300 mol $^{-1}$ cm $^{-1}$ at 280 nm. Molar concentration of the repressor was always calculated in terms of dimer subunit which consists of two identical subunits [6], designated as A and B. However, λ -repressor exists in tetramer-dimer equilibrium in our experimental condition. However, the equilibrium shifts towards the dimeric form in presence of operator DNA [7]. For all studies, the repressor was dialyzed against 0.1 M potassium phosphate buffer, pH 8.0.

3.2.3. Preparation of reverse micelle: Reverse micellar solutions of specific degree of hydration (w_0) were prepared by addition of calculated volume of aqueous solution of the probe in known volume of 100 mM AOT solution in isooctane [8].

In order to ensure that each reverse micelle contains not more than one probe molecule, the overall probe concentration was kept less than that of reverse micellar concentration.

3.2.4. Preparation of synthetic and genomic DNA solutions: In order to reassociate the single strand DNA into self-complimentary double stranded DNA (ds DNA), thermal annealing was performed as per the methodology prescribed by the vendor. Aqueous sample solutions of genomic DNA were prepared in phosphate buffer (pH ~7). The nucleotide concentrations were determined by absorption spectroscopy using the average extinction coefficient per nucleotide of the DNA ($6600 \text{ M}^{-1}\text{cm}^{-1}$ at 260 nm) [9].

3.2.5. Chemical modification of HSA: HSA, also known as endogenous serum albumin (ESA), was chemically modified to tag fluorescent probe, acrylodan. Briefly, a stock solution containing 100 mM HSA was prepared in 0.1 M phosphate buffer pH 7.0. A minimum amount of concentrated acrylodan solution in dimethylformamide (~40 μl) was added to 5 ml of the above solution to make final molar ratio of HSA to acrylodan to be 1:1. The mixture was stirred gently, and maintained at room temperature for 2 hours and then dialyzed at 4 $^{\circ}\text{C}$ against phosphate buffer. The dialysis buffer was changed at 12 hours intervals for 3 days.

3.2.6. Preparation of QDs-MC conjugate: QDs-merocyanine (MC) conjugate was prepared by overnight stirring of the QDs with MC in toluene followed by sonication and filtration to remove any undissolved MC in the solution. Because of the high affinity of ZnS to the sulfur compared to oxygen, on mixing CdSe/ZnS QDs with MC, the TOPO ligands around the QDs were replaced by MC due to the presence of sulfur atoms in it. Thus a surface-attached coupled dipole pair (D-A) is formed.

3.2.7. Preparation of silver mirror: The reflective silver mirror was prepared on a glass substrate by chemical reduction of silver nitrate by sodium hydroxide in presence of sugar and ammonium hydroxide.

References

1. D.V. O'Conner and D. Philips, Time correlated single photon counting. 1984, London: Academic Press.
2. S. Batabyal, S. Rakshit, S. Kar and S.K. Pal, An improved microfluidics approach for monitoring real-time interaction profiles of ultrafast molecular recognition. *Rev. Sci. Instrum.*, **83** (2012) 043113.
3. R. Saha, U. Banik, S. Bandopadhyay, N.C. Mandal, B. Bhattacharyya and S. Roy, An operator-induced conformational change in the C-terminal domain of the λ -repressor. *J. Biol. Chem.*, **267** (1992) 5862.
4. U. Banik, R. Saha, N.C. Mandal, B. Bhattacharyya and S. Roy, Multiphasic denaturation of the λ -repressor by urea and its implications for the repressor structure. *Eur. J. Biochem.*, **206** (1992) 15.
5. A.D. Johnson, C.O. Pabo and R.T. Sauer, Bacteriophage λ -repressor and cro protein: Interactions with operator DNA. *Methods Enzymol.*, **65** (1980) 839.
6. C. Brack and V. Pirrotta, Electron microscopic study of the repressor of bacteriophage λ and its interaction with operator DNA. *J. Mol. Biol.*, **96** (1975) 139.
7. U. Banik, N.C. Mandal, B. Bhattacharyya and S. Roy, A fluorescence anisotropy study of tetramer-dimer equilibrium of λ -repressor and its implication for function. *J. Biol. Chem.*, **268** (1993) 3938.
8. R. Saha, S. Rakshit, P.K. Verma, R.K. Mitra and S.K. Pal, Protein-cofactor binding and ultrafast electron transfer in riboflavin binding protein under the spatial confinement of nanoscopic reverse micelles. *J. Mol. Recognit.*, **26** (2013) 59.
9. G. Cosa, K.-S. Focsaneanu, J.R.N. McLean, J.P. McNamee and J.C. Scaiano, Photophysical properties of fluorescent DNA dyes bound to single and double stranded DNA in aqueous buffered solution. *Photochem. Photobiol.*, **73** (2001) 585.

Chapter 4

Time-resolved spectroscopic studies on biological and engineered environment

4.1. Introduction: The hydrophobic effect, the interaction of waters with nonpolar molecules, is very crucial in various fields of scientific research and most important in biomolecular structure and function [1]. Particularly, structure and energetics of water molecules in the hydrophobic cavity/cleft of protein trigger a number of research works in the field of experimental biophysics [2-6]. In most of the time “disordered” water molecules in hydrophobic protein cavities are essentially missed in X-ray crystallographic studies, however, clearly revealed in NMR structural studies [7]. From a number of recent experiments, it is an accepted fact that dynamical behavior of water molecules in hydrophobic protein cavities is not unique, rather very much case specific and depends on the structural (slower) [3] and functional (faster) [5] requirements of the protein. For example, due to substantial negative free energy generated by high enthalpy and low entropy factors, water molecules present within the substrate binding cavity of α -chymotrypsin are expelled easily upon ligand binding [8]. In many proteins, nonpolar cavities are often located at or near the active site and are thought to be involved in the uptake, transfer, and release of both nonpolar and polar molecules [9]. One of such examples include the presence of a cleft around Cys 34 (Figure 4.1) in the domain I of endogenous serum albumin (ESA), which is reported to be responsible for the binding of an anticancer drug doxorubicin [10]. The X-ray structure of the native protein reveals that Cys 34 residing in a hydrophobic crevice that is $\sim 10\text{-}12$ Å deep from the protein surface [10]. Site selective acrylodan labelling of Cys 34, offers unique opportunity to investigate the dynamics of water molecules in the cleft. In recent past, Zewail group explored the hydration

dynamics using site selective acrylodan probe at Cys 34 and correlated the dynamics with unfolding pathways of the protein [11]. As mentioned in a review of biological water [12], femtosecond dynamics essentially reveal rotational and inertial (roto-translational) motions of water molecules, however, complete diffusion of water molecules in the several hundred ps to ns time scales, is expected to be beyond experimental time windows of the measurement.

In the this study, we have selectively labeled Cys 34 using thiol reactive probe acrylodan and probed the environmental dynamics with picosecond time resolution in an experimental time window of several 10s of nanoseconds. The hydrophobic crevice on the protein surface at Cys 34 is approximately 10-12 Å deep [10] and careful observation of the crystal structure [13] reveals the presence of 4-5 water molecules within 10 Å distance from Cys 34 residue. Temperature dependent solvation dynamics over wide range of physiologically relevant temperature region (10-70 °C) clearly indicates that dynamics is essentially due to the water molecules in the cleft and follows Arrhenius type behavior up to 60 °C, beyond which the structural integrity of the protein is not preserved [14]. Significant spectral overlap of the single tryptophan (Trp 214) with the site-selective probe acrylodan offers unique opportunity to apply Förster resonance energy transfer (FRET) for the investigation of distance with molecular resolution between two specific sites at various temperatures, thus revealing the structural integrity of the protein in our experimental condition [15]. The distance distribution between donor and the acceptor in our experimental condition was also investigated. Fluorescence anisotropy of acrylodan attached to Cys 34 at different temperatures reveal that physical motion of the probe is much slower than the reorganization of the immediate environments of the probe. In order to understand the importance of the water molecules in the solvation of acrylodan probe in the protein cleft, we have extended our studies on a nano-sized water pool of AOT reverse micelles (RMs) [16-18]. Similarity of the dynamics of the

protein with that of RMs ($w_0=5$), indicates that the dynamics is essentially from water. A careful comparison of our dynamics in the above systems with those in MD simulation studies [19] reveal an interesting water dynamics in the cleft. The bound water molecules in the lower temperature undergo quasibound state, where the water molecules get immobilized by double or more hydrogen bond bridges and exhibit slower dynamics compared to free water molecules [20].

4.2. Results and discussion:

4.2.1. Picosecond-resolved solvent reorganization and energy transfer in biological and model cavities [21]: Figure 4.2a depicts the fluorescence characteristics of acrylodan probe attached to Cys 34 residue of endogenous serum albumin (ESA). As shown in the figure, the emission is blue shifted from 530 nm (in buffer) to 488 nm upon covalent attachment to Cys 34 residue in protein. As the fluorescence of acrylodan is very sensitive to the polarity of the medium [22], it can be used to probe the solvation dynamics in the surrounding environment [11].

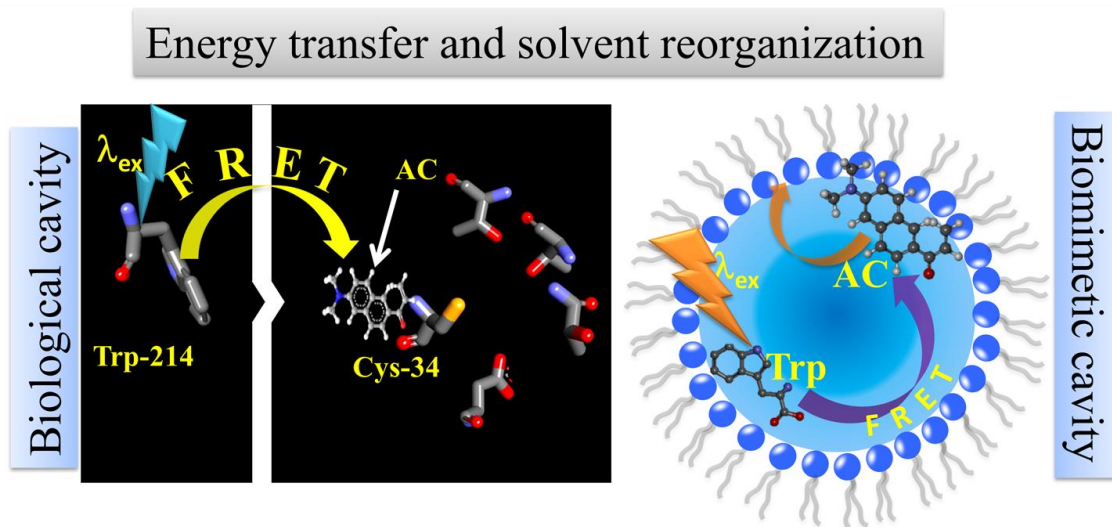


Figure 4.1. The cavity region around Cys 34 in the protein is schematically presented (Left). FRET from intrinsic tryptophan to acrylodan residing in the cavity attached to Cys 34 occurs upon excitation of tryptophan residue in the protein. In artificial biomimetic, AOT reverse micelle, the occurrence of FRET from tryptophan to acrylodan is schematically shown (Right).

With increasing temperature (10-70 °C), the emission of the probe in the protein is observed to be slightly blue shifted (Figure 4.2a), which indicates that probe resides in hydrophobic cleft even at elevated temperatures. Figure 4.2b reveals temperature dependent picosecond-resolved FRET from intrinsic tryptophan of ESA to extrinsic fluorescent probe acrylodan. It is well documented that tryptophan and acrylodan serve as excellent FRET pair [23, 24] as there is significant spectral overlap between tryptophan emission and acrylodan absorption spectrum. The FRET study confirms the location of the probe (Figure 4.1) and also elucidates structural integrity of the protein at various temperatures (10-70 °C). As evident in the inset of Figure 4.2b, at 10 °C, the lifetime of tryptophan is significantly quenched in acrylodan labeled ESA in comparison to unlabeled ESA. The lifetime quenching occurs due to the nonradiative energy transfer from tryptophan to acrylodan (FRET). From the observed FRET efficiency of 83% at 10 °C, the distance ($r=36 \text{ \AA}$) between tryptophan and acrylodan was estimated according to equation (2.53) and found to be in good agreement with the distance ($\sim 40 \text{ \AA}$) between Cys 34 and Trp 214 as revealed from the X-ray crystal structure (PDB code: 2XSI [13]).

At 10 °C, tryptophan in ESA has lifetime decay components of 0.18 ns (20%), 3.16 ns (25%) and 7.96 ns (55%) with average lifetime of 5.13 ns. In the acrylodan labeled ESA, the lifetime components of tryptophan becomes 0.10 ns (54%), 0.97 ns (33%) and 4.20 ns (13%) with average lifetime of 0.9 ns. With increasing temperature, lifetime of tryptophan in both labeled and unlabeled protein is affected due to the perturbation of the secondary structure of the protein. As shown in the inset of Figure 4.2b, at 70 °C, the tryptophan lifetime becomes faster in both the cases and overall FRET efficiency is estimated to be 70%. The lifetime values of tryptophan under various conditions are summarized in Table 4.1.

Table 4.1. Fluorescence lifetimes (τ_i), average fluorescence lifetimes $\langle\tau_{avg}\rangle$, respective amplitudes (amp %) and FRET efficiency (E_{FRET} %) from tryptophan (Trp) to acrylodan (AC) at different temperatures.

Systems	Temperature (°C)	τ_1 (ns)	τ_2 (ns)	τ_3 (ns)	$\langle \tau_{avg} \rangle$ (ns)	E _{FRET} (%)
FRET in ESA						
Trp	10	0.15 (20%)	3.16 (25%)	7.96 (55%)	5.14	82.7
Trp-AC		0.10 (55%)	0.97(33%)	4.19 (12%)	0.89	
Trp	20	0.11 (20%)	1.93(15%)	6.99 (65%)	4.88	77.3
Trp-AC		0.08 (50%)	0.87 (30%)	3.79 (20%)	1.10	
Trp	30	0.15 (17%)	2.35 (21%)	6.66 (62%)	4.60	72.3
Trp-AC		0.18 (47%)	1.19 (32%)	3.97 (21%)	1.27	
Trp	40	0.10 (24%)	2.56 (31%)	6.51 (45%)	3.77	73.7
Trp-AC		0.11 (52%)	1.02 (30%)	3.73 (18%)	0.99	
Trp	50	0.09 (25%)	1.96 (25%)	5.23 (50%)	3.13	71.8
Trp-AC		0.20 (54%)	1.02 (33%)	3.48 (13%)	0.88	
Trp	60	0.17 (17%)	1.72 (37%)	4.43 (46%)	2.69	71.9
Trp-AC		0.14 (49%)	0.78 (38%)	3.15 (13%)	0.75	
Trp	70	0.18 (28%)	1.41 (46%)	3.99 (26%)	1.73	70.1
Trp-AC		0.11 (65%)	0.76 (28%)	3.53 (07%)	0.51	
FRET in AOT RMs						
Trp	10	0.10 (20%)	1.80 (30%)	6.21 (50%)	3.67	75.4
Trp-AC		0.10 (54%)	0.97 (33%)	4.23 (13%)	0.90	
Trp	20	0.11 (19%)	1.81 (34%)	6.19 (47%)	3.52	74.9
Trp-AC		0.11 (55%)	0.85 (31%)	4.22 (14%)	0.88	
Trp	30	0.14 (18%)	2.35 (21%)	6.66 (61%)	4.60	70.9
Trp-AC		0.15 (47%)	1.19 (33%)	4.13 (20%)	1.25	
Trp	40	0.10 (23%)	2.32 (29%)	5.52 (48%)	3.29	66.4
Trp-AC		0.12 (53%)	1.25 (30%)	4.11 (17%)	1.10	
Trp	50	0.08 (25%)	1.86 (28%)	4.82 (47%)	2.79	58.2
Trp-AC		0.12 (51%)	1.21(29%)	3.88 (20%)	1.16	
Trp	60	0.18 (28%)	1.68 (46%)	4.52 (26%)	1.98	52.1
Trp-AC		0.12 (53%)	1.02 (31%)	3.61 (16%)	0.94	
Trp	70	0.18 (28%)	1.65 (46%)	4.21 (26%)	1.86	48.5
Trp-AC		0.12 (53%)	1.02 (30%)	3.64 (17%)	0.96	

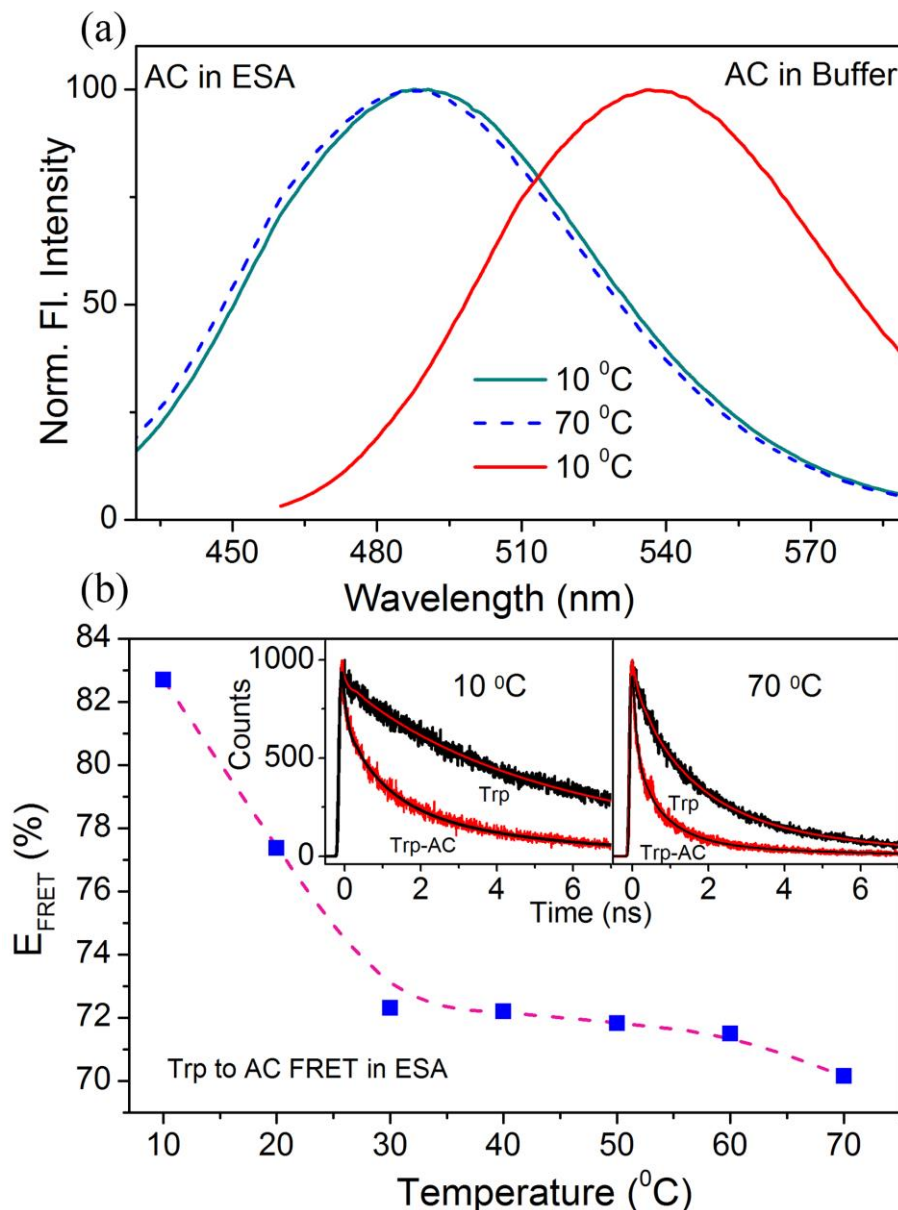


Figure 4.2. (a) Represents the steady-state emission spectrum of acrylodan (AC) in buffer and in serum albumin protein. The emission of acrylodan is significantly blue shifted in protein. The dotted line indicates the emission spectrum of acrylodan in ESA at elevated temperature (70 °C). (b) The energy transfer efficiency from tryptophan to acrylodan in the protein at various temperatures was estimated as represented in the figure. The dotted line is the guide to the eye. The inset figures show the lifetime quenching of tryptophan (Trp) in presence of acrylodan (Trp-AC) at two representative temperatures in ESA protein. Tryptophan was excited at 299 nm and emission was collected at 350 nm.

As shown in Figure 4.2b, the temperature dependent energy transfer profile consists of three distinct regions, 10 °C to 30 °C, 30 °C to 60 °C and above 60 °C. The efficiency up to 30 °C sharply decreases from 82% to 72% and remains almost

same up to 60 °C after which it starts to fall again. Around 60 °C, the protein structure is reported to be collapsed [14] which is well reflected in our temperature dependent FRET studies. The sharp change in the energy transfer efficiency with increase of temperature from 10 to 30 °C could be attributed to the different flexibilities of the protein domains (I, II and III) [11] at various thermal regions. However, the CD study [14] of thermal unfolding of the protein does not reveal any such specific pattern.

Table 4.2. Solvation correlation data for acrylodan in ESA and AOT RMs at different temperature values^b.

Temperature (°C)	a_1	τ_1 (ns)	a_2	τ_2 (ns)	$\langle \tau_{solv} \rangle$	E_a (kcal mol ⁻¹)
Acrylodan in ESA						1.80±0.1
10	0.39	0.30	0.60	0.28	0.25	
20	0.46	0.11	0.53	0.32	0.23	
30	0.50	0.11	0.50	0.29	0.20	
40	0.61	0.13	0.36	0.23	0.17	
50	0.68	0.11	0.31	0.25	0.15	
60	0.85	0.13	0.12	0.27	0.14	
70	0.72	0.14	0.28	0.18	0.15	
Acrylodan in AOT RMs						1.90±0.2
10	0.67	0.15	0.37	0.46	0.26	
20	0.68	0.15	0.38	0.46	0.26	
30	0.67	0.15	0.38	0.46	0.26	
40	0.65	0.15	0.36	0.43	0.25	
50	0.72	0.15	0.31	0.44	0.23	
60	0.80	0.14	0.23	0.46	0.21	
70	0.70	0.08	0.36	0.40	0.18	

^b τ represents the solvent correlation time constant, a represents its relative weight. τ_{solv} is the average solvation correlation decay time.

In order to exploit the local environmental dynamics around acrylodan attached to Cys 34 residue of ESA, wavelength dependent fluorescence transients of acrylodan in ESA were collected starting from lower (10 °C) to higher temperatures (70 °C). The fluorescence transients collected at blue end, decay faster in comparison to the transients collected at the red end of the spectrum.

Table 4.3. Fluorescence anisotropy decays, Wobbling-in-Cone data, microviscosity around the probe and energy barrier for viscous flow of acrylodan in ESA and in AOT RMs at different temperature values.

Temperature ($^{\circ}\text{C}$)	τ_{slow} (ns)	τ_{fast} (ns)	τ_{rot} (ns)	θ_W (deg)	$D_W \times 10^8$ (s^{-1})	η_m (cP)	E_n (kcal mol $^{-1}$)
Acrylodan in ESA							1.90 \pm 0.2
10	60 (97%)	0.53 (03%)	58.33	7.8	0.10	8.38	
20	55 (95%)	0.49 (05%)	52.50	10.1	0.18	8.09	
30	42 (96%)	0.41 (04%)	40.62	8.5	0.15	6.97	
40	40 (96%)	0.38 (04%)	39.12	6.9	0.11	6.71	
50	36 (97%)	0.30 (03%)	35.21	6.9	0.14	5.41	
60	29(98%)	0.11 (02%)	28.42	6.6	0.35	2.04	
70	15 (94%)	0.05 (04%)	14.44	9.0	1.44	0.95	
Acrylodan in AOT RMs							2.05 \pm 0.2
10	22 (67%)	0.67 (33%)	14.96	29.1	0.99	10.28	
20	20 (65%)	0.60 (35%)	13.21	30.1	1.18	9.33	
30	18 (64%)	0.53 (36%)	11.71	30.6	1.37	8.63	
40	16 (63%)	0.40 (37%)	10.23	31.2	1.87	7.69	
50	15 (62%)	0.33 (28%)	9.42	31.7	2.34	6.32	
60	13 (61%)	0.28 (39%)	8.04	32.2	2.84	5.58	
70	12 (61%)	0.23 (39%)	7.41	32.2	3.46	4.75	

Time-resolved emission spectra (TRES) were constructed from the fluorescence decay transients for different temperatures. As illustrated in Figure 4.3a, at lower temperature (10 $^{\circ}\text{C}$), the net spectral shift in TRES was estimated 1500 cm^{-1} in 1 ns time window. The spectral shift decreases with increasing temperature and becomes 700 cm^{-1} at 70 $^{\circ}\text{C}$. The decrease in the spectral shift of 800 cm^{-1} , associated with faster solvation at elevated temperatures confirms that a considerable fraction of solvation is lost due to the transition of water molecules. Figure 4.3b represents the solvation correlation function ($C(t)$) constructed for acrylodan probe attached to Cys 34 in ESA at various temperatures. The solvation correlation decay profiles were fitted to bi-exponential function to obtain water relaxation times and corresponding decay constants are tabulated in Table 4.2. The overall decrease of solvation correlation decay time up to certain temperature range (~ 60 $^{\circ}\text{C}$) indicates that increase in temperature accelerates the solvation process leading to a decrease

in water relaxation time. The observed temperature-induced acceleration of solvation dynamics of acrylodan in ESA is associated with the transition of water molecules with temperature, which in turn is governed by an Arrhenius type of activation energy barrier crossing model [25, 26]. The activation energy barrier crossing model was applied in order to calculate the activation energy barrier (E_a) for water transition using the Arrhenius relation [25] using equation 2.46. The activation energy barrier (E_a) was found to be 1.80 ± 0.1 kcal mol⁻¹.

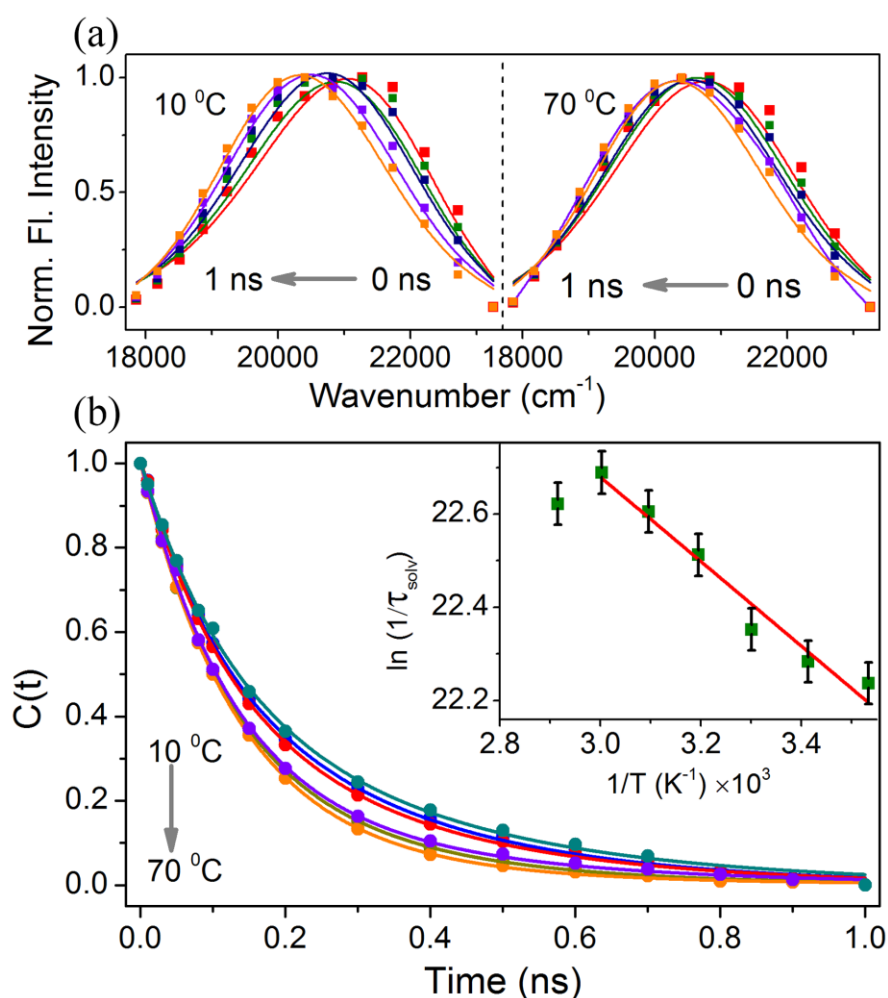


Figure 4.3. (a) Depicts the constructed TRES for acrylodan attached to Cys 34 in endogenous serum albumin (ESA) at two different temperatures, 10 °C and 70 °C. (b) Solvation correlation decay profiles of acrylodan in ESA at various temperatures are plotted. Inset shows the plot of $1/\tau_{solv}$ against $1/T$ (the solid line is a fitting to the Arrhenius equation with 1% error bar).

It is well documented that transition of bound to the bulk-type water is associated with a higher energy barrier of 7-8 kcal mol⁻¹, which is much higher than our estimated value [27, 28]. The activation energy barrier value is closely consisted with the transition of water from bound to quasibound state in the cavity around the probe attached to Cys 34 [20].

At this juncture, it is important to know the rotational flexibility of the probe acrylodan in the cavity in the experimental temperature range (10-70 °C). Figure 4.4a represents the polarization gated time-resolved anisotropy decay of acrylodan attached to Cys 34 at two different temperatures. As evident from the Figure 4.4a, at 10 °C, the anisotropy decay is much slower in comparison to that at 70 °C. The anisotropy decay collected at 10 °C consists of biexponential decay function having time constant of 60 ns (96 %) and 0.50 ns (04 %). The 60 ns component reveals the overall global motion of the protein molecule and is consistent with the reported value [29]. The shorter 0.5 ns component with insignificant weightage represents the rotational motion of the probe within its immediate microenvironment [29]. At elevated temperature of 70 °C, the anisotropy decay constants become 15 ns (93%) and 50 ps (7%). The average rotational time constants τ_{rot} , were estimated at various temperatures and summarized in Table 4.3. To account for the effect of temperature on the rotational relaxation process of the probe in the protein cavity, the anisotropy decays were analyzed using the wobbling-in-cone model [30]. Figure 4.4b represents the change of diffusion coefficient for wobbling motion (D_W) value with increasing temperature. The diffusion coefficient (D_W) values are of the same order of magnitude as reported in one of our earlier works on another probe in the protein [31].

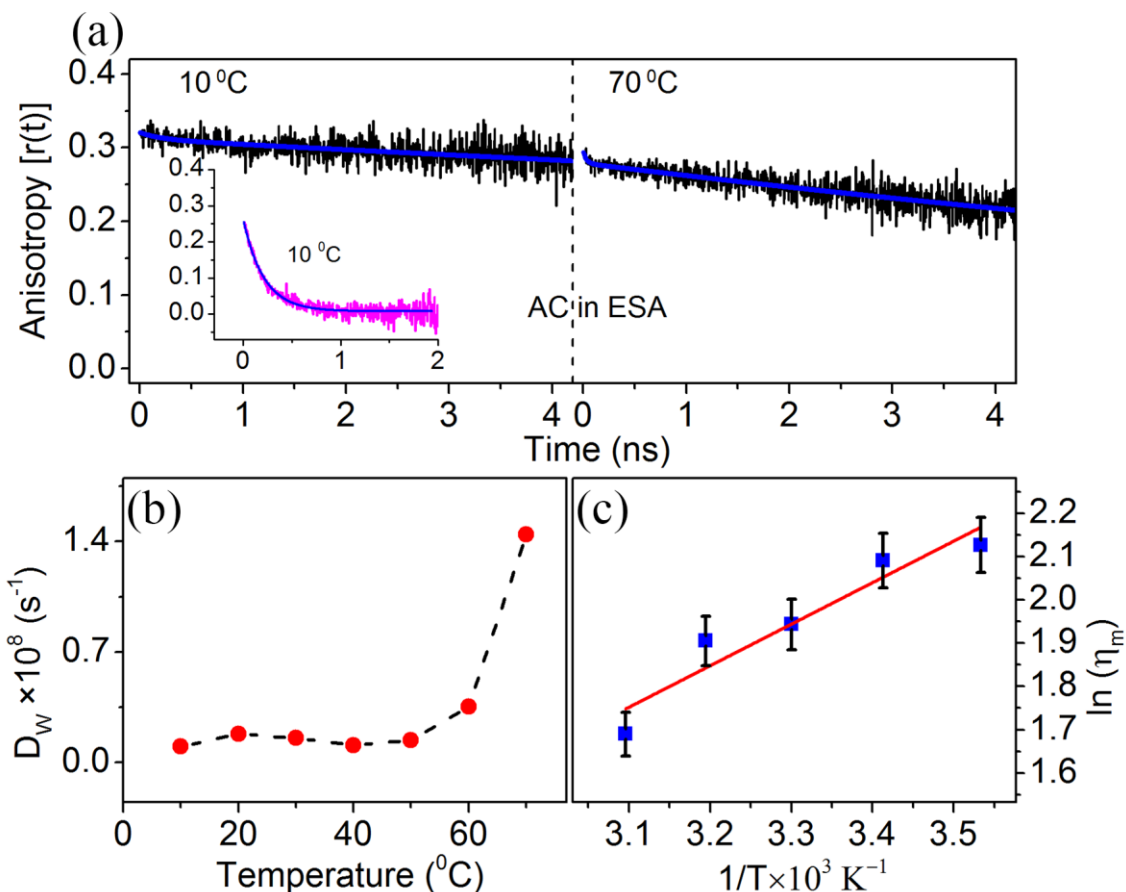


Figure 4.4. (a) Temporal decays of rotational anisotropy at 10 °C and 70 °C of acrylodan (AC) covalently attached to Cys 34 are shown. Inset figure depicts the rotational anisotropy of acrylodan ($\tau_{\text{rot}}=200 \text{ ps}$) in phosphate buffer (b) Diffusion coefficient for wobbling motion (D_w) of AC in ESA at different temperatures. Dotted line is guide to eye. (c) Plot of $\ln(\eta_m)$, η_m expressed in cP, against $1/T$ of AC in ESA with a linear fit (2% error bar included).

The corresponding semicone angles (θ_w) experienced by the acrylodan probe in different thermal regions are summarized in Table 4.3. The observation is consistent with higher lability of the probe AC in the protein cavity at elevated temperature. Figure 4.4c represents the plot of microviscosity, experienced by the probe at different temperatures. The energy barrier (E_η) for the viscous flow was obtained using the equation (2.41) by estimating the microviscosity (η_m) at different temperatures [32]. As shown in Figure 4.4c, a good linear fit was

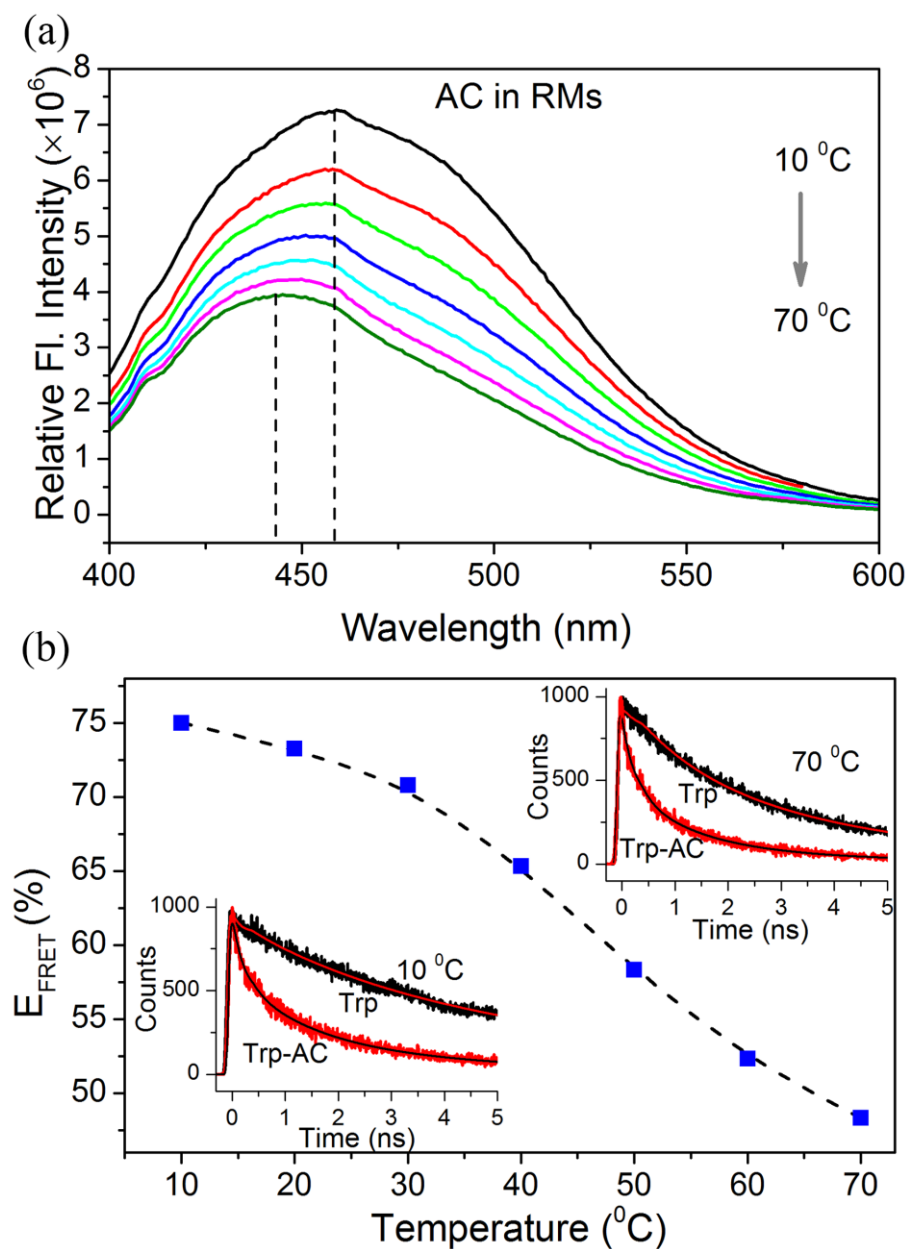


Figure 4.5. (a) Represents the steady-state emission spectrum of acrylodan (AC) in AOT reverse micelle at various temperatures. Acrylodan emission is blue shifted and quenched with increase of temperature. (b) The energy transfer efficiency from tryptophan to acrylodan at various temperatures was estimated as represented in the figure. The dotted line is the guide to the eye. The inset figures represent the lifetime quenching of tryptophan in RMs in presence of acrylodan at two different temperatures. Tryptophan was excited at 299 nm and emission was collected at 350 nm.

obtained with an estimated E_{η} value of 1.90 ± 0.2 kcal mol⁻¹. The good agreement between the energy barrier values (E_{η} obtained from the rotational anisotropy study and E_a value obtained from solvation dynamics study) is indicative of the

interlinking of the two processes involved in the cavity. It has to be noted that, there prevails a possibility of interference bond rotation in the solvation dynamics [33]. In our case, the possibility of interference of bond rotation in the solvation dynamics, can be safely rule out as the solvation time scale (τ_{solv} =230 ps) is much faster compared to the rotational flexibility of the probe (τ_{rot} =500 ps) as observed with time-resolved anisotropy study.

In order to compare the dynamics and energetics of water molecules with that in a well-known model biomimetic cavity, similar experiments were carried out in AOT reverse micelle (RMs) of w_0 =5. FRET from tryptophan to acrylodan in the model cavity was applied to confirm structural integrity of the cavity at various temperatures. The steady-state fluorescence spectra of AC in RMs of w_0 =5 are presented in Figure 4.5a. The [water]/[surfactant] ratio (w_0) was carefully chosen in our experiment. In one of our earlier studies, we have established that at w_0 =5, the effect of temperature on the size of the RMs is little or insignificant [31]. In addition, we noticed that the nonradiative twisted intramolecular charge transfer [34] feasibility of AC in RMs of w_0 =5 is minimum in comparison to higher w_0 values. As evident from Figure 4.5a with increase in temperature, the relative intensity of acrylodan decreases and the emission spectrum is blue shifted. In presence of acrylodan, the lifetime of tryptophan is significantly quenched due to FRET. The temperature dependency of the energy transfer process is represented in Figure 4.5b. The lifetime traces of tryptophan in absence and in presence of acrylodan for two different temperatures (10 °C and 70 °C) are shown in the insets of Figure 4.5b. The occurrence of FRET confirms the coexistence of tryptophan and acrylodan within AOT reverse micelle in our experimental temperature window.

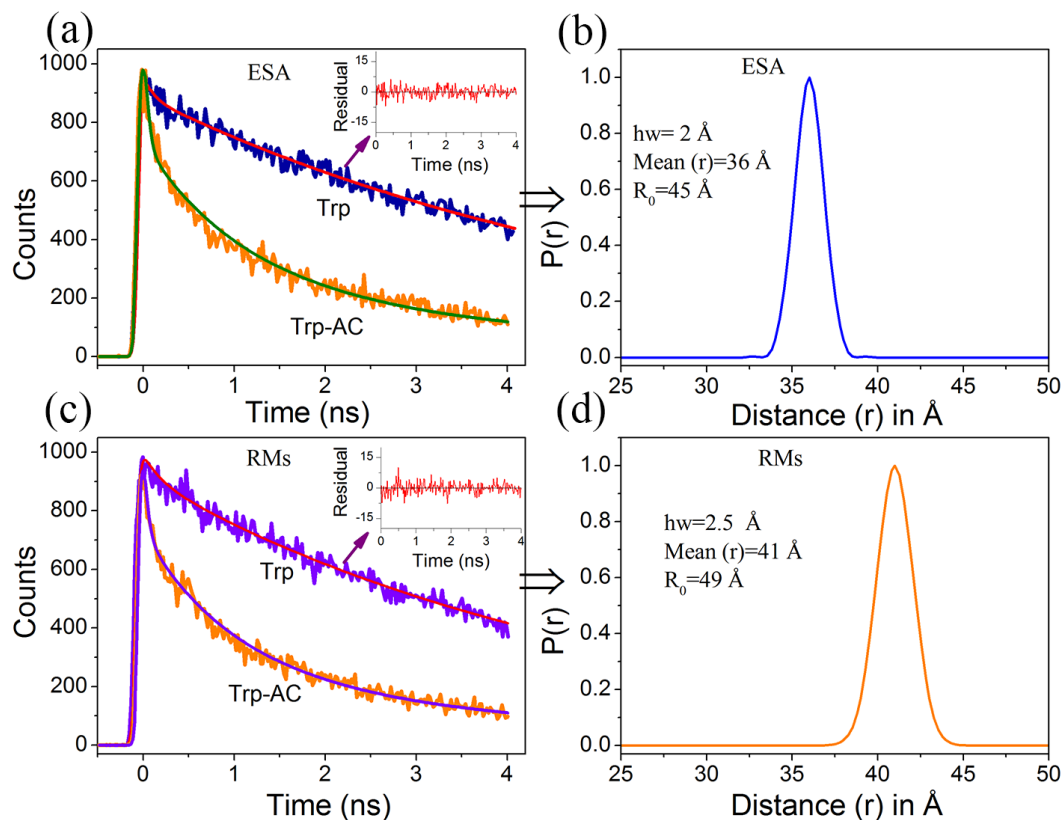


Figure 4.6. (a) and (c) depict the fitting of time-resolved lifetime traces considering the distance distribution between donor and acceptor in ESA and RMs respectively. The inset shows the residual of the fitting. (b) and (d) show the probability of distance distribution ($P(r)$) with respect to mean distance.

In order to understand the possible distribution of the acceptor molecules from the donor in the systems (protein and RMs), the fluorescence transients of the donor in absence and presence of acceptor were fitted following equations (2.54) & (2.55) and are shown in Figure 4.6. As shown in Figure 4.6, at 10 °C, the half width (hw) of the distance distribution functions are 2 Å and 2.5 Å for protein (Figure 4.6a and 4.6b) and RMs (Figure 4.6c and 4.6d) respectively. The observed narrow distribution in the donor acceptor distance in the studied system may indicate their dynamical flexibility.

The estimated energy transfer efficiencies at various temperatures are plotted in Figure 4.5b. As evident from the figure, energy transfer rate remains almost same up to 30 °C. With further increase of temperature, the energy transfer

efficiency gradually decreases. The lifetime decay constants of tryptophan in RMs under various temperatures are tabulated in Table 4.1. As evident from the energy transfer studies, the probe acrylodan resides within the interior of reverse micelle (Figure 4.1), which offers a unique opportunity to study the water dynamics of nano-size water pool inside the reverse micelle using the probe. Figure 4.7a depicts the constructed TRES of acrylodan in RMs at 10 °C and 70 °C respectively. It is evident from the figure that with increase of temperature, the net spectral shift decreases. The solvation correlation decay function, $C(t)$, of acrylodan was estimated for a temperature range of 10-70 °C and are represented in Figure 4.7b.

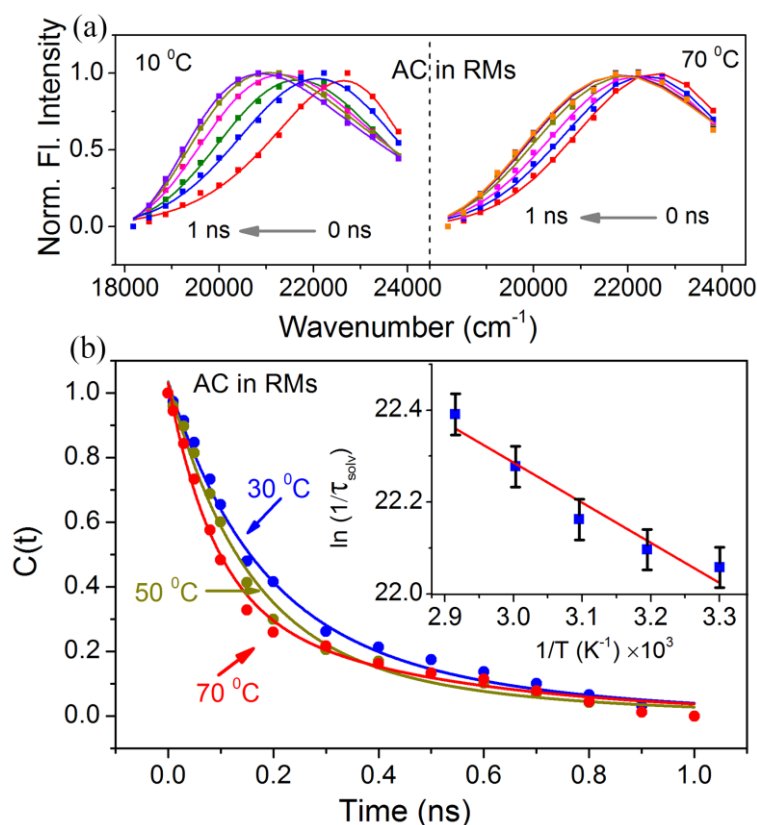


Figure 4.7. (a) Depicts the constructed TRES for acrylodan in AOT reverse micelle at lower and higher temperatures. (b) Solvation correlation decay profiles of acrylodan in RMs are plotted for various temperatures. When the temperature was increased from 10-30 °C, insignificant change in $C(t)$ was observed. Inset shows the plot of $1/\tau_{solv}$ against $1/T$ (the solid line is a fitting to the Arrhenius equation with 1% error bar).

It has to be noted that, the temperature dependent solvation correlation decay function of acrylodan in RMs follows a different course than that in the protein. When the temperature is raised from 10 °C to 30 °C, little or insignificant change in the $C(t)$ was observed. After 30 °C, with further increase of temperature, the solvation correlation decay function becomes faster as elaborated in Figure 4.7b. The corresponding solvation correlation decay constants at various temperatures are tabulated in Table 4.2. Inset of Figure 4.7c represents the Arrhenius plot of activation energy barrier model. The slope of the plot of $\ln\left(\frac{1}{\tau_{solv}}\right)$ vs $\frac{1}{T}$ yields a value of activation energy of 1.70 ± 0.2 kcal mol⁻¹. The result indicates that acrylodan is located in the hydration shell at the interior of the RMs and solvation relaxation of AC essentially involves the transition between interfacially bound waters to quasibound state [20]. Insignificant change of $C(t)$ in the temperature region of 10-30 °C indicates the increase in temperature does not perturb the relaxation dynamics of water molecules inside the RMs in the temperature range.

Figure 4.8a represents anisotropy decay plot of acrylodan in RMs at lower (10 °C) and elevated temperature (70 °C). The anisotropy experiments elucidate the rigidity of the probe molecules within RMs, and hence the water dynamics. At lower temperature (10 °C), the anisotropy consists of two decay components (22 ns (67%) and 0.67ns (33%)). The slower 22 ns time component is due to the global motion of the RMs which is well corroborated with the estimated value using SED equation [35] considering the hydrodynamic radius of RMs (3.5 nm) for $w_0=5$ as reported in the literature [31]. At 70 °C, the anisotropy decay constant becomes 12 ns (61%) and 0.23 ns (39%). The corresponding time constants for the anisotropy decays are summarized in Table 4.3. Figure 4.8b represents the change of diffusion coefficient for wobbling motion (D_W) value with increasing temperature. The diffusion coefficient (D_W) values are of the same order of magnitude as reported in one of our earlier work [31] for coumarin-500 in AOT RMs and increases with

increasing temperatures. The corresponding semicone angles (θ_w) experienced by the probe in different thermal regions are tabulated in Table 4.3. The observation is consistent with higher lability of the probe AC in the RMs at elevated temperature. Figure 4.8c represents the plot of microviscosity, experienced by the probe at different temperatures. The energy barrier (E_η) for the viscous flow was estimated from the slope of the plot of $\ln(\eta_m)$ against $\frac{1}{T}$ as described in equation (2.41). A good linear fit is obtained with a calculated E_η value of 2.05 ± 0.2 kcal mol⁻¹. Reasonably good agreement between the energy barrier values (E_η obtained from the rotational anisotropy study and E_a value obtained from solvation dynamics study) is found.

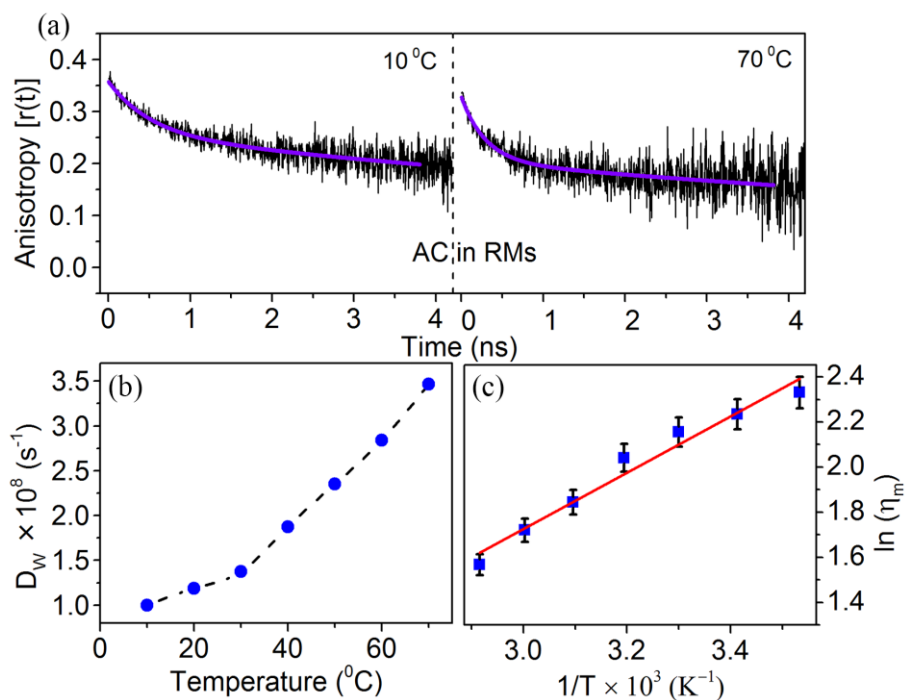


Figure 4.8. (a) Temporal decays of rotational anisotropy of acrylodan in RMs at 10 °C and 70 °C are shown. (b) Diffusion coefficient for wobbling motion (D_w) of AC in AOT RMs at different temperatures. Dotted line is guide to eye. (c) Plot of $\ln(\eta_m)$, η_m expressed in cP, against $1/T$ of AC in AOT RMs with a linear fit (5% error bar included).

4.3. Conclusion: In summary, we have carried out detail investigation of an important fluorescent probe acrylodan in biological and biomimetic cavities. The study provides some new insights about the cavity water dynamics for both biological and biomimetic systems. The estimated activation energy for water transition for both biological (ESA) and biomimetic (RMs) cavities using Arrhenius type activation energy model is similar and essentially indicates the water transition from bound to quasibound state. The rigidity of water molecules around Cys 34 of the protein cleft might have significant role in protein stability as well as crucial functional role in the ligand binding including an important anticancer drug doxorubicin. The persistency of the structural flexibility of the protein in the physiologically relevant temperature range (30-60 °C) as revealed from FRET and anisotropy studies is well justified from the perspective of protein activity. The considerable similarity of the dynamical properties of the water molecules in the protein cavity with that in the nano-droplets in the RMs is clearly revealed from our experiment. From the FRET studies, we have also observed a very narrow donor-acceptor distance distribution in the protein and RMs. The observation is important as a mammoth of theoretical (MD simulation in particular) and experimental understanding on the biomimetic RM-cavity is evident in the literature. Our experimental study is expected to have deep impact in the understanding of water relaxation/activity in hydrophobic cavity of protein interiors.

References

1. D. Chandler, Interfaces and the driving force of hydrophobic assembly. *Nature*, **437** (2005) 640.
2. S. Matysiak, P.G. Debenedetti and P.J. Rossky, Role of hydrophobic hydration in protein stability: A 3d water-explicit protein model exhibiting cold and heat denaturation. *J. Phys. Chem. B*, **116** (2012) 8095.
3. S. Somani, C.P. Chng and C.S. Verma, Hydration of a hydrophobic cavity and its functional role: A simulation study of human interleukin-1 beta. *Proteins*, **67** (2007) 868.
4. Y. Levy and J.N. Onuchic, Water mediation in protein folding and molecular recognition. *Annu. Rev. Biophys. Biomol. Struct.*, **35** (2006) 389.
5. N. Giovambattista, C.F. Lopez, P.J. Rossky and P.G. Debenedetti, Hydrophobicity of protein surfaces: Separating geometry from chemistry. *Proc. Natl. Acad. Sci. USA*, **105** (2008) 2274.
6. P. Rydberg, T.H. Rod, L. Olsen and U. Ryde, Dynamics of water molecules in the active-site cavity of human cytochromes P450. *J. Phys. Chem. B*, **111** (2007) 5445.
7. B. Yu, M. Blaber, A.M. Gronenborn, G.M. Clore and D.L.D. Caspar, Disordered water within a hydrophobic protein cavity visualized by X-ray crystallography. *Proc. Natl. Acad. Sci. USA*, **96** (1999) 103.
8. C. Carey, Y.-K. Cheng and P.J. Rossky, Hydration structure of the α -chymotrypsin substrate binding pocket: The impact of constrained geometry. *Chem. Phys.*, **258** (2000) 415.
9. J.C. Rasaiah, S. Garde and G. Hummer, Water in nonpolar confinement: From nanotubes to proteins and beyond. *Annu. Rev. Phys. Chem.*, **59** (2008) 713.
10. F. Kratz, A. Warnecke, K. Scheuermann, C. Stockmar, J. Schwab, P. Lazar, P. Druckes, N. Esser, J. Dreves, D. Rognan, C. Bissantz, C. Hinderling, G.

- Folkers, I. Fichtner and C. Unger, Probing the cysteine-34 position of endogenous serum albumin with thiol-binding doxorubicin derivatives. Improved efficacy of an acid-sensitive doxorubicin derivative with specific albumin-binding properties compared to that of the parent compound. *J. Med. Chem.*, **45** (2002) 5523.
11. J.K.A. Kamal, L. Zhao and A.H. Zewail, Ultrafast hydration dynamics in protein unfolding: Human serum albumin. *Proc. Natl. Acad. Sci. USA*, **101** (2004) 13411.
 12. S.K. Pal and A.H. Zewail, Dynamics of water in biological recognition. *Chem. Rev.*, **104** (2004) 2099.
 13. A.J. Ryan, J. Ghuman, P.A. Zunszain, C.-w. Chung and S. Curry, Structural basis of binding of fluorescent, site-specific dansylated amino acids to human serum albumin. *J. Struct. Biol.*, **174** (2011) 84.
 14. R.K. Mitra, S.S. Sinha and S.K. Pal, Hydration in protein folding: Thermal unfolding/refolding of human serum albumin. *Langmuir*, **23** (2007) 10224.
 15. K. Flora, J.D. Brennan, G.A. Baker, M.A. Doody and F.V. Bright, Unfolding of acrylodan-labeled human serum albumin probed by steady-state and time-resolved fluorescence methods. *Biophys. J.*, **75** (1998) 1084.
 16. K. Bhattacharyya, Solvation dynamics and proton transfer in supramolecular assemblies. *Acc. Chem. Res.*, **36** (2002) 95.
 17. R. Saha, S. Rakshit, R.K. Mitra and S.K. Pal, Microstructure, morphology, and ultrafast dynamics of a novel edible microemulsion. *Langmuir*, **28** (2012) 8309.
 18. D. Pant and N.E. Levinger, Polar solvation dynamics in nonionic reverse micelles and model polymer solutions. *Langmuir*, **16** (2000) 10123.
 19. S. Pal, S. Balasubramanian and B. Bagchi, Temperature dependence of water dynamics at an aqueous micellar surface: Atomistic molecular dynamics simulation studies of a complex system. *J. Chem. Phys.*, **117** (2002) 2852.

20. S. Balasubramanian, S. Pal and B. Bagchi, Hydrogen-bond dynamics near a micellar surface: Origin of the universal slow relaxation at complex aqueous interfaces. *Phys. Rev. Lett.*, **89** (2002) 115505.
21. S. Batabyal, T. Mondol and S.K. Pal, Picosecond-resolved solvent reorganization and energy transfer in biological and model cavities. *Biochimie*, **95** (2013) 1127.
22. G. Weber and F.J. Farris, Synthesis and spectral properties of a hydrophobic fluorescent probe: 6-propionyl-2-(dimethylamino)naphthalene. *Biochemistry*, **18** (1979) 3075.
23. J. González-Jiménez and M. Cortijo, Resonance energy transfer between tryptophan-214 in human serum albumin and acrylodan, prodan, and promen. *Protein J.*, **23** (2004) 351.
24. M.A. Tricerri, A.K. Behling Agree, S.A. Sanchez and A. Jonas, Characterization of apolipoprotein A-I structure using a cysteine-specific fluorescence probe. *Biochemistry*, **39** (2000) 14682.
25. N. Nandi and B. Bagchi, Dielectric relaxation of biological water. *J. Phys. Chem. B*, **101** (1997) 10954.
26. R.K. Mitra, S.S. Sinha and S.K. Pal, Temperature-dependent hydration at micellar surface: Activation energy barrier crossing model revisited. *J. Phys. Chem. B*, **111** (2007) 7577.
27. S. Pal, S. Balasubramanian and B. Bagchi, Identity, energy, and environment of interfacial water molecules in a micellar solution. *J. Phys. Chem. B*, **107** (2003) 5194.
28. P. Sen, S. Mukherjee, A. Halder and K. Bhattacharyya, Temperature dependence of solvation dynamics in a micelle. 4-Aminophthalimide in triton X-100. *Chem. Phys. Lett.*, **385** (2004) 357.
29. R.K. Mitra, S.S. Sinha and S.K. Pal, Hydration in protein folding: Thermal unfolding/refolding of human serum albumin. *Langmuir*, **23** (2007) 10224.

30. K. Kinosita Jr, A. Ikegami and S. Kawato, On the wobbling-in-cone analysis of fluorescence anisotropy decay. *Biophys. J.*, **37** (1982) 461.
31. R.K. Mitra, S.S. Sinha and S.K. Pal, Temperature-dependent solvation dynamics of water in sodium bis(2-ethylhexyl)sulfosuccinate/isooctane reverse micelles. *Langmuir*, **24** (2007) 49.
32. R. Zana, Microviscosity of aqueous surfactant micelles: Effect of various parameters. *J. Phys. Chem. B*, **103** (1999) 9117.
33. S.K. Pal, J. Peon and A.H. Zewail, Biological water at the protein surface: Dynamical solvation probed directly with femtosecond resolution. *Proc. Natl. Acad. Sci. USA*, **99** (2002) 1763.
34. S. Batabyal, T. Mondol, K. Das and S.K. Pal, Förster resonance energy transfer in a nanoscopic system on a dielectric interface. *Nanotechnology*, **23** (2012) 495402.
35. D. Lavalette, C. Tetreau, M. Tourbez and Y. Blouquit, Microscopic viscosity and rotational diffusion of proteins in a macromolecular environment. *Biophys. J.*, **76** (1999) 2744.

Chapter 5

Spectroscopic studies on the interfacial dynamics at a specific protein-DNA interface

5.1. Introduction: Interaction of regulatory DNA binding protein with their target sites is responsible for the regulation of key biological functions such as gene expression [1], DNA repair and recombination [2], signal transduction [2, 3] etc. The functional perspective of a protein-DNA complex is critically dictated by the static and dynamic aspects of the conformation of protein and DNA in complex. Specific protein-DNA interaction [4] is governed by sequence recognition (base readout) through direct contacts between protein's amino acid side chains and DNA bases [5], as well as the spatial geometry of the two biomolecules (shape readout) [5]. Nonspecific protein-DNA interaction [2, 6] however is governed by purely electrostatic forces [7] of interaction between the negatively charged DNA and the protein, and does not have sequence dependence. In contemporary literature, there are ample examples of studies dealing with such specific/nonspecific protein-DNA interaction enlightening the driving force for the interactions, role of solvent molecules, and the involved thermodynamics [8-12]. In protein-DNA complex formation, proteins interact with both major and minor grooves of DNA, *via* hydrogen bonding and hydrophobic interactions as well as water mediated interactions [13]. Most structural and functional studies on different specific protein-DNA complexes reveal the existence of water molecules at the interaction interface [14]. The important contribution of these interfacial water molecules to the stability and specificity of protein-DNA interactions has been recognized through a combination of high-resolution structural and allied computational studies [15-17]. Several such studies indicate towards different roles of water molecules that act as a screen to

neutralize like charges on proteins and DNA, enabling formation of water mediated hydrogen bonds. However, these structural (mainly crystallography and NMR) and theoretical studies do not cover the aspects of the dynamics of water molecules bound to the DNA in the complex [18, 19].

In this context, we have exploited the unique opportunity to study a model protein-DNA complex comprising of lambda repressor (λ -repressor) protein and the two operator DNA sites, O_{R1} and O_{R2} (described in chapter 3). Structurally λ -repressor is a two-domain protein, the N-terminal domain interacts with the operator DNA, while C-terminal domain is responsible for most protein-protein interactions, and these interactions are essential for the cooperative binding and for the functioning of the genetic switch [20]. These target operator DNA sites are 17 base pairs pseudo-palindromic sites bearing close similarity with each other [21]. The repressor protein interacts with different operator DNA with differing specificity [20, 22-24]. The exploration of the dynamical role of minor groove water molecules in specific protein DNA interaction is the main motive of the study. Though various structural studies demonstrated the presence and importance of water molecules in the specific protein DNA interface, the dynamical time scales at the interface are very sparse in the literature. The change of DNA backbone flexibility in the protein-DNA complex was also explored. In order to unravel the role of minor groove water dynamics and DNA side chain motion in the specific protein-DNA interaction, a well-known fluorescent probe, Hoechst 33258 (H258) was used. The cationic nature and minor groove matching concaveness allow H258 to interact with the DNA minor grooves through van der Waals force and hydrogen bonding [25]. Earlier femtosecond resolved solvation studies on H258 bound to DNA minor groove revealed sub-100 ps water relaxation time [19]. On the other hand, long time component (\sim ns) is reported to be associated to the DNA backbone flexibility [26]. In the current context, picosecond-resolved solvation dynamics study of H258 provides a unique opportunity to explore both minor groove water relaxation (ps time scale) and the DNA side chain flexibility (ns time

scale). The physical characterization of the binding nature of the probe and the conformation of the DNA structure before and after interaction with protein was elucidated with the help of steady-state/time-resolved fluorescence spectroscopy, circular dichroism, and time-resolved fluorescence anisotropy studies. Detailed Förster resonance energy transfer (FRET) analysis was carried out in order to investigate the conformational perturbation of the DNA in the complex. Picosecond-resolved lifetime traces of H258 were analyzed to estimate the dynamical behavior of water molecules present in the DNA minor grooves and the flexibility of the DNA side chain. The stability of minor groove water molecules and the dynamical exchange of such water molecules with the bulk water molecules were further investigated through temperature dependent solvation studies in the protein-DNA complex.

5.2. Results and discussion:

5.2.1. Ultrafast interfascial solvation dynamics in specific protein DNA recognition [27]: Figure 5.1a,b show emission spectra of H258 bound to different operators DNA in presence and absence of λ -repressor. In presence of O_R1 and O_R2 DNA, the emission maximum of H258 (buffer: 500 nm) is significantly blue shifted (O_R1 DNA: 457 nm, O_R2 DNA: 460 nm) due to the interaction of H258 with DNA. Upon addition of λ -repressor to the H258, bound to operator DNA, the emission spectrum is further blue shifted especially in H258-O_R2- λ complex as shown in Figure 5.1b. From the steady-state experiments, it is evident that upon repressor binding, the local environment around H258 in O_R2 DNA (Figure 5.1b) is influenced to a greater extent in comparison to O_R1 DNA (Figure 5.1a). To rule out the possibility of any specific interaction between H258 and λ -repressor leading to such spectral change, a set of control time-resolved experiments were carried out. From the fluorescence lifetime transients (Figure 5.1c), it is evident that the nonspecific binding of H258 with repressor is insignificant as the lifetime of H258 is minimally perturbed in presence of repressor. Time-resolved

fluorescence anisotropy analysis (Figure 5.1d) further supports the observation as the rotational time constant (τ_{rot}) of H258 in absence and in presence of λ -repressor remains unaltered ($\tau_{\text{rot}}=0.55$ ns). The anisotropy decay constant of ~ 0.55 ns, indicates the free rotational motion of the probe in solution [28].

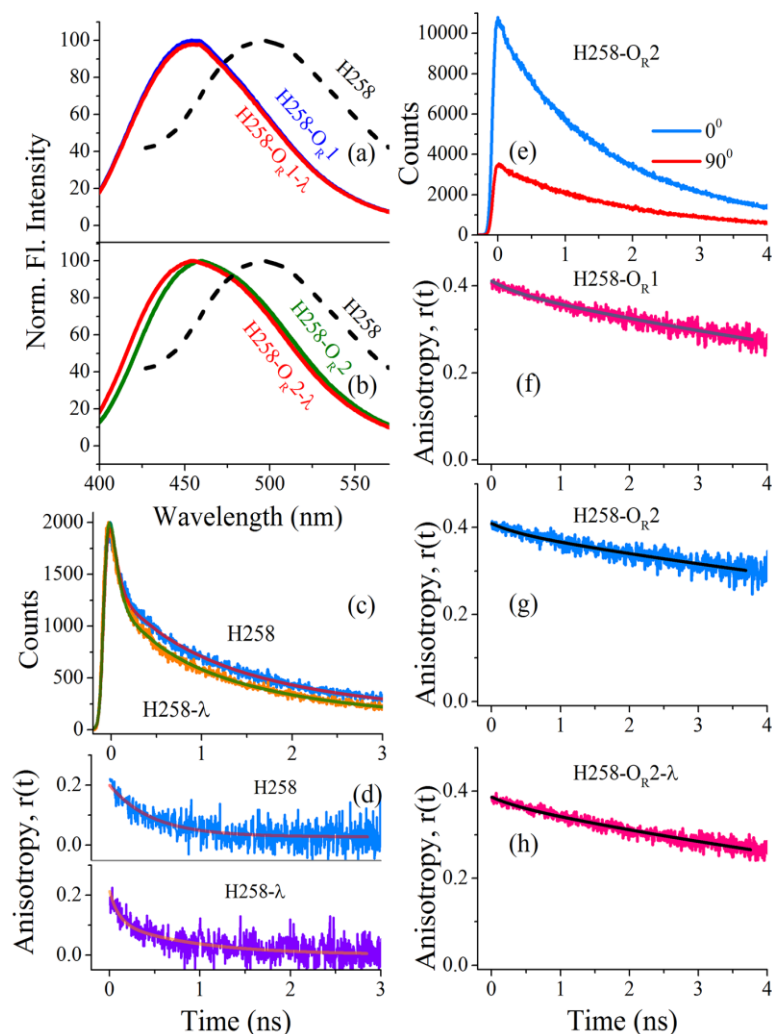


Figure 5.1. Normalized steady-state fluorescence spectra of probe H258 in three different environments: (a) in buffer, O_R1 DNA and O_R1-repressor complex, (b) in buffer, O_R2 DNA and O_R2-repressor complex. (c) Picosecond-resolved fluorescence transients of H258 are shown in presence and absence of λ -repressor protein. For comparison, the fluorescence transient of H258 in buffer solution is also included. (d) Time-resolved fluorescence anisotropies, $r(t)$, of the probe in water (buffer) and in presence λ -repressor protein at emission wavelength of 500 nm are shown. (e) Representative time-resolved traces of H258 in O_R2 at different polarization (0° and 90°) are shown. Time-resolved fluorescence anisotropies of H258 in O_R1 (f) and O_R2 (g) are depicted. (h) Represents the anisotropy decay of H258 in O_R2-protein complex.

The fluorescence anisotropy decays of H258 in presence of O_{R1} and O_{R2} DNA are presented in Figure 5.1f and Figure 5.1g respectively. The representative time-resolved fluorescence intensity decays at different polarization (0° and 90°) for H258-O_{R2} complex are presented in Figure 5.1e. The bi-exponential anisotropy decay of H258 in O_{R1} and O_{R2} are quite similar. In case of O_{R1}, the rotational decay consists of 0.4 ns and 10 ns decay components, whereas, in case of O_{R2}, the rotational decay consists of 0.4 ns and 14 ns decay components. The details of anisotropy data are provided in Table 5.1. It has to be noted that the fluorescence anisotropy decays were collected at the corresponding emission maxima of the concerned systems. In DNA-protein complex, the anisotropy decay pattern of H258 remains unaltered, suggesting the location of the probe in the DNA does not change even after the complex formation. The representative anisotropy decay of H258 in protein-DNA complex is shown in Figure 5.1h.

The steady-state fluorescence measurements and time-resolved fluorescence anisotropy decays reveal the binding nature of H258 to the operator DNA in absence and presence of repressor. In order to investigate conformational and structural changes of the operator DNA, upon interaction with λ -repressor, circular dichroism (CD) spectroscopy was used. Figure 5.2 represents the CD spectra of operator DNA, O_{R1} and O_{R2} in absence and in presence of λ -repressor. In case of O_{R2} (Figure 5.2b), careful observation reveals a shift of the spectral maximum (270 nm) along with the increase in ellipticity upon complexation with λ -repressor. In case of O_{R1} DNA (Figure 5.2a), negligible spectral shift and smaller change in ellipticity was observed in comparison to O_{R2}. The observation indicates the conformational change of O_{R2} after binding to the repressor is significant compared to that of O_{R1}. The inset of Figure 5.2a represents the CD spectrum of unbound λ -repressor, indicating no possible interference of CD signal at 270 nm wavelength. The characteristic wavelength shift in the CD spectra of operator DNA (O_{R2}) upon repressor binding is consistent with the reported protein induced bending of DNA [29].

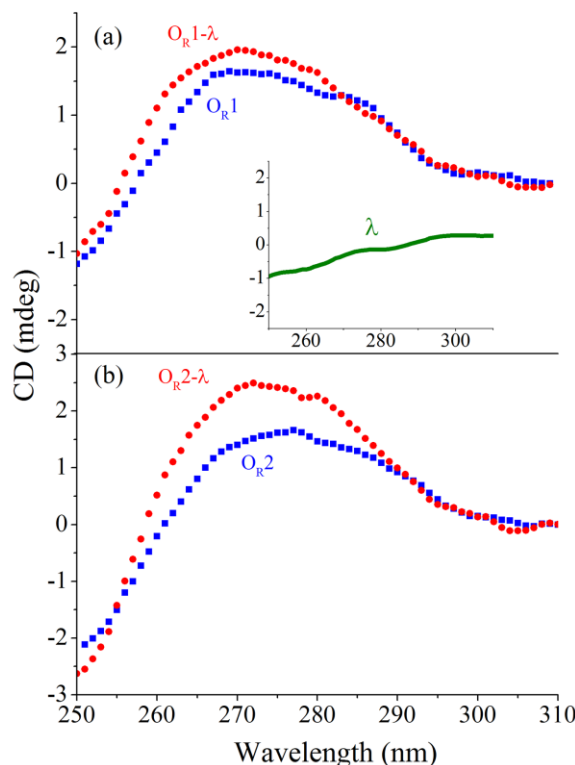


Figure 5.2. (a) Ellipticity (mdeg) of O_{R1} DNA in presence and in absence of λ -repressor protein. The inset figure represents the CD spectrum of λ -repressor protein. (b) Depicts the optical rotation (mdeg) of O_{R2} DNA in presence and in absence of λ -repressor protein. Upon complexation with protein, the characteristic peak of DNA around 270 nm is blue shifted. No significant wavelength shift was observed in case of O_{R1} .

To further investigate the structural aspects of DNA and its change upon protein binding, Förster resonance energy transfer (FRET) study from DNA bound H258 to ethidium moieties intercalated into DNA was carried out. Steady-state emission quenching of DNA bound H258 in presence of EtBr is evident in Figure 5.3a. In an earlier study, it was observed that H258 and EtBr can bind simultaneously to DNA, without displacing each other [30]. In that study, it was also demonstrated that H258 and EtBr serve as an excellent FRET pair, where H258 is an energy donor and EtBr is an energy acceptor. The time-resolved fluorescence transients are represented in Figure 5.3b. As evident, from Figure 5.3b (lower panel), upon addition of repressor to O_{R2} , the efficiency of energy transfer from H258 to EtBr decreases (72% to 59%), whereas in case of O_{R1} (upper

panel), the efficiency remains unaltered (57%). The FRET study clearly demonstrates that O_R2 DNA undergoes significant conformation change upon protein binding, leading to the decrease in energy transfer efficiency. From the calculated R_0 value (3.81 nm) and measured FRET efficiency, the donor (H258)-acceptor (EtBr) distance in O_R1 and O_R2 was estimated as 3.58 nm and 3.25 nm respectively.

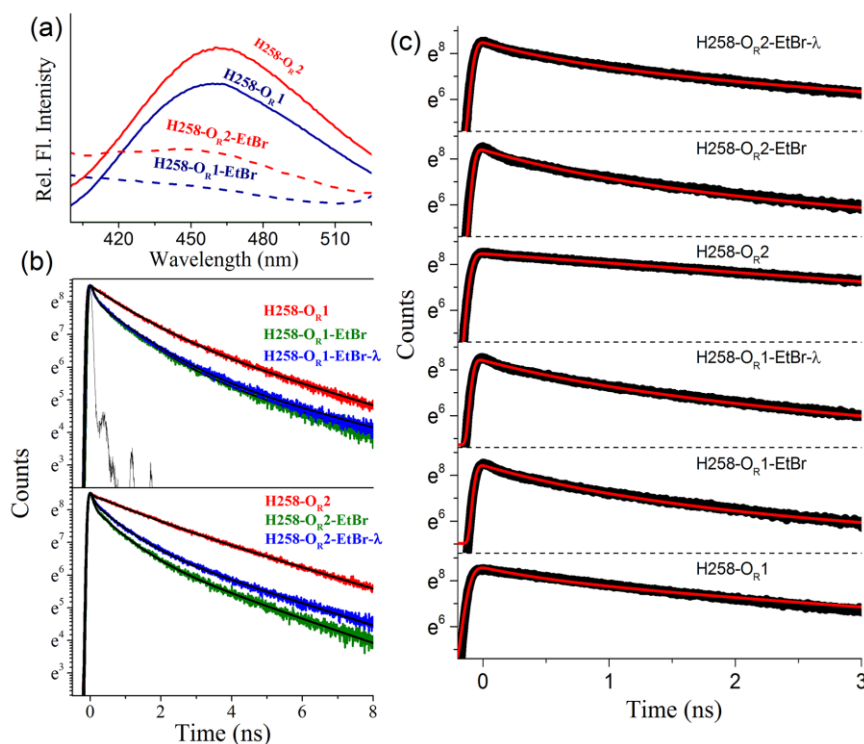


Figure 5.3. (a) Steady-state emission spectra of H258 in operator DNA in presence and in absence of EtBr. (b) The fluorescence lifetime quenching of H258. Upper panel shows the effect of EtBr in O_R1 system and the lower panel depicts the energy transfer for O_R2 system. (c) Fitting of time-resolved lifetime data of H258 under various conditions by Tachiya kinetic model.

Upon addition of λ -repressor, the donor-acceptor distance in O_R2 -repressor complex reveals value of 3.6 nm. In this context, we have applied a kinetic model developed by Tachiya [31] for the quenching of luminescent probes undergoing nonradiative energy transfer in restricted environments. In contemporary literature, the kinetic model finds its relevance in various aspects including drug binding [32], nanoparticles quenching [33]. The model provides a clear

understanding about the number of possible binding sites of the host molecules. In our case, the host being the DNA strand itself, where EtBr intercalates.

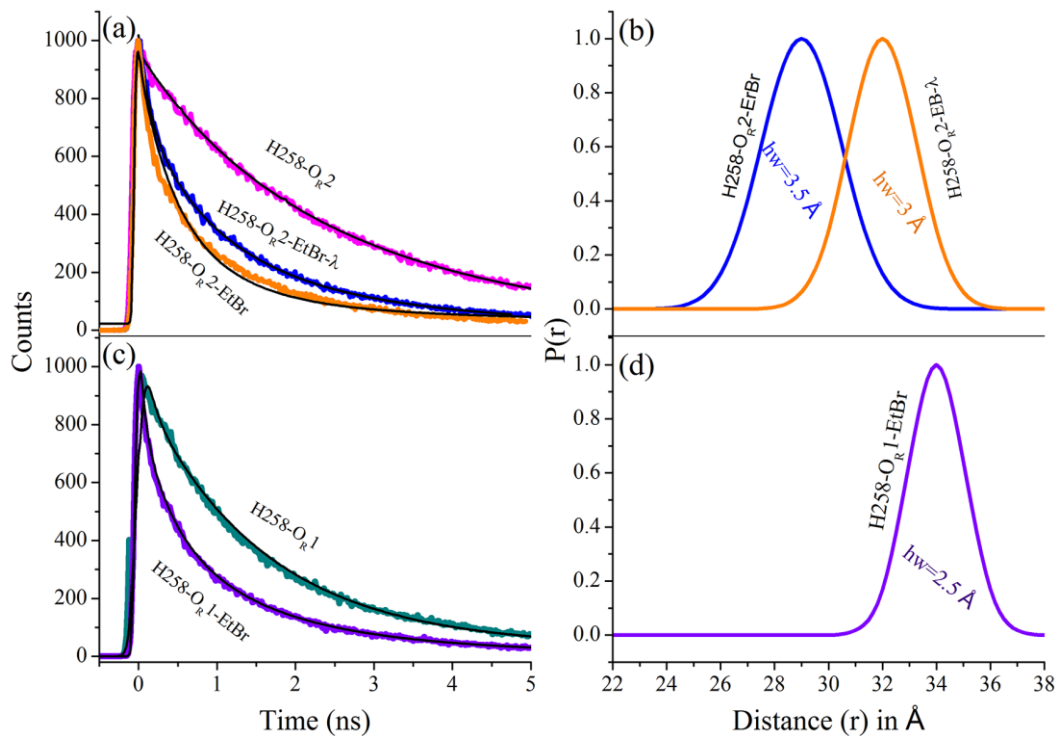


Figure 5.4. (a) and (c) Depict the fitting of time-resolved lifetime traces considering the distance distribution between donor and acceptor in O_R2 and O_R1 system respectively. (b) and (d) Show the corresponding probability of distance distribution ($P(r)$) with respect to mean donor-acceptor distance.

For O_R1 DNA (Figure 5.3c), the mean number (m) of intercalated ethidium moiety present per DNA was estimated to be ~ 5 and the quenching rate constant (kq) was estimated 0.9 ns^{-1} . The m and kq values remain unchanged in DNA-protein complex. In case of O_R2 (Figure 5.3c), the mean number of acceptor (ethidium) per DNA was estimated to be ~ 6 and the quenching constant was 1.4 ns^{-1} . Upon addition of repressor, the quenching rate constant for O_R2 decreases to a value of 1.1 ns^{-1} . The change in orientation factor between donor and acceptor dipoles could also contribute to the decrease in the energy transfer. The distance distribution (hw) changes from 3.5 Å ($H258-O_R2-EtBr$) to 3 Å ($H258-O_R2-EtBr-\lambda$). In

case of O_R1, the distance distribution between H258 and EtBr does not change in presence of protein (Figure 5.4).

At this juncture, it is important to know the local dynamics of water molecules, which actively take part in various biological functions including the recognition process as well as in maintaining the biological activity [23]. As revealed by the various structural studies, H258 remains attached to the both repressor bound and unbound operator DNA and hence can report their environmental dynamics. In order to study the interfacial water dynamics at DNA-protein interface and the relaxation dynamics of water molecules around two different operators DNA, time-resolved fluorescence experiments were carried out. Figure 5.5a displays the fluorescence transients (blue to red end) of H258 in O_R1 DNA, in absence and in presence of λ -repressor. Figure 5.5b shows the constructed time-resolved emission spectrum (TRES) of H258 giving a shift of 1300 cm⁻¹ and 1450 cm⁻¹ in a 10 ns time window for O_R1 and O_R1-repressor complex respectively, which indicates that H258 in the excited state is stabilized due to the solvation by the minor groove water molecules along with the DNA itself. However, the change in the net spectral shift of H258 for O_R1 and O_R1-repressor complex is insignificant. The corresponding solvation correlation decay profiles are presented in the inset figure. The solvation correlation decay profile of H258 in O_R1, consists decay time constants of 50 ps (35%) and 7 ns (65%). One of the previous femtosecond-resolved studies on the DNA minor groove water dynamics reveals the hydration time scale of 1.4 ps and 20 ps [19]. However, in the limited time resolution (picosecond-resolved), the observed 50 ps component in the solvation decay profile is consistent with the sub-100-ps relaxation of minor groove water molecules [34]. The major decay component of ~10 ns is related to the relaxation of the DNA structure itself [34]. The observed solvation decay constants of H258 are consistent with our earlier studies [35]. Strikingly, the constructed solvation correlation decay for H258 in DNA-protein complex does

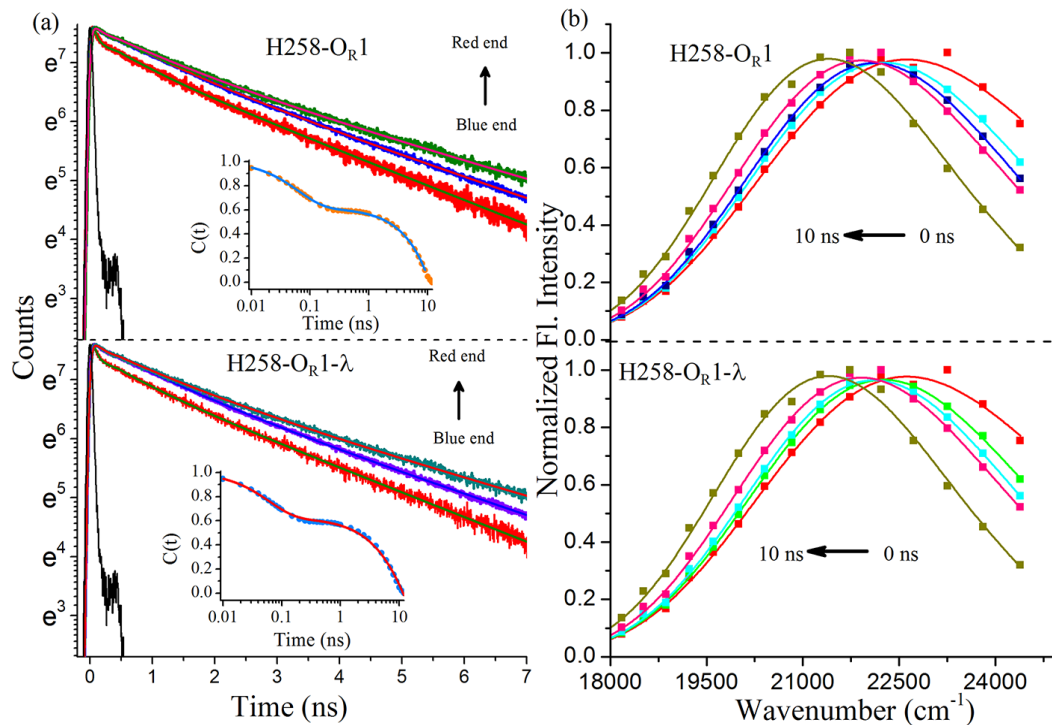


Figure 5.5. (a) Picosecond-resolved fluorescence transients of H258 at three wavelengths in O_R1 DNA and O_R1 -repressor complex respectively are shown. The excitation wavelength was 375 nm. Solid lines indicate exponential numerical fitting of the experimental data points. The insets depict the solvation correlation decay profiles of H258 in O_R1 in absence and in presence of lambda repressor. (b) Time-resolved emission spectrum (TRES) of H258 in O_R1 and O_R1 - λ repressor complex are shown respectively. The lifetime plots are in semi-log format to better visualize the change of the lifetime traces at different wavelengths.

not change significantly as shown in Figure 5.5a (50 ps (30%) and 7 ns (70%)). Figure 5.6a displays the fluorescence transients of H258 from blue to red end, i.e. 410 nm, 470 nm, and 530 nm in O_R2 and O_R2 -repressor complex. At the blue edge shift for both DNA and DNA-protein complex is consistent with similar solvation correlation decay profile. Negligible change in the faster time scale of the solvation decay profile is observed suggesting less perturbed water dynamics in the minor groove of DNA (O_R1/O_R2) in presence of lambda repressor protein.

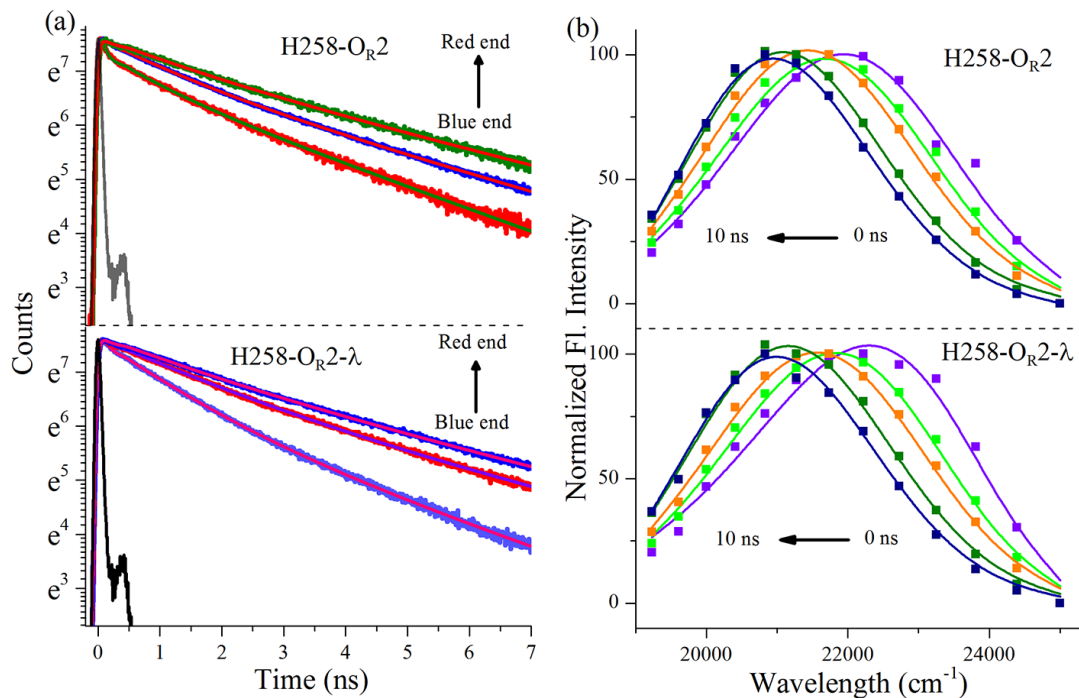


Figure 5.6. (a) Picosecond-resolved fluorescence transients of H258 at three wavelengths in OR₂ DNA and OR₂-repressor complex are shown respectively. The excitation wavelength was 375 nm. Solid lines indicate exponential numerical fitting of the experimental data points. (b) Time-resolved emission spectrum of H258 in OR₂ and OR₂-repressor complex are shown respectively. The lifetime plots are in semi-log format to better visualize the change of the lifetime traces at different

In case of OR₂, the DNA side chain flexibility is slightly hindered as reflected in the slower decay component (9 ns changes to 11 ns). However, in case of OR₁, upon repressor binding, side chain flexibility remains unchanged as reflected in the H258 solvation decay profile. Upon repressor binding, the slight change in the slower decay component of H258 solvation decay profile in case of OR₂, could be attributed to the observed conformational change of its structure upon protein binding. In this context, we also attempted to understand whether exchange of minor groove water with the bulk water decreases due to the formation of stable interface in DNA-protein complex. In order to address exchange of minor groove water with the bulk water, we have carried out the temperature dependent TRES analysis of H258 in OR₂ DNA in absence and presence of repressor. Figure 5.7a shows the temporal decay of the solvation correlation function ($C(t)$) for the

probe (H258) bound to O_R2 at various temperatures. At lower temperature (7 °C), the solvation correlation function decays with a time constant of 40 ps (40%) and 9 ns (60%). With increase in temperature, the contribution of faster solvation decay time gradually decreases and the overall solvation becomes slower.

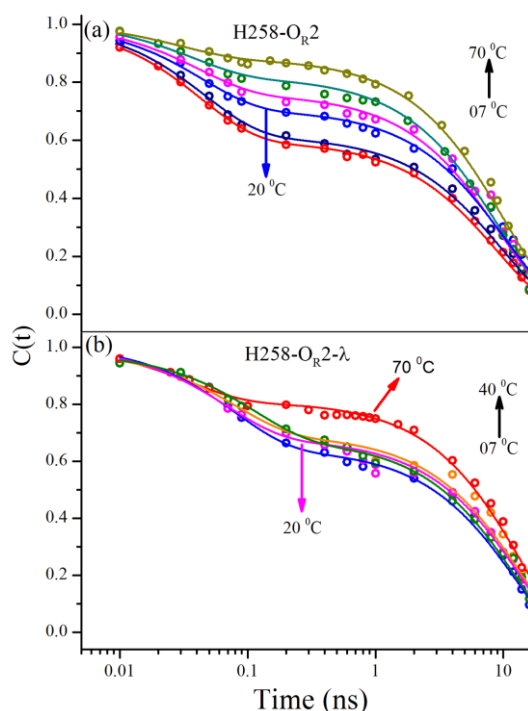


Figure 5.7. Temporal decay of the solvation correlation function ($C(t)$) at different temperatures for the H258 in (a) O_R2 and in (b) O_R2-repressor complex. The time has been plotted on a logarithmic scale. Solid lines indicate exponential fitting of the experimental data points.

At 40 °C, the temporal decay of the solvation correlation function shows time constants of 40 ps (20%) and 9 ns (80%). On the contrary, for O_R2-repressor complex, the temperature dependent hydration dynamics follows a different course (Figure 5.7b). The solvation correlation profile decays with a time constant of 100 ps (30%) and 12.3 ns (70%) at lower temperature (7 °C). In the temperature region of 7-40 °C, the water dynamics in repressor-operator interface is minimally affected as reflected in the solvation correlation decays (Figure 5.7b). With further increment of temperature, >50 °C, the water dynamics around H258 changes significantly possibly due to the melting of DNA strand itself. The temperature

dependent solvation studies unearth the exchangeability of minor groove water molecules with the bulk water molecules. In the free operator DNA, the exchangeability of minor groove changes with increase in temperature as reflected in the faster solvation decay time. However, due to the formation of a stable interface in the DNA-protein complex, the water molecules in the minor groove are conserved and less susceptible to the temperature changes.

Table 5.1. Biexponential anisotropy decay fitting of H258 in operator DNA and protein-DNA complex.

System	τ_1 (ns) %	τ_2 (ns) %	τ_{rot} (ns)
H258-O _{R1}	0.44 (5%)	10 (95%)	9.53
H258-O _{R1} - λ	0.41 (5%)	10 (95%)	9.52
H258-O _{R2}	0.43 (4%)	14 (96%)	13.45
H258-O _{R2} - λ	0.43 (4%)	14 (96%)	13.45

5.3. Conclusion: In summary, the study characterizes the conformational change of the DNA, the dynamics of DNA minor groove water molecules and DNA side chain flexibility in a specific DNA protein interaction between λ -repressor and two operators DNA (O_{R1} and O_{R2}). In specific DNA-protein interaction, the recognition process does not only involve the charge and shape complementarities, but also rely upon the dynamics of interfacial water molecules. The crucial observation indicates the preservation of minor groove water molecules due to formation of stable DNA-protein complex. The dynamics of these DNA minor groove water molecules and the flexibility of DNA side chain is minimally affected upon interaction with the protein as revealed by the excited state relaxation of minor groove binder H258. It has to be noted that, upon protein binding, the slight change in solvent relaxation decay profile of H258 in O_{R2} is consistent with the structural modification of the DNA as evidenced from CD study and FRET analysis. The experimental observation is expected to contribute towards understanding the role of minor groove water relaxation and DNA side chain flexibility in DNA-protein complex formation.

References

1. G. Orphanides and D. Reinberg, A unified theory of gene expression. *Cell*, **108** (2002) 439.
2. C.G. Kalodimos, N. Biris, A.M.J.J. Bonvin, M.M. Levandoski, M. Guennuegues, R. Boelens and R. Kaptein, Structure and flexibility adaptation in nonspecific and specific protein-DNA complexes. *Science*, **305** (2004) 386.
3. C. Muller, P. Calsou, P. Frit and B. Salles, Regulation of the DNA-dependent protein kinase (DNA-PK) activity in eukaryotic cells. *Biochimie*, **81** (1999) 117.
4. A.H. Koop, S.I. Staprans and S. Bourgeois, Specific binding of the cAMP receptor protein of Escherichia coli to the lactose operon promoter. *Biochimie*, **67** (1985) 161.
5. R. Rohs, X.S. Jin, S.M. West, R. Joshi, B. Honig and R.S. Mann, Origins of specificity in protein-DNA recognition. *Annu. Rev. Biochem.*, **79** (2010) 233.
6. H.X. Zhou, Rapid search for specific sites on DNA through conformational switch of nonspecifically bound proteins. *Proc. Natl. Acad. Sci. USA*, **108** (2011) 8651.
7. Y. Kao-Huang, A. Revzin, A.P. Butler, P. O'Conner, D.W. Noble and P.H. Von Hippel, Nonspecific DNA binding of genome-regulating proteins as a biological control mechanism: Measurement of DNA-bound Escherichia coli lac repressor in vivo. *Proc. Natl. Acad. Sci. USA*, **74** (1977) 4228.
8. D. Zhong, S.K. Pal and A.H. Zewail, Femtosecond studies of protein-DNA binding and dynamics: Histone I. *ChemPhysChem*, **2** (2001) 219.
9. R. Sarkar and S.K. Pal, Interaction of hoechst 33258 and ethidium with histone1-DNA condensates. *Biomacromolecules*, **8** (2007) 3332.
10. C.K. Reddy, A. Das and B. Jayaram, Do water molecules mediate protein-DNA recognition? *J. Mol. Biol.*, **314** (2001) 619.

11. R. Sarkar and S.K. Pal, Ligand-DNA interaction in a nanocage of reverse micelle. *Biopolymers*, **83** (2006) 675.
12. V. Ramakrishnan and R. Rajagopalan, Dynamics and thermodynamics of water around EcoRI bound to a minimally mutated DNA chain. *Phys. Chem. Chem. Phys.*, **14** (2012) 12277.
13. C.O. Pabo and R.T. Sauer, Protein-DNA recognition. *Annu. Rev. Biochem*, **53** (1984) 293.
14. N.Y. Sidorova and D.C. Rau, The dissociation rate of the EcoRI-DNA-specific complex is linked to water activity. *Biopolymers*, **53** (2000) 363.
15. S. Jones, P. van Heyningen, H.M. Berman and J.M. Thornton, Protein-DNA interactions: A structural analysis. *J. Mol. Biol.*, **287** (1999) 877.
16. Z. Otwinowski, R.W. Schevitz, R.G. Zhang, C.L. Lawson, A. Joachimiak, R.Q. Marmorstein, B.F. Luisi and P.B. Sigler, Crystal-structure of Trp repressor operator complex at atomic resolution. *Nature*, **335** (1988) 321.
17. B. Nguyen, S. Neidle and W.D. Wilson, A role for water molecules in DNA-ligand minor groove recognition. *Acc. Chem. Res.*, **42** (2009) 11.
18. S.K. Pal and A.H. Zewail, Dynamics of water in biological recognition. *Chem. Rev.*, **104** (2004) 2099.
19. S.K. Pal, L.A. Zhao and A.H. Zewail, Water at DNA surfaces: Ultrafast dynamics in minor groove recognition. *Proc. Natl. Acad. Sci. USA*, **100** (2003) 8113.
20. M. Ptashne and N. Hopkins, The operators controlled by the lambda phage repressor. *Proc. Natl. Acad. Sci. USA*, **60** (1968) 1282.
21. A.D. Johnson, B.J. Meyer and M. Ptashne, Interactions between DNA-bound repressors govern regulation by the λ phage repressor. *Proc. Natl. Acad. Sci. USA*, **76** (1979) 5061.
22. R.T. Sauer, K. Hehir, R.S. Stearman, M.A. Weiss, A. Jeitler-Nilsson, E.G. Suchanek and C.O. Pabo, An engineered intersubunit disulfide enhances

- the stability and DNA binding of the N-terminal domain of lambda repressor. *Biochemistry*, **25** (1986) 5992.
23. T. Mondol, S. Batabyal and S.K. Pal, Ultrafast electron transfer in the recognition of different DNA sequences by a DNA-binding protein with different dynamical conformations. *J. Biomol. Struct. Dyn.*, **30** (2012) 362.
 24. S. Deb, S. Bandyopadhyay and S. Roy, DNA sequence dependent and independent conformational changes in multipartite operator recognition by lambda-repressor. *Biochemistry*, **39** (2000) 3377.
 25. P.E. Pjura, K. Grzeskowiak and R.E. Dickerson, Binding of hoechst 33258 to the minor groove of B-DNA. *J. Mol. Biol.*, **197** (1987) 257.
 26. S. Sen, D. Andreatta, S.Y. Ponomarev, D.L. Beveridge and M.A. Berg, Dynamics of water and ions near DNA: Comparison of simulation to time-resolved stokes-shift experiments. *J. Am. Chem. Soc.*, **131** (2009) 1724.
 27. S. Batabyal, T. Mondol, S. Choudhury, A. Mazumder and S.K. Pal, Ultrafast interfacial solvation dynamics in specific protein DNA recognition. *Biochimie*, **95** (2013) 2168.
 28. T. Mondol, P. Rajdev, A. Makhal and S.K. Pal, Interaction of an antituberculosis drug with a nanoscopic macromolecular assembly: Temperature-dependent Förster resonance energy transfer studies on rifampicin in an anionic sodium dodecyl sulfate micelle. *J. Phys. Chem. B*, **115** (2011) 2924.
 29. Y. Lyubchenko, L. Shlyakhtenko, B. Chernov and R.E. Harrington, DNA bending induced by cro protein-binding as demonstrated by gel-electrophoresis. *Proc. Natl. Acad. Sci. USA*, **88** (1991) 5331.
 30. D. Banerjee and S.K. Pal, Simultaneous binding of minor groove binder and intercalator to dodecamer DNA: Importance of relative orientation of donor and acceptor in FRET. *J. Phys. Chem. B*, **111** (2007) 5047.
 31. M. Tachiya, Kinetics of quenching of luminescent probes in micellar systems. II. *J. Chem. Phys.*, **76** (1982) 340.

32. S. Banerjee, M. Tachiya and S.K. Pal, Caffeine-mediated detachment of mutagenic ethidium from various nanoscopic micelles: An ultrafast Förster resonance energy transfer Study. *J. Phys. Chem. B*, **116** (2012) 7841.
33. S. Sadhu, M. Tachiya and A. Patra, A stochastic model for energy transfer from CdS quantum dots/rods (donors) to Nile red dye (acceptors). *J. Phys. Chem. C*, **113** (2009) 19488.
34. E.B. Brauns, M.L. Madaras, R.S. Coleman, C.J. Murphy and M.A. Berg, Measurement of local DNA reorganization on the picosecond and nanosecond time scales. *J. Am. Chem. Soc.*, **121** (1999) 11644.
35. D. Banerjee and S.K. Pal, Direct observation of essential DNA dynamics: Melting and reformation of the DNA minor groove. *J. Phys. Chem. B*, **111** (2007) 10833.

Chapter 6

Development of an engineered platform for the detection of very fast molecular/biomolecular interaction

6.1. Introduction: Molecular recognition process refers to the weak non-covalent interaction, which takes place selectively and specifically between small ligand molecules with biological macromolecules. Understanding of such recognition in biological and biomimetic milieu is the central attraction for drug designing, which is crucial for the improvement of human healthcare. A thorough knowledge of the structural, dynamical and energetic parameters that dictate such molecular interactions can find immense use in the modulations of the ligand-macromolecular recognition process. In recent years, microfluidics (MF) is finding its way in more and more practical applications in a vast majority of fields including physics, biology as well as in many chemical applications such as separation of products, polymerase chain reactions, etc. [1, 2]. During the past decade, it outweighed the traditional analytical instruments, as it provides a means for reducing both analysis time and the amount of reagents necessary to perform each analysis. Virtually, the microfluidics methodology is based on the low Reynolds number as well as the diffusion of the analytes or particles of interest [3, 4]. Within the microchannel, diffusion plays a critical role in the reaction or mixing mechanism, and proper mixing requires certain tactics [5] involving the suitable control of flow rates and the complex microfluidics geometry. One important aspect of the microfluidics methodology lies in the kinetics study of chemical and biological phenomena. Kinetics studies of fast processes in flasks are cumbersome due to the lack of homogeneity and relatively slow mixing that typify batch processes [6-8]. On the other hand, the stopped-flow

method [9] has been a quite widespread technique to monitor fast chemical reactions, where the reaction is terminated at the fluidics path. The bulk approach provides the information about the end-point of reactions or interactions, but it lacks the valuable information regarding the intermediary steps. Similarly, in case of stopped-flow kinetics, [10-13] the achievable time resolution, to date, is in the order of milliseconds [14].

In contrary, in case of continuous flow microfluidics, both end-point as well as location-specific in-depth information can be obtained [15-17], enabling to envisage and interpret reactions/interactions profiles more appropriately. The kinetic information (time scales) can be extracted through space-to-time conversion by measuring the product formation at different positions along the microchannel. Until now, the exploration of reaction kinetics using MF techniques essentially focuses on the ability to control the reaction, and the use of a minimum amount of reagent [18-20], and rather less efforts have been made for the enhancement of time resolution associated with diffusion-controlled reactions [7, 21-23]. However, better time resolution in such reactions is essential in order to reveal the “missing” parts in the kinetics such as the existence of intermediate states in a molecular recognition process. By thoughtful adjustment of the flow rate and geometry of the microchannel, the reaction within MF channel initially takes place, which ensures that the extent of the reaction changes significantly from the start to the end of the flow path [16]. The reaction profile can be obtained by the quantitative comparison of the reaction product(s) or reactants themselves [24]. It is not always crucial for the reaction to be completed by the end of the microchannel; the only prerequisite is that the selected analytical technique (e.g., fluorescence intensity [25] decay time, fluorescence lifetime image [15], etc.) is sensitive enough to detect the change in the product or reactant concentrations along the flow path.

The present work describes the development of microfluidics as an advanced analytical platform for studying molecular interactions or even very fast chemical reactions. The use of time-resolved fluorescence spectroscopy as well as fluorescence microscopy enables us to follow the reaction kinetics with better time resolution revealing the intermediate states of molecular recognition and providing a way to correlate different sets of experimental data. The special design of the flow channel enables it to withstand higher flow rates (~ 14 ml/min) without any leakage or turbulence and a specifically small region of the microchannel serves the purpose of achieving significantly higher time resolution. The developed platform is capable of providing a time resolution as good as sub-hundred nanoseconds with the suitable adjustment of flow rates, which is not possible to achieve with existing stopped-flow techniques. As demonstrated with a fast ionic reaction between sodium hydroxide and phenolphthalein, microsecond-resolved kinetics was observed. The same MF platform also serves the purpose of a stopped-flow method as the flow velocity can be brought to zero after which the diffusion process can be followed. The process is the reverse of the existing stopped-flow techniques and can be termed as “flow-stopped” method. It provides an efficient way for studying diffusion-controlled phenomena such as energy/charge transfer in biomolecular interactions. We have further applied our MF system for the investigation of intermediate states involved in the molecular recognition of macromolecular self-assemblies (micelles with different charges) and genomic DNA (from salmon testes) by small ligands (Hoechst 33258 (H258), Ethidium bromide (EtBr)).

6.2. Results and discussion:

6.2.1. An improved microfluidics approach for monitoring real-time interaction profiles of ultrafast molecular recognition [26]: Figure 6.1(a) portrays the used MF system, represented as the Y-shaped MF chip. In order to study a fast model reaction in our MF device, the ionic reaction of sodium hydroxide with

phenolphthalein ($\text{H}_2\text{P}_{(\text{aq-colourless})} + 2\text{OH}^- \rightarrow \text{P}_{\text{aq}}^{2-} + 2\text{H}_2\text{O}$) was chosen. The flow rate of 7 ml min^{-1} for each channel, i.e., 14 ml min^{-1} of overall fluid front velocity in the MF channel leading to a spatial resolution of 70 $\text{ns } \mu\text{m}^{-1}$, does not reveal any detectable reaction product in the channel, even at the end of the small channel (Figure 6.1a: X region). The observation clearly shows that the formation of product is negligible even after 165 μs of confluence. However, the flow rate of 500 $\mu\text{l/min}$ in each channel, leading to a spatial resolution of 1 $\mu\text{s } \mu\text{m}^{-1}$ clearly reveals the formation of the anionic pink species (Figure 6.1b). The intensity of the anionic pink species increases steadily along the microchannel.

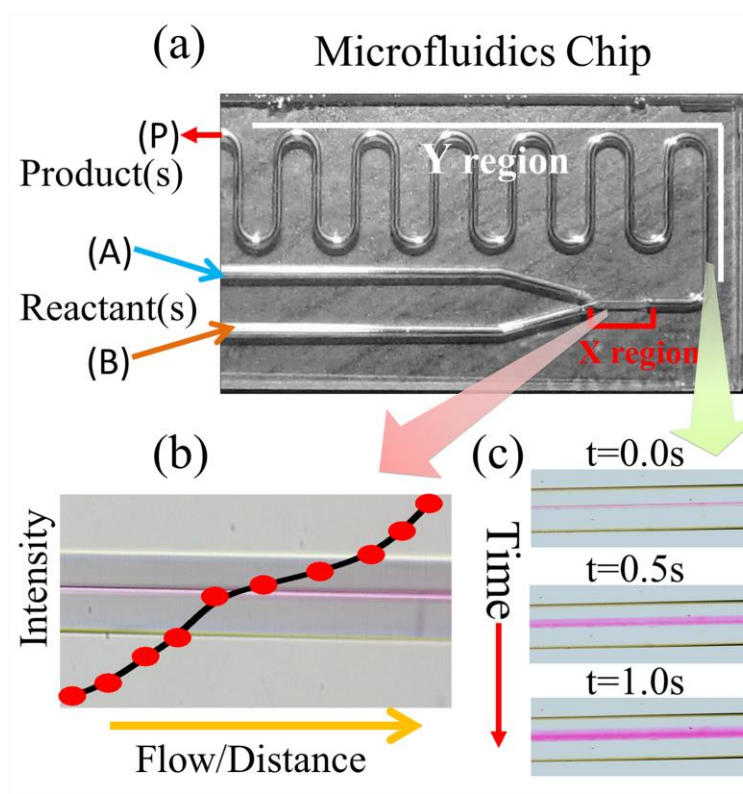


Figure 6.1. (a) Specially designed microfluidics chip for the measurement of ultrafast kinetics. Two specific regions are shown: X, for fast sub-100 ns kinetics and Y, for slower kinetics. (b) A fast ionic model reaction between sodium hydroxide and phenolphthalein measured in the microfluidics chip (X region) on the microsecond time scale is shown. (c) The “flow-stopped” methodology applied to the same ionic reaction at a fixed position (Y region) of the microchannel without any flow of the reactants is shown. The snapshots reveal the role of diffusion in the ongoing reaction (see text).

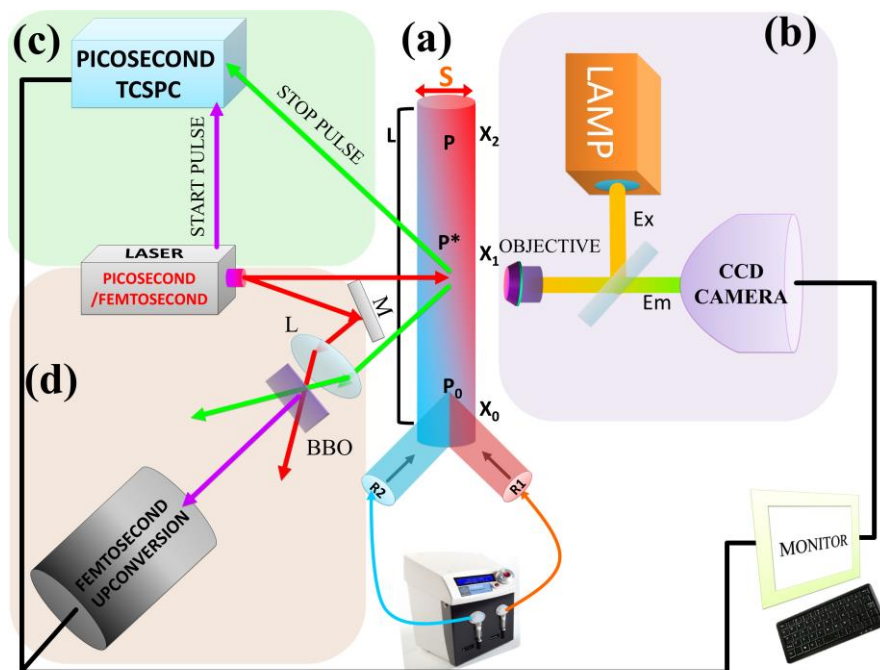


Figure 6.2. (a) Schematic presentation of the developed microfluidics platform. L denotes the flow path length, X_i are the positions for measurements along the channel, and S is the cross section of the microchannel. (b) The fluorescence microscope coupled to the microfluidics channel. A CCD camera captures images of the ongoing reactions inside the microchannel. (c) Picosecond-resolved fluorescence technique (TCSPC) for the collection of decay profiles along the microchannel. (d) Femtosecond upconversion technique combined with the microfluidics platform for studying ultrafast dynamics.

The pseudo-first-order rate constant was estimated to be $3.2 \times 10^{-4} \text{ s}^{-1}$, which is almost similar to the reported literature value ($0.7 \times 10^{-4} \text{ s}^{-1}$) [27]. Figure 6.1c reveals the MF platform for studying diffusion-controlled reactions without any external velocity components, i.e., essentially as in the flow-stopped method, for the same reaction as described above. The intensity as well as the width of the product zone increases with time, enabling to visualize the diffusion process. The method was also found to be very efficient for studying diffusion-controlled biological phenomena such as energy/charge transfer processes in protein-protein and protein-DNA interactions. The diffusion controlled energy transfer process in solution phase was visualized in the recognition process of lambda repressor protein with operator DNA [28].

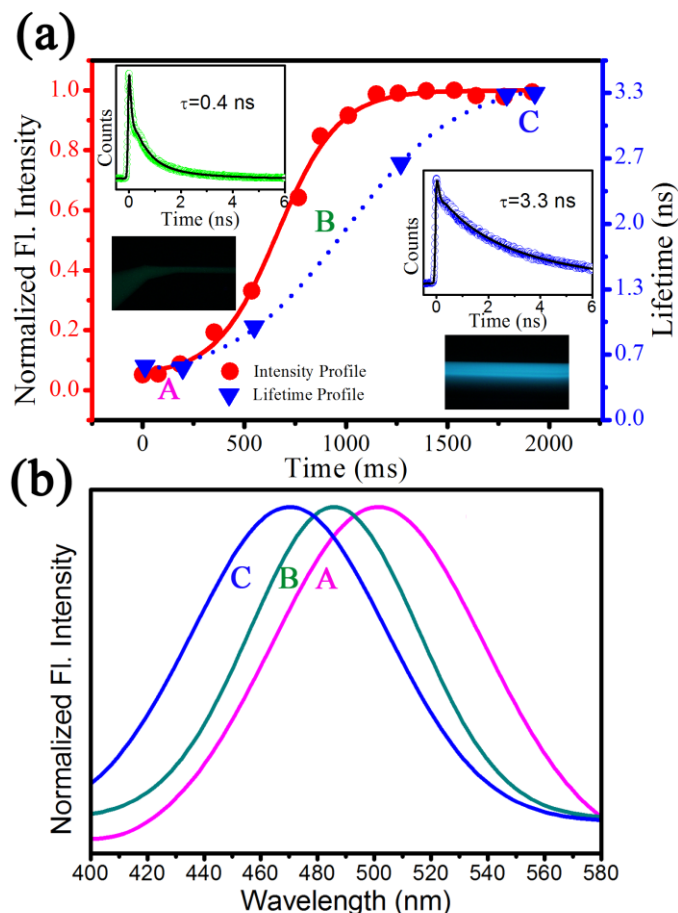


Figure 6.3. (a) Fluorescence intensity profile of H258 in the complexation reaction with SDS (red dots). Fluorescence images showing the extent of the reaction along the microfluidics channel as revealed by the increase in fluorescence intensity and change in the fluorescence maximum (inset images). Picosecond-resolved fluorescence transients of H258 (inset traces) depicting the dynamical lifetime of H258 along the channel (blue triangles). Solid and dotted lines indicate the fit of the experimental data with the appropriate kinetic equation as described in the text. (b) Depicts the change in the fluorescence emission maximum in the course of the complexation. A, B, and C denotes three positions along the microchannel as shown in the upper panel of the figure. The emission maximum is blue shifted from 500 nm (A), to 485 nm (B), and finally to 470 nm (C).

In order to study the time-resolved reaction pathways associated with the molecular recognition (complexation) with self-assembled anionic SDS micelles by a cationic ligand H258, fluorescence microscopy and picosecond-resolved emission spectroscopy with our MF device (Figure 6.2) was employed. The anionic micelles are good mimics of DNA [29], having a negatively charged surface and hydrophobic interior. The cationic ligand H258 is a well-known DNA minor

groove binder [30], which reveals significantly higher fluorescence yield in hydrophobic environments compared to that in bulk water. It has earlier been shown that H258 remains at the interface of the SDS micelles projecting its cationic charges toward the anionic SDS head groups and the bis-benzimidazole moiety at the hydrophobic side [30].

In this regard, the molecular recognition of SDS micelles by H258 is expected to be interesting, as there are two possible ways of complexation. H258 may directly approach the micelle and form the complex (single step), or the ligand may form an intermediate complex with the micelle via electrostatic interaction, and finally form the energy minimized complex as revealed in equilibrium (two steps). Figure 6.3a displays the interaction profile of H258 with SDS micelle based on the detected fluorescence images as well as fluorescence transients along the channel at desired specific locations. The overall flow rate was kept at 150 $\mu\text{l}/\text{min}$. In Figure 6.3a, the numerical fit of the fluorescence intensity (red solid line) according to equation (2.74) for multistep kinetics was found to be reasonably good, indicating the reaction pathway to be a two-step process (Figure 6.6a) [31]. The overall rate constant of the interaction profile was estimated to be 2.1 s^{-1} . The fluorescence lifetime of H258 increases (0.4 ns to 3.3 ns) along the microchannel and the pattern is consistent with the increase of fluorescence intensity value as well as the change in emission maximum (500 nm to 470 nm, emission maximum is blue shifted as indicated in Figure 6.3b). The reported lifetime value of H258 in buffer is $\sim 300\text{ ps}$ [15] which is similar to the value obtained at the mixing point of the Y junction (Figures 6.1a and 6.2a). The observation reveals insignificant interaction of H258 with the SDS micelle at the mixing point (X_0 of Figure 6.2a). At the saturation point of the reaction profile of H258-SDS binding, the lifetime value of H258 was measured to be 3.3 ns in the MF channel, which closely resembles the lifetime of H258 in SDS micellar environment in equilibrium [32]. We have also studied the nature of complexation of H258 with cationic (CTAB) and neutral (TX-100) micelles as shown in Figure 6.4. The

complexation of H258 with the two micelles is consistent with the kinetic pathways as described in Equation (2.73), which is one-step in nature (Figure 6.6b). From these studies on the complexation of H258 with model micellar systems, interesting pathways associated with the molecular recognition of DNA in the minor groove binding [30] of H258 can be anticipated.

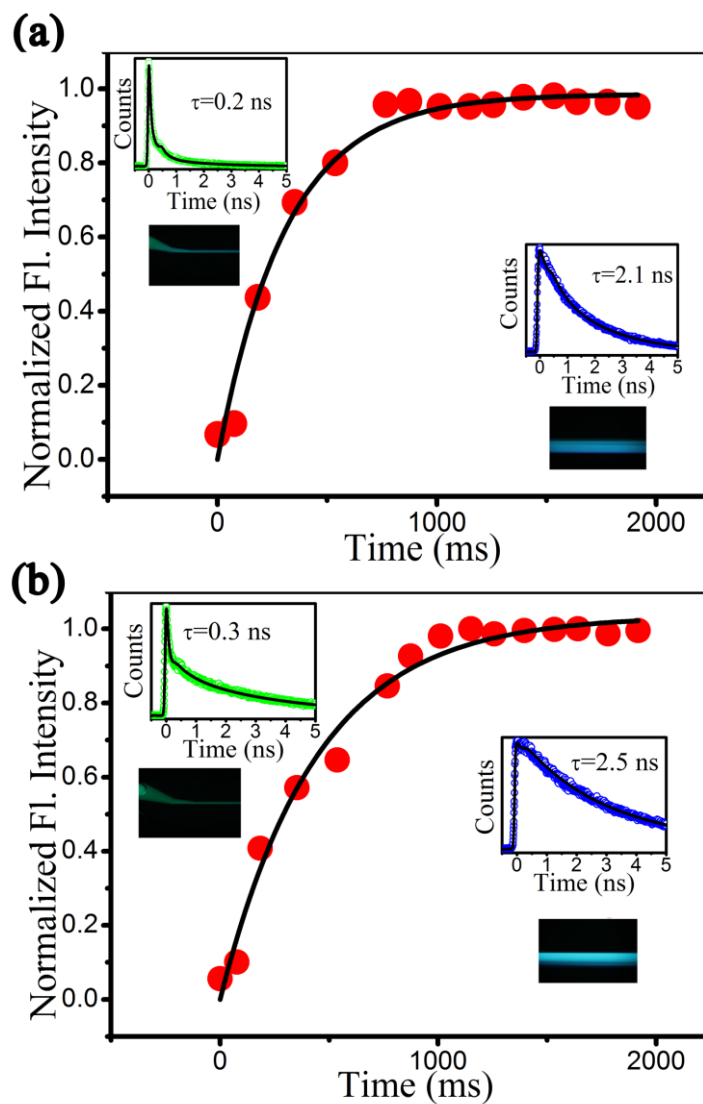


Figure 6.4. Fluorescence intensity profile of H258 in the complexation reaction with CTAB (a) and TX100 (b), respectively. Fluorescence images (insets) showing the extent of the reaction along the microfluidics channel as revealed by the increase in fluorescence intensity. Picosecond-resolved fluorescence transients of H258 (inset traces) depicting the dynamical lifetime of H258 along the channel during the complexation.

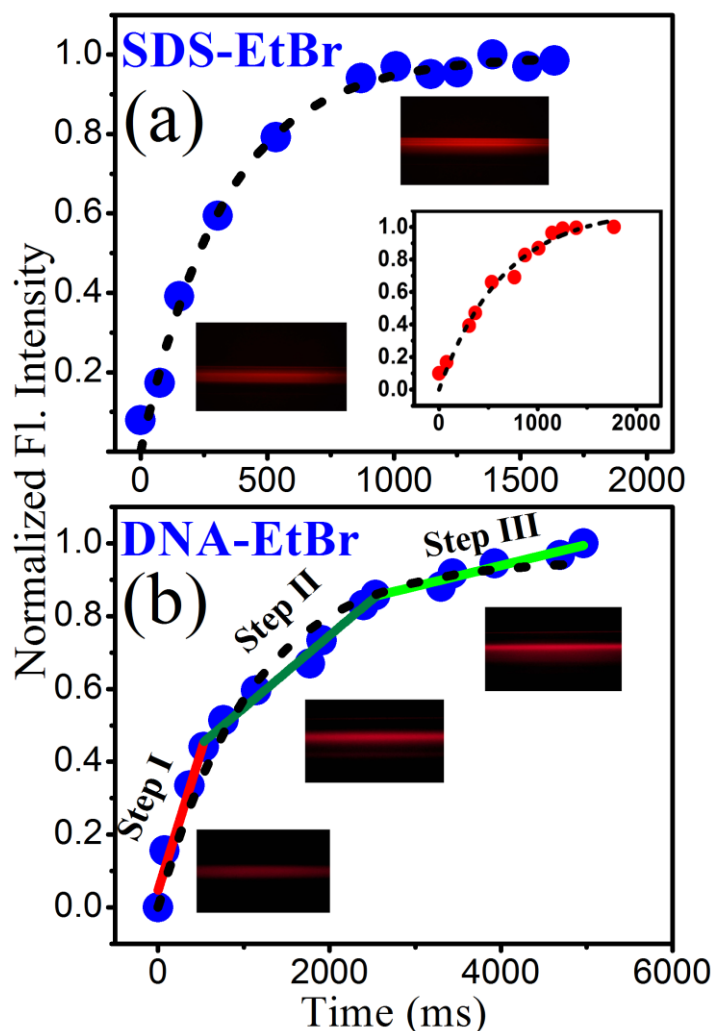


Figure 6.5. Fluorescence intensity profile of EtBr along the microchannel as obtained from the fluorescence microscope. The complexation of the probe EtBr with the SDS micelle (a) and the three step intercalation process of the probe into the DNA (b) are shown. Dashed lines indicate the fits of the experimental data (dots) to the appropriate kinetic equations as described in the text. The inset of (a) depicts the fluorescence intensity profile of EtBr-TX100 complexation.

In addition, the developed MF system was used in order to study the molecular recognition of DNA by a well-known intercalator, EtBr. In this endeavor, the interaction profile of EtBr with anionic SDS micelle was studied as shown in Figure 6.5a. The intensity profile of EtBr upon complexation with the micelle reasonably follows a one-step mechanism. The first-order rate constant was calculated to be 3.0 s^{-1} . In the case of the neutral TX-100 micelle, the complexation pathway is comparable to that of the SDS micelle as shown in the

inset of Figure 6.5a. The emission of the cationic ligand EtBr does not change appreciably from that in bulk water in the presence of the cationic CTAB micelle revealing negligibly small interaction with the micelle. On the other hand, multi-step pathways involved in the complexation of EtBr with the genomic DNA are very clear from the intensity profile as shown in Figure 6.5b. It has to be noted that, the enhancement of fluorescence intensity of the EtBr probe is associated with the decrease in the dielectric constant of the host medium around the probe [33] associated with retarded proton transfer in EtBr. It has been shown that the local dielectric environment around DNA reveals a radial distribution of dielectric constants from a value of 2 at the center to 80 at 5 Å away from the DNA surface [34]. At the DNA surface, the dielectric constant is found to be around 4-12 [35].

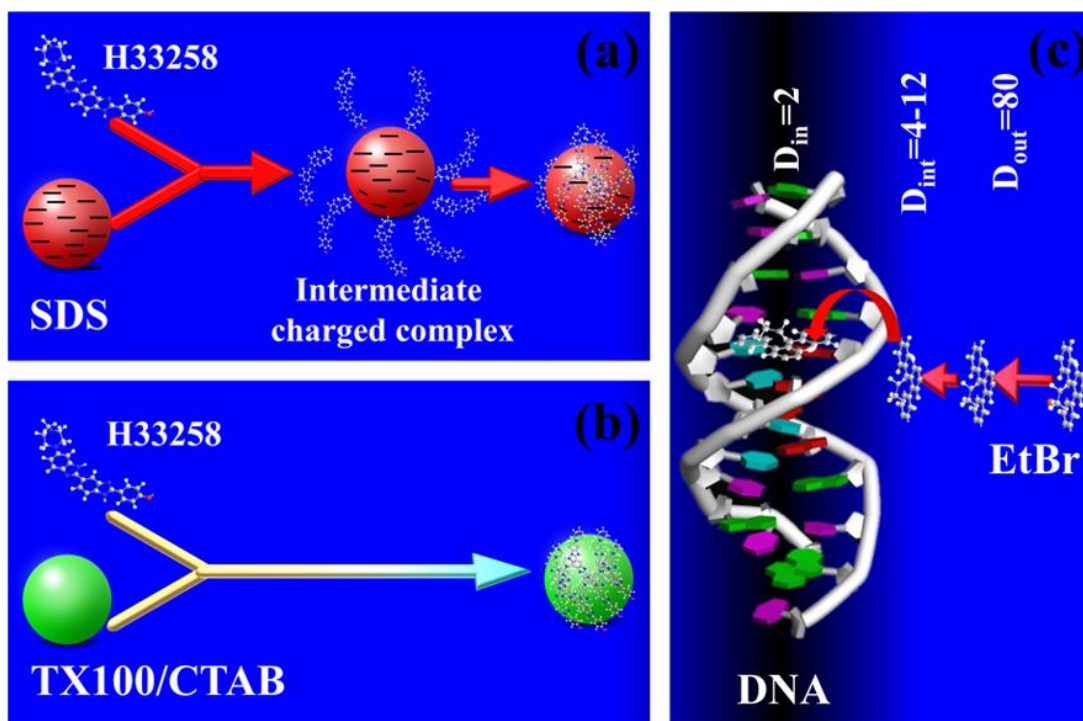


Figure 6.6. (a) Schematic showing the formation of the intermediate charge complex for the molecular recognition of SDS micelles with H258. (b) One-step molecular recognition of TX100 and CTAB micelles with H258. (c) Schematic of DNA-EtBr interactions. D_{in} , D_{int} , and D_{out} are the dielectric values at the DNA centre, at the DNA surface and in bulk water, respectively. The scheme describes the multi-step intercalation process of EtBr into the DNA.

Thus, in the course of intercalation, the intercalator EtBr has to diffuse through three distinct environments with different dielectric constants as shown in Figure 6.6c. The observation of intercalation in terms of intensity enhancement of EtBr as shown in Figure 6.5b distinctly reveals three different regions. The observation is consistent with the fact that the probe EtBr has to interact with the surface of the DNA, probably making an intermediate surface adduct before the final intercalation. The overall rate constant for the DNA-EtBr interaction was estimated to be 0.9 s^{-1} , which is in reasonably good agreement with the reported value (0.7 sec^{-1}) [36].

6.3. Conclusion: In summary, the developed MF system provides an alternative for studying complex chemical and biological systems with sub-100 ns resolution. The platform provides an alternative way for achieving a better time resolution to study very fast kinetics. The incorporation of time-resolved spectroscopy further reinforces the technique to observe the decay dynamics. The successful implementation of the approach explored the complexation behavior of two drugs in bio-mimetic and biological systems. The key findings include the identification of the intermediate pathways of EtBr intercalation into DNA. The micellar systems provide a significant insight in the complexation of macromolecular recognition. Overall, our approach may be well applied to biological systems like protein-DNA, protein-protein interactions to visualize and interpret the underlying mechanism. The indigenous developed microfluidic platform allows extraction of location-specific data, which in turn provides a better tool to diagnose a chemical reaction with higher time resolution.

References

1. J.W. Hong and S.R. Quake, Integrated nanoliter systems. *Nat. Biotechnol.*, **21** (2003) 1179.
2. M.G. Whitesides, The origins and the future of microfluidics. *Nature*, **442** (2006) 368.
3. A.P. Sudarsan and V.M. Ugaz, Multivortex micromixing. *Proc. Natl. Acad. Sci. USA*, **103** (2006) 7228.
4. T.M. Squires and S.R. Quake, Microfluidics: Fluid physics at the nanoliter scale. *Rev. Mod. Phys.*, **77** (2005) 977.
5. S. Yao and O. Bakajin, Improvements in mixing time and mixing uniformity in devices designed for studies of protein folding kinetics. *Anal. Chem.*, **79** (2007) 5753.
6. G.H. Seong and R.M. Crooks, Efficient mixing and reactions within microfluidic channels using microbead-supported catalysts. *J. Am. Chem. Soc.*, **124** (2002) 13360.
7. C. Wang, S.J. Li, Z.Q. Wu, J.J. Xu, H.Y. Chen and X.H. Xia, Study on the kinetics of homogeneous enzyme reactions in a micro/nanofluidics device. *Lab Chip*, **10** (2010) 639.
8. W.D. Ristenpart, J.D. Wan and H.A. Stone, Enzymatic reactions in microfluidic devices: Michaelis-Menten kinetics. *Anal. Chem.*, **80** (2008) 3270.
9. K.R. Fox and M.J. Waring, Stopped-flow kinetic studies on the interaction between echinomycin and DNA. *Biochemistry*, **23** (1984) 2627.
10. J. Mori, Y. Miyashita, D. Oliveira, H. Kasai, H. Oikawa and H. Nakanishi, Stopped-flow analysis on the mechanism of perylene nanoparticle formation by the reprecipitation method. *J. Cryst. Growth*, **311** (2009) 553.
11. J. Alves, C. Urbanke, A. Fliess, G. Maass and A. Pingoud, Fluorescence stopped-flow kinetics of the cleavage of synthetic oligodeoxynucleotides by the EcoRI restriction endonuclease. *Biochemistry*, **28** (1989) 7879.

12. J. Jiang, J.F. Bank and C.P. Scholes, Subsecond time-resolved spin trapping followed by stopped-flow EPR of Fenton reaction products. *J. Am. Chem. Soc.*, **115** (1993) 4742.
13. T.D. Pollard, P. Maupin, J. Sinard and H.E. Huxley, A stopped-flow/rapid-freezing machine with millisecond time resolution to prepare intermediates in biochemical reactions for electron microscopy. *J. Electron. Microsc. Tech.*, **16** (1990) 160.
14. G. Feng and T. Jia, A millisecond infrared stopped-flow apparatus. *Appl. Spectrosc.*, **60** (2006) 1477.
15. R.K.P. Benninger, O. Hofmann, B. Önfelt, I. Munro, C. Dunsby, D.M. Davis, M.A.A. Neil, P.M.W. French and A.J. Mello, Fluorescence-lifetime imaging of DNA-dye interactions within continuous-flow microfluidic systems. *Angew. Chem. Int. Ed.*, **46** (2007) 2228.
16. S. Mozharov, A. Nordon, D. Littlejohn, C. Wiles, P. Watts, P. Dallin and J.M. Girkin, Improved method for kinetic studies in microreactors using flow manipulation and noninvasive raman spectrometry. *J. Am. Chem. Soc.*, **133** (2011) 3601.
17. O. Bilsel, C. Kayatekin, L.A. Wallace and C.R. Matthews, A microchannel solution mixer for studying microsecond protein folding reactions. *Rev. Sci. Instrum.*, **76** (2005) 014302.
18. H. Song and R.F. Ismagilov, Millisecond kinetics on a microfluidic chip using nanoliters of reagents. *J. Am. Chem. Soc.*, **125** (2003) 14613.
19. Y.J. Song, J. Hormes and C. Kumar, Microfluidic synthesis of nanomaterials. *Small*, **4** (2008) 698.
20. A. Abou-Hassan, O. Sandre and V. Cabuil, Microfluidics in inorganic chemistry. *Angew. Chem. Int. Ed.*, **49** (2010) 6268.
21. T. Robinson, H.B. Manning, C. Dunsby, M.A.A. Neil, G.S. Baldwin, A.J. de Mello and P.M.W. French, Investigating fast enzyme-DNA kinetics using

- multidimensional fluorescence imaging and microfluidics. *Proc. of SPIE*, **7593** (2010) 759304.
22. H.Y. Park, S.A. Kim, J. Korlach, E. Rhoades, L.W. Kwok, W.R. Zipf, M.N. Waxham, W.W. Webb and L. Pollack, Conformational changes of calmodulin upon Ca^{2+} binding studied with a microfluidic mixer. *Proc. Natl. Acad. Sci. USA*, **105** (2008) 542.
 23. H. Roder, K. Maki and H. Cheng, Early events in protein folding explored by rapid mixing methods. *Chem. Rev.*, **106** (2006) 1836.
 24. C.N. Baroud, A.M. Huebner, C. Abell, W.T.S. Huck and F. Hollfelder, Monitoring a reaction at submillisecond resolution in picoliter volumes. *Anal. Chem.*, **83** (2011) 1462.
 25. T. Thorsen, S.J. Maerkl and S.R. Quake, Microfluidic large-scale integration. *Science*, **298** (2002) 580.
 26. S. Batabyal, S. Rakshit, S. Kar and S.K. Pal, An improved microfluidics approach for monitoring real-time interaction profiles of ultrafast molecular recognition. *Rev. Sci. Instrum.*, **83** (2012) 043113.
 27. K.Y. Tam and F.T. Chau, Simultaneous multiwavelength study of the reaction of phenolphthalein with sodium-hydroxide. *J. Autom. Chem.*, **14** (1992) 157.
 28. S. Roy, Protein-DNA and protein-protein interactions in lambda-repressor/operator system: A review. *Curr. Sci.*, **71** (1996) 100.
 29. S. Pal, P.K. Maiti and B. Bagchi, Anisotropic and sub-diffusive water motion at the surface of DNA and of an anionic micelle CsPFO. *J. Phys.: Condens. Matter*, **17** (2005) S4317.
 30. D. Banerjee and S.K. Pal, Ultrafast charge transfer and solvation of DNA minor groove binder: Hoechst 33258 in restricted environments. *Chem. Phys. Lett.*, **432** (2006) 257.
 31. T.D. Slavnova, A.K. Chibisov and H. Gerner, Kinetics of salt-induced J-aggregation of cyanine dyes. *J. Phys. Chem. A*, **109** (2005) 4758.

32. T. Mondol, P. Rajdev, A. Makhal and S.K. Pal, Interaction of an antituberculosis drug with a nanoscopic macromolecular assembly: Temperature-dependent Förster resonance energy transfer studies on rifampicin in an anionic sodium dodecyl sulfate micelle. *J. Phys. Chem. B*, **115** (2011) 2924.
33. S.K. Pal, D. Mandal and K. Bhattacharyya, Photophysical processes of ethidium bromide in micelles and reverse micelles. *J. Phys. Chem. B*, **102** (1998) 11017.
34. M.A. Young, B. Jayaram and D.L. Beveridge, Local dielectric environment of B-DNA in solution: Results from a 14 ns molecular dynamics trajectory. *J. Phys. Chem. B*, **102** (1998) 7666.
35. J.M. Leveritt, C. Dibaya, S. Tesar, R. Shrestha and A.L. Burin, One-dimensional confinement of electric field and humidity dependent DNA conductivity. *J. Chem. Phys.*, **131** (2009) 245102.
36. C. Mandal, S.W. Englander and N.R. Kallenbach, Hydrogen-deuterium exchange analysis of ligand-macromolecule interactions: Ethidium-deoxyribonucleic acid system. *Biochemistry*, **19** (1980) 5819.

Chapter 7

Spectroscopic studies on the ultrafast migration of radiation at the engineered dielectric interface

7.1. Introduction: The efficiency of a photon source is heavily dependent on its immediate environment [1-4]. A precise control over the excited state lifetime and emission quantum yield of organic dyes and inorganic QDs involving fundamental physics of light-matter interactions is important to a number of branches of science [5-7]. Energy migration from a photon source through resonance dipole-dipole interaction (RDDI) is found to be an important way to control the emission property of the sample [8, 9]. Most important natural example of the utilization of RDDI is the photosynthesis [10]. The process is of increasing importance as a means of improving functionality and efficiency of organic material based LED [11] and laser devices [10, 12]. In a practical usage of a photon source under the RDDI, an energy donor (D) in proximity of acceptor (A), several situations can be considered. The D-A pair may be confined in a microcavity [8, 13]. It has been demonstrated that the FRET in the D-A pair is heavily influenced by the photonic mode density [8]. Locating D and A molecules at well-defined positions, the study [8] shows the transfer rate to be determined as a function of both mutual separation and cavity length. Sometimes the proximity of highly conducting noble metals (Ag, Au) to the D/A molecules may lead to extra channel for the deactivation of the D molecules through photon-surface plasmon interaction [14, 15]. In a recent study [16], we have shown that the non-radiative energy transfer from the emitting semiconductor QDs to the plasmonically active silver surface is Förster resonance energy transfer (FRET) type rather than well-known Nanosurface energy transfer (NSET) type.

Proximity of the D-A pair beyond the distance ($d > \lambda/10$) of the plasmonic interaction from the metal surface may not arise in some cases. In that case, the following two situations may arise. Firstly, if the D-A pair is within a distance of 25 nm from the metal surface, the D-A may be considered to be in a half optical cavity [8]. In that case, FRET is expected to be affected by local density of photonic mode (PMD). Secondly, if the location of the D-A pair is beyond 100 nm from the metallic reflective surface, there would be negligible effect of either PMD or plasmonic interaction in the rate of FRET. Here, we demonstrate that apparent rate of FRET is significantly affected by studying picosecond-resolved transfer of excitation energy between a QDs and organic dye at distance of $d > 100$ nm from the metallic surface (Figure 7.1b).

The physical mechanism of FRET depends on the D-A separation, R . When D and A are very close, virtual photon initiates the non-radiative energy transfer process and pre requirement for the FRET is achieved. On the other hand, when D and A are far apart ($R > \lambda/10$), the energy transfer follows radiative pathways, D-A coupling being mediated by a real photon [8, 17]. It has to be noted that dipole-dipole interaction plays the central role in both the above two process, radiative process rely on dipole far field while nonradiative transfer proceeds through the evanescent near field components.

In an earlier study, it was shown that the emission of the radiation for an excited molecule (atom) in front of a mirror is significantly influenced [18]. By studying the fluorescence lifetime of europium-dibenzoylmethene complex, at various well defined distances from a silver mirror, the study concluded the change in the fluorescence lifetime of the dye complex in the interface between two dielectrics of different refractive indices, is solely a consequence of optical interference between two waves (reflected and nonreflected) as shown in Figure 7.1. Similar studies have also been recently carried out [19-22]. The radiation of an oscillating electric dipole in front of a mirror, and the consequence of the optical interference is shown in Figure 7.1, where the radiation essentially depends on the

angle of detection (θ) as well as the separating distance (d) between emitter and surface. When the path difference between the direct and reflected beam is such that the constructive interference occurs, the molecule will radiate strongly in the direction [18]. As a consequence, amplification by the interface dipole radiation, twice the power as without mirror ($\tau_m=1/2\tau$), where τ_m and τ are the fluorescence lifetimes of the molecule in presence and absence of the mirror respectively. In contrast, when the path difference is half a wavelength smaller so that the direct and reflected beam interferes destructively, quenching of radiation occurs, where the dipole cannot radiate revealing $\tau_m=\infty$. As the energy donor-acceptor pair (D-A) is considered as a coupled oscillating dipole [23], the efficiency of energy transfer between a FRET pair in front of a mirror is of importance as a means of understanding optical radiation from the optical devices. The biological aspects of such studies include GFP, and other fluorescent probes which could have direct relevance in bioelectronics and nanobioelectronics. The absence of appropriate experimental information till date leaves open the question whether apparent FRET efficiency can be changed by the proximity of a reflecting surface and is the motive of the present work. An experiment consisted of quantifying the quenching by FRET acceptor as a function of the distance of D-A pair from reflective surfaces is illustrated in our present study.

7.2. Results and discussion:

7.2.1. Förster resonance energy transfer in a nanoscopic system on dielectric interfaces [24]: The characterization of the QDs was done using a transmission electron microscope (TEM). The average diameter of the QDs obtained from the TEM image was estimated to be 3.8 nm and the TEM image is represented in Figure 7.2a. The inset figure represents the size distribution of the QDs. The inset snapshot reveals the existence of a fringe ensuring high crystallinity of the QDs. The interplanar distance of 0.34 nm is consistent with the (111) planes of cubic CdSe [25]. Energy dispersive X-ray spectroscopy (EDAX) analysis of the QDs provided the atomic composition of the QDs as represented in Figure 7.2b. Steady-

state emission quenching of QDs in presence of merocyanine (MC) is represented in Figure 7.3a. Alongside, the emission spectrum of MC is also shown. As shown in the figure, the possible contribution of MC emission at 542 nm can be safely ruled out. Figure 7.3b represents the photoluminescence (PL) lifetime of QDs-MC complex collected at 542 nm and 620 nm. The efficiency of energy transfer from QDs to MC is justifiable from the decay component in QDs lifetime (542 nm) which is manifested in the rise component in MC (620 nm) lifetime.

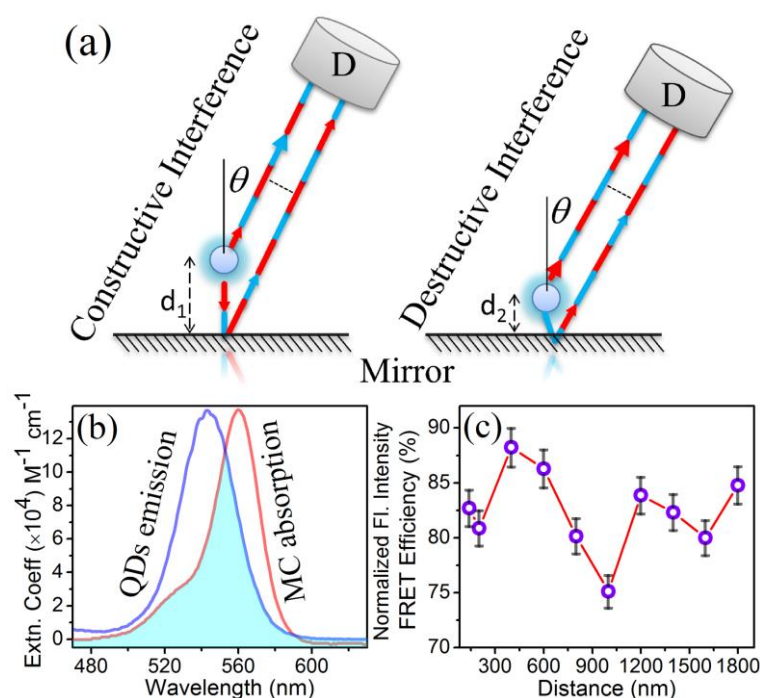


Figure 7.1. (a) Schematic for the optical interference near interfaces. The constructive (for d_1) and destructive interference (for d_2) is shown for a dipole emitter near the reflective mirror. (b) Spectroscopic data for the donor (QDs) and acceptor (MC) molecules. The shaded region depicts the overlap between QDs emission and MC absorption cross-section. The donor emission is normalized with respect to the MC extinction coefficient. The overlap integral is estimated to be $5.5 \times 10^{15} M^{-1} cm^{-1} nm^4$ considering the extinction coefficient of MC ($138000 M^{-1} cm^{-1}$) at 560 nm. (c) Change in apparent FRET efficiency for the conjugate dipolar system, QDs-MC, due to the optical interference is presented.

It has to be noted that both the lifetime and steady-state quenching of QDs in QDs-MC conjugate occur due to non-radiative energy transfer from QDs to MC and not due to surface modification of QDs by MC ligand [26]. To highlight the significant

role played by the silver interface, we measured the PL lifetime of both point dipole (QDs) and coupled dipole system (QDs-MC conjugate) as a function of distance between them and the silver interface for several different spacer layers.

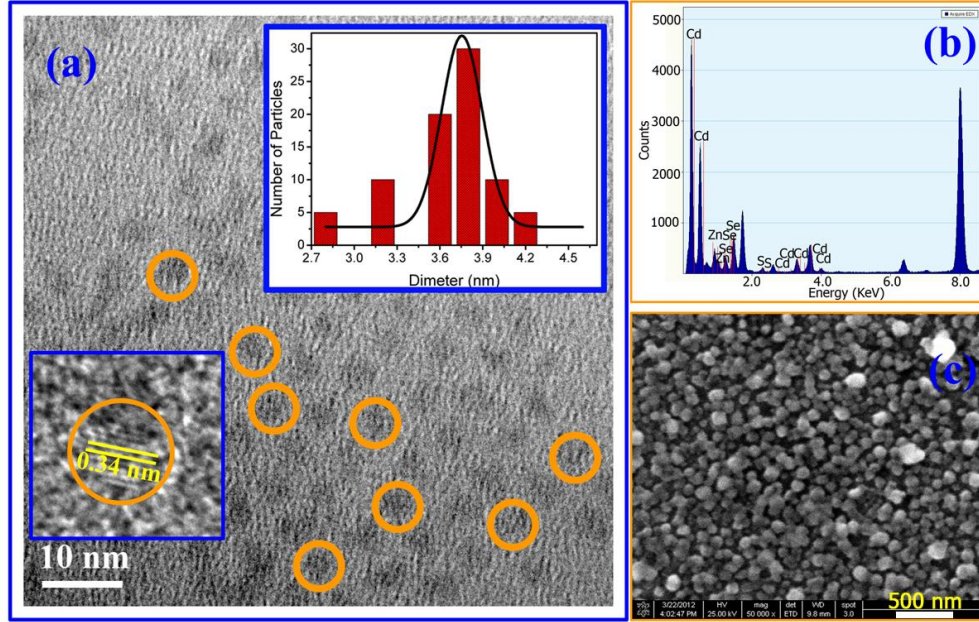


Figure 7.2. (a) TEM images of the CdSe/ZnS QDs. The size distributions of the particles are represented in the inset figure. The particle diameter was estimated to be 3.8 nm. The inset snapshot represents the HRTEM of the particle with distinct crystal fringes. (b) EDAX analysis of the QDs revealing the atomic compositions. (c) Represents the SEM images of the silver film over the glass substrate.

If the presence of the interface was of no consequence, one would expect the lifetime in presence and absence of the interface to be unaffected. However, for both point dipole and coupled dipole system (D-A), significant lifetime variation was observed, which is graphically presented in Figure 7.4. Figure 7.4a represents the time-resolved PL decay of CdSe/ZnS QDs located at various distances from the silver interface. The distance was varied up to $\sim 1.6 \mu\text{m}$. The PL decays show the enhancement and quenching of lifetime depending on the spacer layer thickness. The relative lifetime variation is plotted against the distance in Figure 7.4b. As shown in the figure, the lifetime follows oscillatory behavior. The D-A distance from the time-resolved FRET on bare glass was estimated to be 3.7 nm

which is consistent with our system under study (1.9 nm CdSe core + 0.3 nm ZnS shell + 1.2 nm ligand distance).

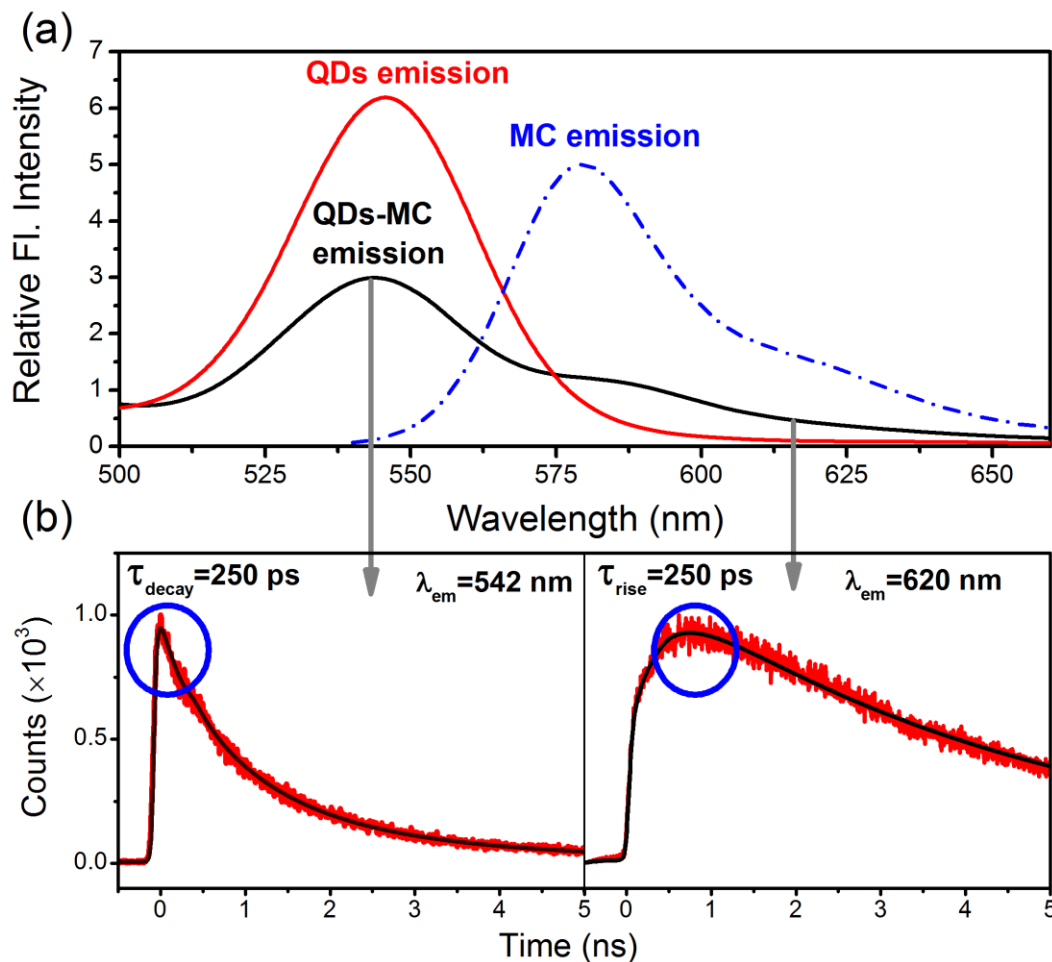


Figure 7.3. (a) Steady-state spectrum of QDs in presence and absence of MC is shown. The PL of QDs in presence of MC is significantly quenched. Alongside, the emission spectrum of MC is shown (dotted lines). From the figure, it is evident that at 542 nm detection wavelength, the possible contribution of MC emission can be safely ruled out. (b) Represents the PL decay of QDs-MC conjugate systems collected at two different wavelengths, 542 nm and 620 nm. The decay collected at 542 nm shows the lifetime quenching of QDs due to energy transfer from QDs to MC and is reflected by the faster decay component of 250 ps. The decay collected at 620 nm exhibits the lifetime of MC and due to energy transfer, the rise component of 250 ps is manifested in its lifetime decay.

On the silver surface, the lifetime of QDs is significantly quenched, which is due to the energy transfer from QDs to silver film, and is consistent with one of our previous studies [16]. However, in presence of PVA spacer layer, there is no

direct energy transfer feasibility from QDs to silver film due to the larger distance ($d > 100$ nm). Therefore, the lifetime variation of QDs is solely due to the light wave interference. In the next step, we measured the PL lifetime of QDs-MC conjugate, a dipole pair, which serves as FRET pair. The lifetime decays of QDs-MC conjugate having various distances from the interface are presented over Figure 7.4c and the oscillatory nature of the relative lifetime values are plotted in Figure 7.4d.

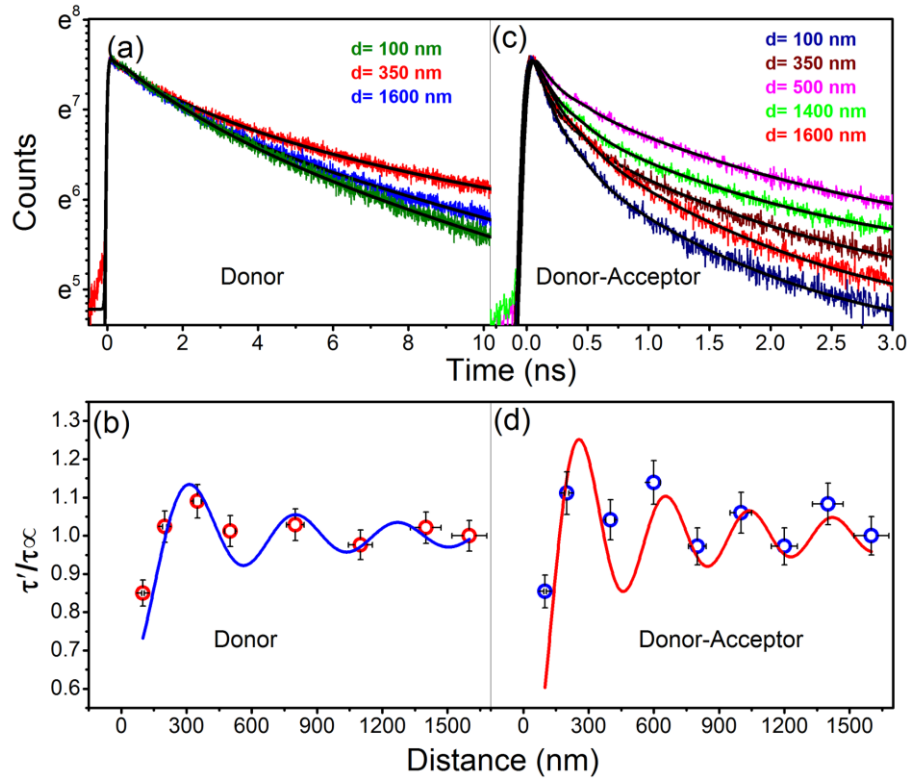


Figure 7.4. (a) and (c) the fluorescence transients of QDs and QDs-MC conjugate with varying distance from the silver mirror. The excitation wavelength was 375 nm. The decay was collected at the emission maximum of QDs (542 nm). (b) and (d) the dependency of QDs lifetime on mirror distances are graphically presented. The open circles with 5% error bar represent the experimental data. The line curve is the fitted plot of the experimental data to equation (7.3).

The outcome of this lifetime variation greatly influences the apparent energy transfer efficiency as presented over Figure 7.1c. The apparent energy transfer efficiency, estimated considering the lifetime changes for both the donor

(QDs) and donor-acceptor (QDs-MC) system at various spacer distances due to optical interference, changes from 75% to 89%. In order to establish the fact that the lifetime alteration is solely due to reflective interference, we further extended our study using silicon wafer as a reflective interface. The polished silicon wafer does not possess any plasmonic absorption characteristic like the silver film [27]. For silicon wafer, similar results were obtained (Figure 7.5) as of silver surface.

The fluorescence lifetime of the coupled dipolar system was also found to have distance dependency. The study with silicon clearly rules out the possibility of direct energy transfer that might be arising due to the silver absorptivity. It is now instructive to compare the obtained data with the existing model. The lifetime variation in front of reflecting surface as described by Drexhage [18] is well relevant to our system under study. In case of a plane reflective surface, the decay time (τ) can be expressed as follows:

In case of electric dipole oscillator parallel to the mirror,

$$\frac{\tau}{\tau_{\infty}} = \left[1 + \frac{3}{4} \int_0^1 \rho_{\parallel}(u) u^2 \cos(xu - \delta_{\parallel}(u)) du + \frac{3}{4} \int_0^1 \rho_{\perp}(u) u^2 \cos(xu - \delta_{\perp}(u)) du \right]^{-1} \quad (7.1)$$

Where $x = \frac{4\pi nd}{\lambda}$; $u = \cos \theta$; $\rho_{\parallel}(u)$, $\rho_{\perp}(u)$ are reflection coefficients and δ is the phase shift and n is refractive index of the medium in front of the surface. In case of perfect mirror, the above equation can be solved, and the equation becomes:

$$\frac{\tau}{\tau_{\infty}} = \left[1 - \frac{3 \sin x}{2x} - \frac{3 \cos x}{x^2} + \frac{3 \sin x}{2x^3} \right]^{-1} \quad (7.2)$$

If one considers the radiation-less deactivation to be affected by the mirror, then the true decay time would be τ' and the above equation can be rearranged as follows:

$$\frac{\tau'}{\tau_{\infty}} = \left[\frac{1}{1 + n_{\infty} \left(\frac{\tau_{\infty}}{\tau} \right)} \right] \quad (7.3)$$

where η_{∞} is the quantum yield of the emitting state.

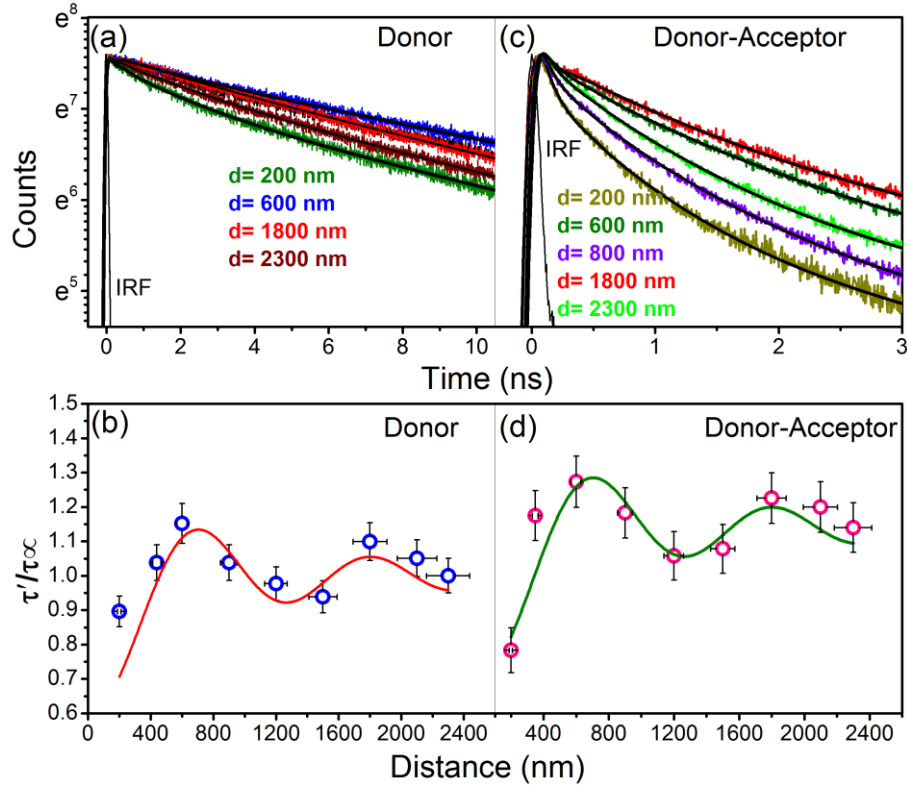


Figure 7.5. (a) and (c) the fluorescence transients of QDs and QDs-MC conjugate with varying distance from the silicon surface. The excitation wavelength was 375 nm. The decay was collected at the emission maximum of QDs (542 nm). (b) and (d) the dependency of represent the experimental data. The line curve is the fitted plot of the experimental data to equation (7.3). QDs lifetime on mirror distances are graphically presented. The open circles with 5% error bar represent the experimental data.

We applied the above theoretical model and found reasonably good fitting of our experimental data to equation (7.3). The fitting curves are represented along the respective figures (Figure 7.4 and Figure 7.5). The obtained quantum efficiencies

(0.3-0.5), from the theoretical fitting are reasonably good with the actual quantum yield of the donor system QDs (*viz.* 0.4). The quantum efficiency of the donor system (D) obtained by the model fit reflects the intrinsic quantum yield of the donor (QDs), even for the D-A conjugate system. An attempt to fit the experimental data considering the perpendicular orientation of the dipole to the mirror surface, for both the D and D-A systems, found to be not appropriate for our systems. As described in equation (7.1), the decay time of the emitter depends on emission wavelength, reflection co-efficient, phase shift and also the refractive index of the medium in front of the mirror. The reflectivity and phases shift for both the materials (silver and silicon) would be different, which will eventually contribute to the oscillatory nature of the dipolar emission.

7.3. Conclusion: In summary, this new understanding can be put to practical use. The theoretical model fit for conjugate dipolar system having lifetime dependency on surface-dipole separation (d) could provide useful information about the intrinsic quantum efficiency of the emitting dipole, which is otherwise not obtainable by general approach of quantum efficiency estimation using standard steady state and time-resolved technique. The practical application of such understanding includes many optical devices, and one of the prominent examples is organic material based light-emitting diode (OLED). In an OLED, within a microcavity, interference effects can significantly alter both the intensity and the spectrum of the emitted light [28]. In case of organic LEDs, microcavity plays a vital role where the organic layers remain sandwiched between two parallel reflectors [29, 30]. Usually, in a state-of-the-art OLED, one of the reflectors is a metallic mirror while the other is a Bragg reflector. The light beam interferes multiple times between the two reflectors producing enhanced forward-emission and spectral narrowing in these devices. An ordinary OLED, however, consists of only one effective reflector, metallic cathode. In this geometry, wide-angle interference is anticipated to dominate when directly radiated and reflected waves overlap with each other. The thickness of the light-emitting layer control the

optical path difference between the direct and the reflected waves and is crucial to the overall efficiency including angular intensity distribution and operational frequency bandwidth of an OLED.

References

1. P. Anger, P. Bharadwaj and L. Novotny, Enhancement and quenching of single-molecule fluorescence. *Phys. Rev. Lett.*, **96** (2006) 113002.
2. D. Kleppner, Inhibited Spontaneous Emission. *Phys. Rev. Lett.*, **47** (1981) 233.
3. P.T. Worthing, R.M. Amos and W.L. Barnes, Modification of the spontaneous emission rate of Eu^{3+} ions embedded within a dielectric layer above a silver mirror. *Phys. Rev. A*, **59** (1999) 865.
4. R.R. Chance, A. Prock and R. Silbey, Molecular fluorescence and energy transfer near interfaces. *Adv. Chem. Phys.*, **37** (1978) 1.
5. M.D. Leistikow, J. Johansen, A.J. Kettelarij, P. Lodahl and W.L. Vos, Size-dependent oscillator strength and quantum efficiency of CdSe quantum dots controlled via the local density of states. *Phys. Rev. B*, **79** (2009) 045301.
6. Y. Akahane, T. Asano, B.S. Song and S. Noda, High-Q photonic nanocavity in a two-dimensional photonic crystal. *Nature*, **425** (2003) 944.
7. C.S. Wolfgang, F. Masayuki, Y. Makoto, A. Takashi and N. Susumu, Light-emission properties of quantum dots embedded in a photonic double-heterostructure nanocavity. *Appl. Phys. Lett.*, **90** (2007) 231101.
8. P. Andrew and W.L. Barnes, Förster energy transfer in an optical microcavity. *Science*, **290** (2000) 785.
9. S.M. Sadeghi, R.G. West and A. Nejat, Photo-induced suppression of plasmonic emission enhancement of CdSe/ZnS quantum dots. *Nanotechnology*, **22** (2011) 405202.
10. M.A. Baldo, M.E. Thompson and S.R. Forrest, High-efficiency fluorescent organic light-emitting devices using a phosphorescent sensitizer. *Nature*, **403** (2000) 750.
11. S. Coe, W. Woo, M. Bawendi and V. Bulović, Electroluminescence from single monolayers of nanocrystals in molecular organic devices. *Nature*, **420** (2002) 800.

12. A. Dodabalapur, L.J. Rothberg, R.H. Jordan, T.M. Miller, R.E. Slusher and J.M. Phillips, Physics and applications of organic microcavity light emitting diodes. *J. Appl. Phys.*, **80** (1996) 6954.
13. X.Y. Wang, C.K. Shih, J.F. Xu and M. Xiao, Enhanced dipole-dipole interaction of CdSe/CdS nanocrystal quantum dots inside a planar microcavity. *Appl. Phys. Lett.*, **89** (2006) 113114.
14. P. Andrew and W.L. Barnes, Energy transfer across a metal film mediated by surface plasmon polaritons. *Science*, **306** (2004) 1002.
15. J. Bellessa, C. Bonnard, J.C. Plenet and J. Mugnier, Strong coupling between surface plasmons and excitons in an organic semiconductor. *Phys. Rev. Lett.*, **93** (2004) 036404.
16. S. Batabyal, A. Makhal, K. Das, A.K. Raychaudhuri and S.K. Pal, Ultrafast dynamics of excitons in semiconductor quantum dots on a plasmonically active nano-structured silver film. *Nanotechnology*, **22** (2011) 195704.
17. J.R. Lakowicz, Principles of fluorescence spectroscopy. 2nd ed. 2006, New York: Kluwer Academic/Plenum.
18. K.H. Drexhage, Influence of a dielectric interface on fluorescence decay time. *J. Lumin.*, **1-2** (1970) 693.
19. M. Achermann, Exciton-plasmon interactions in metal-semiconductor nanostructures. *J. Phys. Chem. Lett.*, **1** (2010) 2837.
20. D.S. Bradshaw, J.N.T. Peck, V.S. Oganessian and D.L. Andrews, Optically controlled energy transfer in stacked and coplanar polycyclic chromophores. *J. Phys. Chem. Lett.*, **1** (2010) 2705.
21. J.Y. Zhang, X.Y. Wang and M. Xiao, Modification of spontaneous emission from CdSe/CdS quantum dots in the presence of a semiconductor interface. *Optics Letters*, **27** (2002) 1253.
22. Y. Zhang, V.K. Komarala, C. Rodriguez and M. Xiao, Controlling fluorescence intermittency of a single colloidal CdSe/ZnS quantum dot in a half cavity. *Phys. Rev. B*, **78** (2008) 241301.

23. J. Hofkens, M. Cotlet, T. Vosch, P. Tinnefeld, K.D. Weston, C. Ego, A. Grimsdale, K. Mullen, D. Beljonne, J.L. Bredas, S. Jordens, G. Schweitzer, M. Sauer and F. De Schryver, Revealing competitive Förster-type resonance energy-transfer pathways in single bichromophoric molecules. *Proc. Natl. Acad. Sci. USA*, **100** (2003) 13146.
24. S. Batabyal, T. Mondol, K. Das and S.K. Pal, Förster resonance energy transfer in a nanoscopic system on a dielectric interface. *Nanotechnology*, **23** (2012) 495402.
25. R. He and H. Gu, Synthesis and characterization of monodispersed CdSe nanocrystals at lower temperature. *Colloids Surf.*, **272** (2006) 111.
26. S.S. Narayanan and S.K. Pal, Aggregated CdS quantum dots: Host of biomolecular ligands. *J. Phys. Chem. B*, **110** (2006) 24403.
27. P. Nagpal, N.C. Lindquist, S.-H. Oh and D.J. Norris, Ultrasoother patterned metals for plasmonics and metamaterials. *Science*, **325** (2009) 594.
28. S.K. So, W.K. Choi, L.M. Leung and K. Neyts, Interference effects in bilayer organic light-emitting diodes. *Appl. Phys. Lett.*, **74** (1999) 1939.
29. T.A. Fisher, D.G. Lidzey, M.A. Pate, M.S. Weaver, D.M. Whittaker, M.S. Skolnick and D.D.C. Bradley, Electroluminescence from a conjugated polymer microcavity structure. *Appl. Phys. Lett.*, **67** (1995) 1355.
30. R.H. Jordan, A. Dodabalapur and R.E. Slusher, Efficiency enhancement of microcavity organic light emitting diodes. *Appl. Phys. Lett.*, **69** (1996) 1997.

Chapter 8

Ultrafast spectroscopic studies on the photon-plasmon interaction at a technologically important interface

8.1. Introduction: Control over the emitting properties of a photon source is of much interest to a wide range of scientists ranging from physicists, chemists to biologists [1]. This control is essential for various potential applications including miniature lasers, light emitting diodes, single photon sources, solar energy harvesting, optical switches, optical sensors, etc [1-4]. The use of metallic surfaces for the control of the excitonic state of a photon emitter is evidenced in the literature [5, 6]. These studies exploit the reflecting properties of metal surfaces to control the local density of states (LDOS) of the photon emitter in proximity (at least 10 nm apart) [7] and carefully avoid direct contact with the metal surfaces [7] in order to disregard nonradiative energy transfer [7, 8]. Inevitably, direct contact of a photon source with a metal film brings complexity owing to the potential possibility, due to interference, of energy/charge transfer and excitonic coupling to the surface plasmon of the metallic surface [9, 10]. Although direct contact of the photon sources with metallic thin film is almost unavoidable for the realization of several photonic devices, including plasmonically coupled single photon transistors [11], there are few detailed systematic studies of the excitonic dynamics of photon sources in contact with plasmonically active metal film [9]. In a recent study, the dynamical consequence of the emission from CdSe quantum dots (QDs) on a gold thin film was demonstrated [9]. Using nanosecond resolved fluorescence spectroscopy, the study concluded the emission quenching to be nonradiative in nature. However, a detailed picture of the nonradiative energy transfer of the QDs and conclusive evidence to rule out charge transfer processes from the QDs to the gold thin film is lacking in the study.

In the present study, we have used CdSe/ZnS core-shell type semiconductor QDs of various sizes and a thin silver film (thickness 35 nm) as the model photon source and metallic surface, respectively. Using a high resolution transmission electron microscope (HRTEM) we have characterized the QDs. An atomic force microscope (AFM) and field emission gun scanning electron microscope (FEG-SEM) were used to study the nano-structured silver thin film on a quartz substrate. Picosecond-resolved fluorescence spectroscopy on the QDs in contact with the silver film explores the dynamics of excitons. Our studies also explore the type of excitonic energy transfer and the possibility of photoinduced charge migration from the QDs to the metal film. NSET [12], one of the other prevailing pathway of nonradiative quenching, was conclusively found to not to occur in this context.

8.2. Results and discussion:

8.2.1. Ultrafast dynamics of excitons in semiconductor quantum dots on a plasmonically active nano-structured silver film [13]: HRTEM images (Figures 8.1 (a-c)) reveal the diameters of the QDs to be 3.2 nm, 4.4 nm and 5.2 nm for Lake placid blue (LBP), Adirondack green (AG) and Birch yellow (BY), respectively. The existence of the fringes ensures the high crystalline nature of the QDs. The SEM (Figure 8.1(d)) and the AFM (inset of Figure 8.1(d)) images of the silver film show that it is formed by the accumulation of silver particles of various sizes ranging from microns to nanometres. The absorption band maxima of the silver thin film at 440 nm (Figure 8.2) is consistent with the presence of silver particles of diameter 10–30 nm in the thin film [14], which makes the film plasmonically active. Noble metal films having nanostructure exhibit one very interesting phenomenon known as localized surface plasmon resonance (LSPR) [15, 16] which arises from resonant oscillation of their free electrons in the presence of light. While the locations and photoluminescence (PL) peaks of the QDs on the thin film

are schematically demonstrated in Figure 8.2, the consequences of the excitonic dynamics of the QDs are evident in Figure 8.3. Each PL decay curve was fitted by a multiexponential to achieve lifetimes under various conditions.

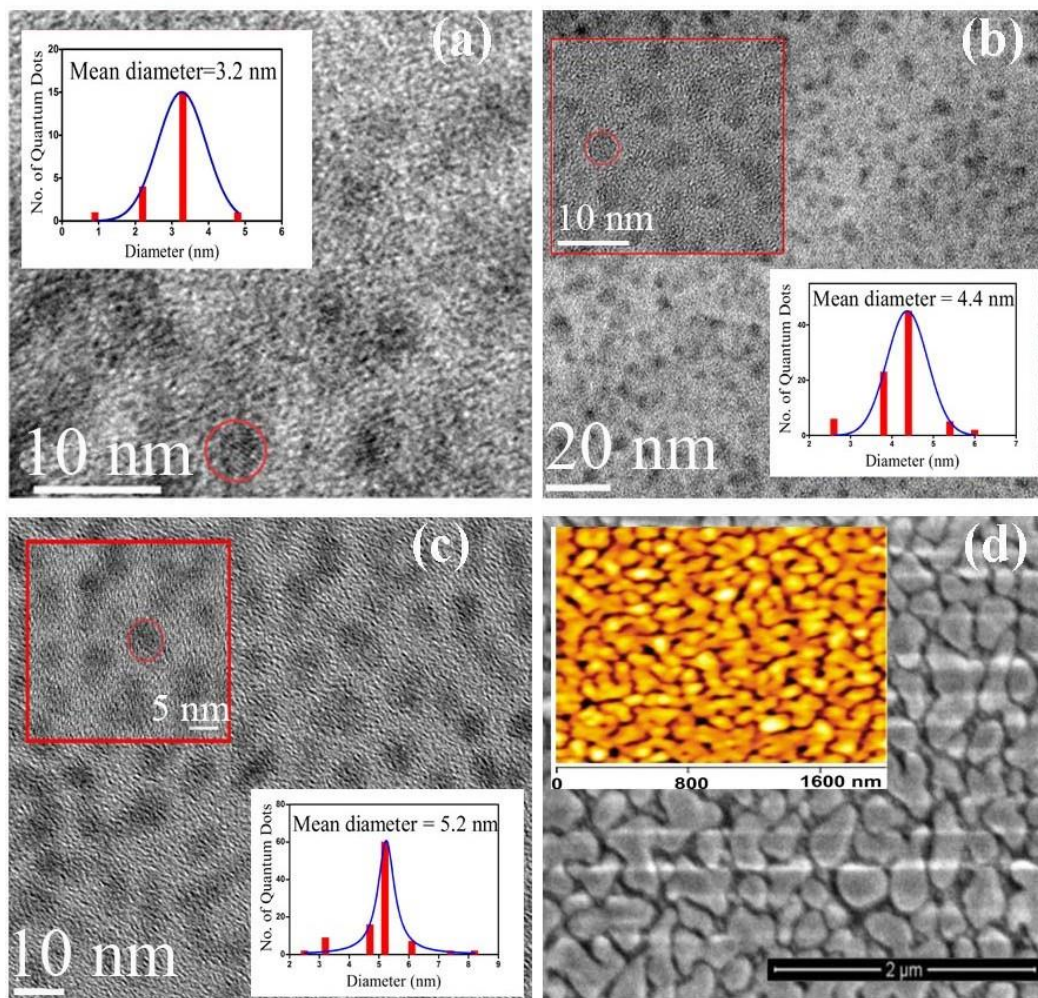


Figure 8.1. (a)–(c) HRTEM images of the QDs LBP, AG and BY, respectively. (d) SEM and AFM (inset) images of the silver film.

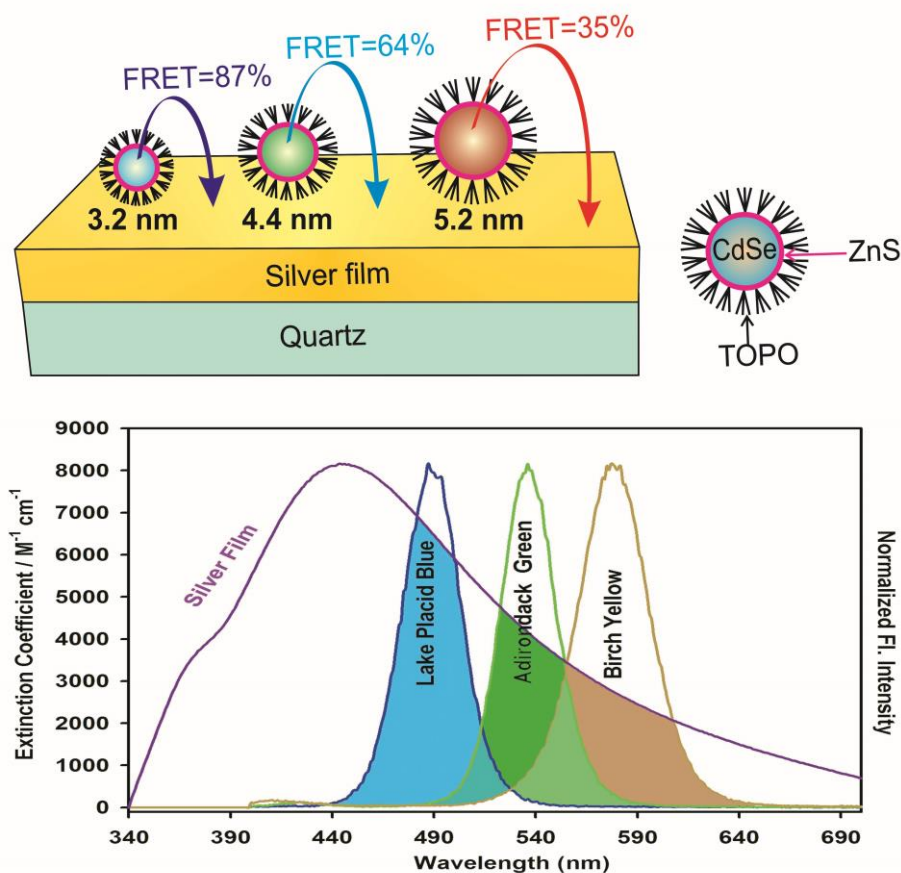


Figure 8.2. Schematic diagram of FRET from QDs to silver film (above). Overlap of the silver absorption with QDs emission (below).

Table 8.1 shows the detailed time-resolved lifetimes of the QDs. It is clearly evident from Figure 8.3 and Table 8.1 that the PL dynamics of QDs become significantly faster on the metal film compared to that on the quartz surface, which could be a consequence of either nonradiative energy transfer or photoinduced charge transfer [17] to the host film. From the Figure 8.3 and Table 8.1 it is also evident that QDs in the presence of benzoquinone (BQ) offer much faster PL dynamics than those on the metal film. Strong lifetime quenching of QDs in the presence of BQ is a typical example of excited state interfacial charge migration from QDs to BQ, the well-known electron shuttle which pumps the excited electron out from semiconductor conduction band [17-19].

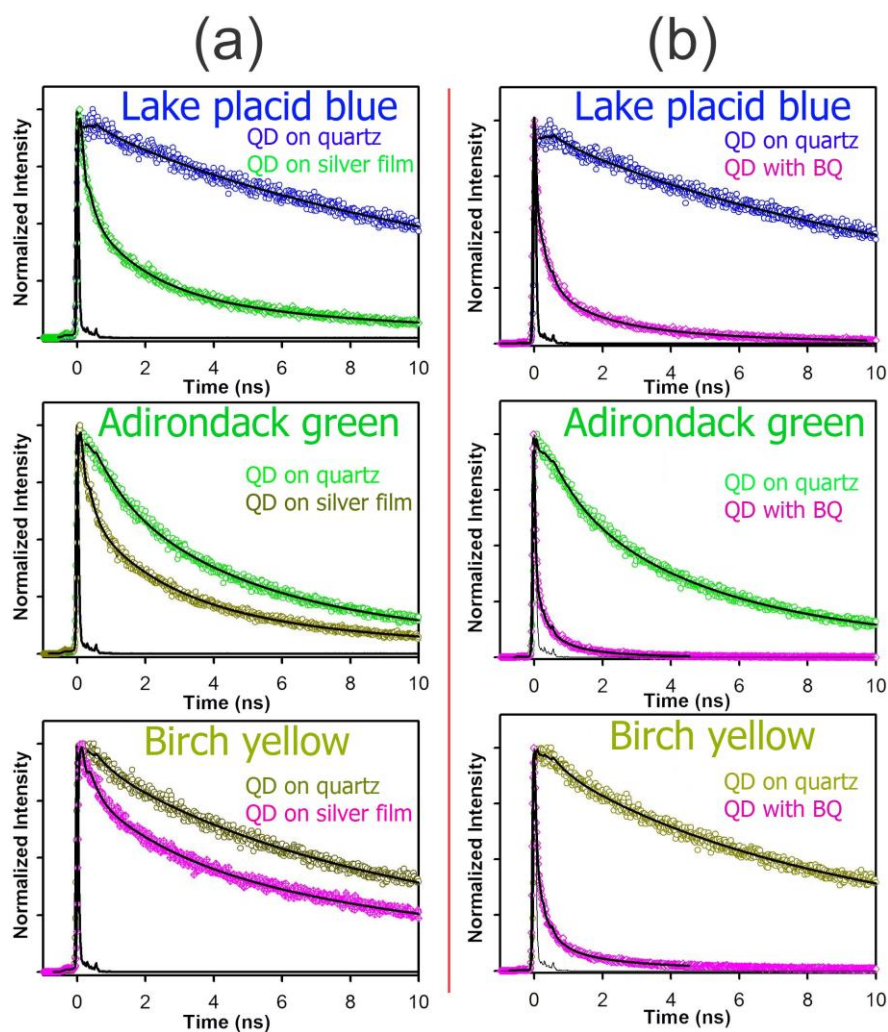


Figure 8.3. Picosecond resolved photoluminescence transients of QDs under various conditions. (a) Lifetime quenching of QDs by silver film due to energy transfer. (b) Lifetime quenching of QDs in the presence of BQ due to electron transfer.

Figure 8.3 shows the picosecond-resolved PL spectra of the QDs LPB, AG and BY under different conditions. The PL spectra were collected at the emission maximum of respective QDs. From the significant difference of the timescales of PL quenching of the QDs on the film from those in the QDs-BQ complexes (Table 8.1 and Figure 8.3), we conclude that the quenching phenomenon is attributable solely to energy transfer. The insignificantly smaller possibility of electron transfer from the QDs to the metal surface can be justified from the formation of a Schottky barrier [20] in the semiconductor metal junction. The equilibrium contact

potential V_0 , which is the order of 0.26 eV, is sufficiently higher to prevent the net electron transfer from semiconductor conduction band to metal side as shown in Figure 8.4. As demonstrated earlier, ZnS shells around the CdSe QDs are not supposed to be a barrier to charge migration [21, 22]. The nonradiative energy transfer is further justified by the strong spectral overlap between the QDs emission with the LSPR band of the silver film (Figure 8.2). Considering the energy transfer to be of the FRET type, the efficiency of energy transfer depends on the inverse of the sixth power of donor-acceptor separation.

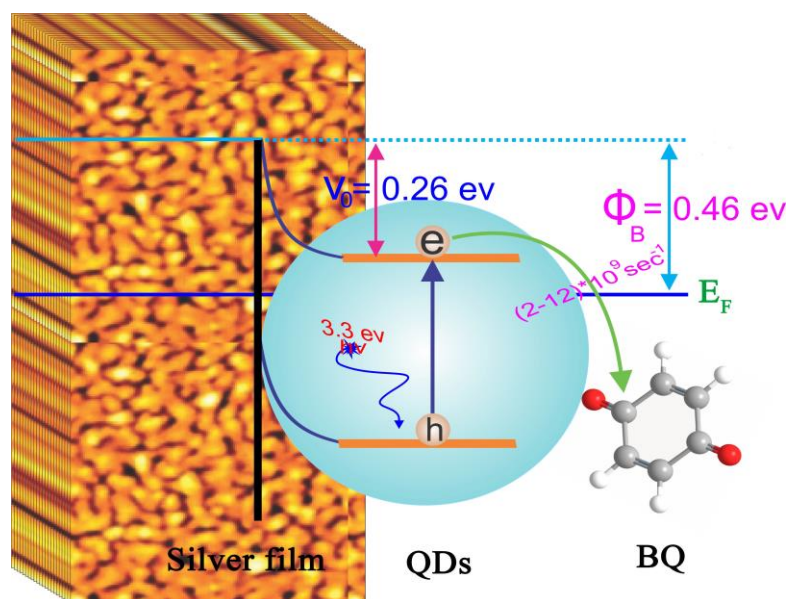


Figure 8.4. Schottky barrier formed at the QDs-silver contact. Φ_B represents the Schottky barrier height and V_0 represents the equilibrium contact potential and was calculated by consulting standard literature [23-25].

The efficiency of FRET for the various QDs on the metal film is depicted in Figure 8.2 and Table 8.1 and found to be in excellent agreement with the estimated values. Both degree of overlap and distance between donor and acceptor have been accounted for simultaneously for FRET efficiency estimation. The FRET efficiency goes on decreasing from LPB to BY with increase in donor-acceptor distance. The effective donor-acceptor distances, which are the distances [26] from the centre of the QDs to the contact point of the QDs to the film, are consistent

with the estimated distances from the diameter of the QDs and the length of the capping ligand TOPO (0.8–1 nm) [27]. The details of the FRET calculations are given in chapter 2. Considering the fact that a point dipole (QDs here) can interact with an infinite metal surface, which is very relevant to our experiment, the energy transfer mechanism can be extended over the well-known FRET model as described above. The extended model was first introduced by Perssons and Lang [28] and is popularly known as NSET where the energy transfer efficiency depends on the inverse of the fourth power of donor–acceptor separation. The details of NSET is discussed in chapter 2. For the NSET, the frequencies of donor electronic transitions for the three quantum dots are taken to be $3.80 \times 10^{15} \text{ s}^{-1}$, $3.50 \times 10^{15} \text{ s}^{-1}$ and $3.26 \times 10^{15} \text{ s}^{-1}$ for LPB, AG and BY respectively. The donor–acceptor distances for LPB, AG and BY assuming the NSET process, are estimated to be 4.04 nm, 5.05 nm and 7.0 nm respectively. The calculated donor–acceptor distance assuming that NSET is guiding the quenching process, was found to be invalid in the present context.

Table 8.1. Individual (τ_i) and average (τ_{av}) fluorescence lifetimes of QDs in different conditions along with Förster distances (R_0), overlap integral ($J(\lambda)$), observed (FRET_{EXP}) and calculated (FRET_{CAL}) FRET efficiencies.

Sample	τ_1 (ns)	τ_2 (ns)	τ_3 (ns)	τ_{av} (ns)	R_0 (nm)	$J(\lambda) \times 10^{14}$ (M ⁻¹ cm ⁻¹ nm ⁴)	FRET _{EXP}	FRET _{CAL}
QDs(LPB;3.2nm)	0.15(26%)	4.08(11%)	18.2(63%)	12.0				
QDs-silver	0.15(64%)	1.72(24%)	8.60(12%)	1.54	3.6	3.67	87%	89%
QDs-BQ	0.07(79%)	0.70(15%)	4.15(06%)	0.41				
QDs(AG;4.4nm)	0.29(27%)	2.89(27%)	9.74(46%)	5.29				
QDs-silver	0.18(59%)	2.20(26%)	8.10(15%)	1.90	3.56	3.41	64%	64%
QDs-BQ	0.03(94%)	0.88(06%)		0.08				
QDs(BY;5.2nm)	0.17(29%)	3.74(19%)	15.2(52%)	8.63				
QDs-silver	0.13(36%)	0.87(22%)	11.0(42%)	4.80	3.5	3.06	35%	36%
QDs-BQ	0.06(86%)	0.57(12%)	4.34(02%)	0.23				

8.3. Conclusion: In summary, our study essentially demonstrates the excited state exciton dynamics of QDs of various sizes in contact with plasmonically active of silver film. The nano-structure on the film surface is found to be responsible for the localized surface plasmon resonance (LSPR) of the metal film. Here we have accounted for every single aspect of the possible mechanisms of the quenching phenomenon (namely charge transfer, nanosurface energy transfer and Förster energy transfer). Among these various possibilities, it is clearly shown that only the nonradiative energy transfer process in the excited QDs takes part in the lifetime quenching and a simple FRET model is good enough to rationalize the quenching phenomenon. Though charge migration from the QDs to silver film is expected, it is not realized in our case due to the formation of a Schottky barrier.

References

1. P. Lodahl, A.F.v. Driel, I.S. Nikolaev, A. Irman, K. Overgaag, D.I. Vanmaekelbergh and W.L. Vos, Controlling the dynamics of spontaneous emission from quantum dots by photonic crystals. *Nature*, **430** (2004) 654.
2. L.A. Blanco and F.J.G. de Abajo, Control of spontaneous emission by complex nanostructures. *Opt. Lett.*, **29** (2004) 1494.
3. T.N. Smirnova, O.V. Sakhno, P.V. Yezhov, L.M. Kokhtych, L.M. Goldenberg and J. Stumpe, Amplified spontaneous emission in polymer-CdSe/ZnS-nanocrystal DFB structures produced by the holographic method. *Nanotechnology*, **20** (2009) 245707.
4. Y. Akahane, T. Asano, B.S. Song and S. Noda, High-Q photonic nanocavity in a two-dimensional photonic crystal. *Nature*, **425** (2003) 944.
5. M.D. Leistikow, J. Johansen, A.J. Kettelarij, P. Lodahl and W.L. Vos, Size-dependent oscillator strength and quantum efficiency of CdSe quantum dots controlled via the local density of states. *Phys. Rev. B*, **79** (2009) 045301.
6. Y. Cesa, C. Blum, J.M. van den Broek, A.P. Mosk, W.L. Vos and V. Subramaniam, Manipulation of the local density of photonic states to elucidate fluorescent protein emission rates. *Phys. Chem. Chem. Phys.*, **11** (2009) 2525.
7. P. Andrew and W.L. Barnes, Energy transfer across a metal film mediated by surface plasmon polaritons. *Science*, **306** (2004) 1002.
8. E. Snoeks, A. Lagendijk and A. Polman, Measuring and modifying the spontaneous emission rate of erbium near an interface. *Phys. Rev. Lett.*, **74** (1995) 2459.
9. Y. Zhenling, W. Yanan, M. Qingkun, L. Yuqiang, S. Yunfei, H. Xing, L. Aihua, Y. Guoyang, Y. Yanqiang and W. Wenzhi, Impact of noble metal nanostructures on surface trapping state of semiconductor quantum dots. *Appl. Phys. Lett.*, **96** (2010) 043118.

10. N. Cade, T. Ritman-Meer and D. Richards, Strong coupling of localized plasmons and molecular excitons in nanostructured silver films. *Phys. Rev. B*, **79** (2009) 241404.
11. D.E. Chang, A.S. Sorensen, E.A. Demler and M.D. Lukin, A single-photon transistor using nanoscale surface plasmons. *Nat. Phys.*, **3** (2007) 807.
12. C.S. Yun, A. Javier, T. Jennings, M. Fisher, S. Hira, S. Peterson, B. Hopkins, N.O. Reich and G.F. Strouse, Nanometal surface energy transfer in optical rulers, breaking the FRET barrier. *J. Am. Chem. Soc.*, **127** (2005) 3115.
13. S. Batabyal, A. Makhal, K. Das, A.K. Raychaudhuri and S.K. Pal, Ultrafast dynamics of excitons in semiconductor quantum dots on a plasmonically active nano-structured silver film. *Nanotechnology*, **22** (2011) 195704.
14. E. Fu, S.A. Ramsey, J. Chen, T.M. Chinowsky, B. Wiley, Y. Xia and P. Yager, Resonance wavelength-dependent signal of absorptive particles in surface plasmon resonance-based detection. *Sens. Actuators B*, **123** (2007) 606.
15. P.K. Jain, X. Huang, I.H. El-Sayed and A.M. El-Sayed, Noble metals on the nanoscale: Optical and photothermal properties and some applications in imaging, sensing, biology, and medicine. *Acc. Chem. Res.*, **41** (2008) 1578.
16. O.A. Yeshchenko, I.M. Dmitruk, A.A. Alexeenko, M.Y. Losytskyy, A.V. Kotko and A.O. Pinchuk, Size-dependent surface-plasmon-enhanced photoluminescence from silver nanoparticles embedded in silica. *Phys. Rev. B*, **79** (2009) 235438.
17. A. Makhal, H. Yan, P. Lemmens and S.K. Pal, Light harvesting semiconductor core-shell nanocrystals: Ultrafast charge transport dynamics of CdSe-ZnS quantum dots. *J. Phys. Chem. C*, **114** (2009) 627.
18. C. Burda, S. Link, M. Mohamed and M. El-Sayed, The relaxation pathways of CdSe nanoparticles monitored with femtosecond time-resolution from the visible to the IR: Assignment of the transient features by carrier quenching. *J. Phys. Chem. B*, **105** (2001) 12286.

19. K. Pechstedt, T. Whittle, J. Baumberg and T. Melvin, Photoluminescence of colloidal CdSe/ZnS quantum dots: The critical effect of water molecules. *J. Phys. Chem. C*, **114** (2010) 12069.
20. B.A. Korgel, Interfaces behaving well. *Nat. Mater.*, **6** (2007) 551.
21. S. Jin and T. Lian, Electron transfer dynamics from single CdSe/ZnS quantum dots to TiO₂ nanoparticles. *Nano Lett.*, **9** (2009) 2448.
22. A. Kongkanand, K. Tvrđy, K. Takechi, M. Kuno and P.V. Kamat, Quantum dot solar cells. Tuning photoresponse through size and shape control of CdSe–TiO₂ architecture. *J. Am. Chem. Soc.*, **130** (2008) 4007.
23. K. Palaniappan, J.W. Murphy, N. Khanam, J. Horvath, H. Alshareef, M.Q. Lopez, M.C. Biewer, S.Y. Park, M.J. Kim, B.E. Gnade and M.C. Stefan, Poly(3-hexylthiophene)-CdSe quantum dot bulk heterojunction solar cells: Influence of the functional end-group of the polymer. *Macromolecules*, **42** (2009) 3845.
24. I.E. Anderson, A.J. Breeze, J.D. Olson, L. Yang, Y. Sahoo and S.A. Carter, All-inorganic spin-cast nanoparticle solar cells with nonselective electrodes. *Appl. Phys. Lett.*, **94** (2009) 063101.
25. K. Tvrđy and P.V. Kamat, Substrate driven photochemistry of CdSe quantum dot films: Charge injection and irreversible transformations on oxide surfaces. *J. Phys. Chem. A*, **113** (2009) 3765.
26. S.S. Narayanan, S.S. Sekhar Sinha, P.K. Verma and S.K. Pal, Ultrafast energy transfer from 3-mercaptopropionic acid-capped CdSe/ZnS QDs to dye-labelled DNA. *Chem. Phys. Lett.*, **463** (2008) 160.
27. D. Steiner, D. Azulay, A. Aharoni, A. Salant, U. Banin and O. Millo, Electronic structure and self-assembly of cross-linked semiconductor nanocrystal arrays. *Nanotechnology* **19** (2008) 065201.
28. B.N.J. Persson and N.D. Lang, Electron-hole-pair quenching of excited states near a metal. *Phys. Rev. B*, **26** (1982) 5409.

List of Publications

(Peer-reviewed journals)

1. S. Batabyal, T. Mondol and S.K. Pal, Picosecond-resolved solvent reorganization and energy transfer in biological and model cavities. *Biochimie*, **95** (2013) 1127.
2. S. Batabyal, T. Mondol, S. Choudhury, A. Mazumder and S.K. Pal, Ultrafast interfacial solvation dynamics in specific protein DNA recognition. *Biochimie*, **95** (2013) 2168.
3. S. Batabyal, S. Rakshit, S. Kar and S.K. Pal, An improved microfluidics approach for monitoring real-time interaction profiles of ultrafast molecular recognition. *Rev. Sci. Instrum.*, **83** (2012) 043113.
4. S. Batabyal, T. Mondol, K. Das and S.K. Pal, Förster resonance energy transfer in a nanoscopic system on a dielectric interface. *Nanotechnology*, **23** (2012) 495402.
5. S. Batabyal, A. Makhal, K. Das, A.K. Raychaudhuri and S.K. Pal, Ultrafast dynamics of excitons in semiconductor quantum dots on a plasmonically active nano-structured silver film. *Nanotechnology*, **22** (2011) 195704.
6. S. Batabyal, S. Choudhury, D. Sao, T. Mondol and S.K. Pal, Dynamical perspective of protein DNA interaction. *Biomol Concepts.*, In press (2014).
- *7. T. Mondol, S. Batabyal and S.K. Pal, Interaction of an antituberculosis drug with nano-sized cationic micelle: Förster resonance energy transfer from dansyl to rifampicin in the microenvironment. *Photochem. Photobiol.*, **88** (2012) 328.
- *8. T. Mondol, S. Batabyal, A. Mazumder, S. Roy and S.K. Pal, Recognition of different DNA sequences by a DNA-binding protein alters protein dynamics differentially. *FEBS Lett.*, **586** (2012) 258.

- *9. T. Mondol, S. Batabyal and S.K. Pal, Ultrafast electron transfer in the recognition of different DNA sequences by a DNA-binding protein with different dynamical conformations. *J. Biomol. Struct. Dyn.*, **30** (2012) 362.
- *10. S. Choudhury, S. Batabyal, D. Sao, T. Mondol and S.K. Pal, Ultrafast dynamics of solvation and charge transfer in a DNA-based biomaterial. *Chem. Asian J.*, DOI: 10.1002/asia.201400062 (2014).
- *11. T. Mondol, S. Banerjee, S. Batabyal and S.K. Pal, Study of biomolecular recognition using time-resolved optical spectroscopy. *Int. Review of Biophysical Chemistry*, **2** (2011) 211.

* Not included in the thesis.